Development of a Monte Carlo Simulation for SPECT Myocardial Perfusion Imaging

A thesis submitted in partial fulfilment of

the requirements for the

Degree of Master of Science in

Medical Physics

By

Miriam Dixon

University of Canterbury

2021

Abstract

The aim of this study was to develop a Monte Carlo simulation that can be used to model a single photon emission computed tomography (SPECT) scan – in particular, a myocardial perfusion imaging (MPI) scan. The developed simulation models a clinically implemented MPI SPECT protocol and was validated to ensure it produces imagery comparable with the clinical SPECT system. The simulation, in conjunction with a digital anthropomorphic phantom, was used to investigate the changes in image quality with patient size in an MPI scan. Proof of concept simulations were completed to show the decreasing image quality with increasing patient habitus and the associated change in visibility of a lesion within the reconstructed image.

The Monte Carlo program GATE v9.0 was used to model a Symbia T2 gamma camera. Model accuracy was validated by comparing the simulation's spatial resolution, energy resolution and extrinsic uniformity to the physical system and was found to be a sufficiently accurate representation of the physical Symbia system. The 4-dimensional extended cardiac-torso (XCAT) phantom was used to represent the average adult male (176 cm, 75.6 kg), with other phantoms generated by scaling the average phantom. Implementation of time reduction techniques within the simulation, such as the inclusion of phase space files as sources, were deemed essential.

The simulation and phantom were used to investigate the relationship between image quality and patient size in an MPI scan. Two sets of simulations were completed, one with and one without a lesion present in the myocardium. The images were reconstructed using clinical software and compared in terms of signal, SNR and CNR. Results from the simulation show the expected decrease in image quality as patient habitus increases, following a $1/r^3$ relationship where r represents patient chest radius. The images were also viewed and rated by MPI experts, which confirmed that the visual clinical assessment followed the same trends as the measured results.

The model developed is an accurate representation of the Symbia T2 detector. A proof of concept study shows that data collected from the simulation can be used in studies such as the optimisation of administered activities.

Acknowledgments

First of all, I would like to deeply thank both my supervisors, Steve Marsh and Darin O'Keeffe, for all their help throughout this project. From our initial conversations around choosing a topic, and through all the ups and downs of making it work, your support and guidance has been invaluable in making this thesis become a reality.

Thanks also to Professor Paul Segars of Duke University, for allowing use of the XCAT phantom and answering the questions I had about it. Your kindness will not be forgotten.

I would also like to acknowledge the NZPEM 2021 Committee, for allowing me to attend and present at their conference under a student scholarship. The experience was a highlight of my thesis year.

This thesis would not have been possible without the additional support provided to me by both my parents, Wayne and Bronwyn Tucker, and my parents-in-law, Ron and Janet Dixon. Between proof reading multiple drafts, listening to updates on what hasn't worked quite right recently, and your constant prayers and moral support, I have truly appreciated how invested you have each been in my progress.

Michael, my amazing husband, thank you so much. I could fill this whole page with things I have noticed you doing to help make this easier on me, especially these last few months of pulling it all together. You are the best cheerleader I could have asked for.

Finally, and above all these, I would like to acknowledge my Father God, for being with me every step of the way and giving me the intelligence to be able to complete this task. To God be the glory.

Table of Contents

Table of Figures

Table of Tables

Abbreviations

^{99m}Tc	The radioactive isomer of ^{99}Tc
AAPM	American Association of Physicists in Medicine
CI	Confidence Interval
CNR	Contrast-to-Noise Ratio
CT	Computed Tomography
FBP	Filtered Back Projection
Flash3D-AC	Flash3D Reconstruction with Attenuation Correction
Flash3D-NoAC	Flash3D Reconstruction without Attenuation Correction
FWHM	Full Width Half Maximum
GATE	Geant4 Application for Tomographic Emission
Geant4	Geometry And Tracking
LEHR	Low Energy High Resolution
LHC	Large Hadron Collider
MCAT	Mathematical Cardiac-Torso
MPI	Myocardial Perfusion Imaging
MRI	Magnetic Resonance Imaging
NCAT	NURBS-based Cardiac-Torso
NURBS	Non-Uniform Rotational B-Spline
OSEM	Ordered Subsets Expectation Maximisation
PDF	Probability Distribution Function
PMT	Photomultiplier Tube
PSF	Point Spread Function
QA	Quality Assurance
ROI	Region of Interest
ROR	Radius of Rotation
SIMIND	Simulating Medical Imaging Nuclear Detectors
SNR	Signal-to-Noise Ratio
SPECT	Single Photon Emission Computed Tomography
STL	Stereolithographic
TOPAS	Tool for Particle Simulation
XCAT	Extended Cardiac-Torso

1 Introduction

Nuclear medicine is a branch of medicine that relates to the administration of radioactive elements (radionuclides) for diagnostic or therapeutic purposes [1]. The radionuclides are chosen based on the nuclear medicine technique being used, with gamma or positron emitters favoured by imaging modalities and alpha or beta emitters favoured by therapeutic modalities [2]. The radionuclide is attached to a pharmaceutical, making a radiopharmaceutical. The pharmaceutical is chosen according to the organ or tissue that is being imaged, as it guides the radionuclide to the organ or tissue in question. This allows the radionuclide to accumulate in a particular location rather than being evenly distributed throughout the body [3].

One of the main modalities within nuclear medicine is Single Photon Emission Computed Tomography (SPECT). SPECT scans utilise gamma emitting radionuclides to observe the functionality of an organ [1]. This is different from the more common Computed Tomography (CT) or magnetic resonance imaging (MRI) scans which produce an anatomical map of the patient. Myocardial perfusion imaging (MPI) scans are a common type of SPECT scan, centred around the heart [4]. The radiopharmaceutical is taken up by the heart muscle to observe the flow of blood within the myocardium. Areas of significantly reduced uptake on the scan indicate a probable defect within the heart muscle.

An MPI scan can be used to diagnose coronary artery disease (CAD), or to assess muscle damage after a heart attack. This procedure is relevant in New Zealand as CAD is one of the leading causes of death [5]. CAD occurs when there is a build-up of plaque within the arteries that supply blood to the heart muscle. This limits the level of oxygen reaching the heart muscle and can lead to myocardial infarction (a heart attack). A correct diagnosis relies on the MPI scan producing an image of diagnostic quality, and is dependent on the amount of administered radiopharmaceutical being correct.

The amount of activity administered to a patient for an MPI scan is carefully monitored in accordance with the guidelines for diagnostic procedures laid out in the Code of Practice for Nuclear Medicine in New Zealand [6]. If the amount of administered activity is too low, the image produced will not be of sufficient quality to indicate the presence of a defect. It is also possible that the low level of activity could result in a defect being observed that is not truly present. This result would put the patient through undue stress, until further tests could confirm the health of the myocardium. If the administered activity is too high, then the patient is exposed to higher levels of radiation than is necessary. Both of these scenarios have potential to cause more harm to the patient than any benefit they may get from the procedure [7]. For “average” weight adult patients (around 70 kg) there is good

agreement on the required activity to be able to discern any defect within the myocardium [8]. For patients of the same height, an increase in weight increases the volume of tissue the emitted photons must pass through to reach the detector [9]. This increase in tissue volume increases the potential for the photons to be scattered or attenuated, reducing the signal reaching the detector. A lower signal reduces the image quality of the output through a decrease in signal to noise ratio, meaning patients of larger body habitus require a higher level of activity to be administered, to achieve an image of the same diagnostic quality achieved for patients of average body habitus.

Despite being the subject of several studies [7]–[13], the optimal scaling of activity administered to a patient as patient weight increases is still an open question. Many studies into optimisation are based on clinical data [7]–[9], [11], [12]. These studies have the disadvantage of not knowing, at the time of the study, whether the patient has a lesion or not. This restricts how much the amount of administered activity can be lowered by – if the presence of a defect is not known, the activity level at which it can be stated with confidence that the image shows no defect is uncertain. Using patient data for the optimisation study also restricts the amount the radiation can be increased by, due to an increased risk of stochastic effects (such as cancer) at higher administered activity levels [14]. These restrictions naturally do not apply when the optimisation study is performed on simulated patients (phantoms) within computer simulations.

Monte Carlo techniques use random number generation and probability distributions to simulate a given scenario. While they can be used in a wide range of situations, Monte Carlo is well known for its ability to simulate the transportation of particles through different media. How charged and uncharged particles travel through tissue, and how energy is transferred from the moving particles to the tissue they are passing through, is of particular interest to radiotherapy and diagnostic radiology [15]–[17]. These simulations allow a way of conducting studies in different modalities of therapy and diagnostics without having a potentially negative impact on the study subjects. With proper use, there is the ability to conduct a series of experiments which vary only one parameter, such as in an optimisation study. Each Monte Carlo system has strengths and weaknesses, based on what the intended purpose of the system is. Some are general purpose software that have the power to compute many different scenarios. However, due to their flexibility, they can take a very long time to finish their computations. Others are very specific in what they are designed to do, which help them to run faster but make them harder to adapt. Once the Monte Carlo software best suited to a situation has been found, it is a powerful tool for exploring the relationships between variables that, in a real-world situation, could not be observed independently.

1.1 Study Aim

The aim of this thesis was to develop a Monte Carlo simulation that accurately models the important components of a SPECT camera system at Christchurch Hospital. It was intended that the simulation developed would be used in future research to find the optimal level of administered activity for an MPI scan based on patient habitus using Monte Carlo modelling techniques. The end goal of the future study will be to provide data to clinical staff at Christchurch Hospital from which scaling of administered activity can be based, as patient weight increases relative to patient height.

The first part of this project was to model a SPECT system within a Monte Carlo simulation. This SPECT system was modelled after the system used at Christchurch Hospital for MPI scans. This model was then validated against the hospital system, to ensure it produces data comparable with the original system.

The second part of this project was to properly characterise a digital human phantom that can be used within the developed simulation. The steps taken were aimed at preparing the phantom for use in an MPI scan, but the same process could be applied to prepare the phantom for use in any SPECT study.

The third part of this project was a proof of concept study, relating the simulation back to how it could be used to answer clinical questions. The aim of this part was to use the developed simulation, in conjunction with a phantom representing patient geometry, to investigate the change in image quality with patient size. Simulations were completed to show the decrease in image quality with an increase in patient size and the associated change in visibility of a heart defect within the reconstructed image.

1.2 Limitations

A key limitation with this study was computing time. While resources are available to decrease the amount of time each simulation took, there is a limit to that reduction. Simplifying the system and reducing the number of particles being followed would decrease the time needed for each simulation but this would also increase uncertainty associated with results thereby decreasing confidence in any useful information gathered. The time limit for this study requires a balance to be found between speeding up simulations while not oversimplifying the methodology.

To narrow the focus of the study, improving the image quality through improved reconstruction methods was not considered. Only those reconstruction methods currently used by the hospital were

used in the study. Electron production in the phantom during the simulation was also not considered, as the focus of the study was to optimise the image quality, which is reliant on gamma photons only.

1.3 Ethical Considerations

This study used patient data retrospectively to validate the simulation. An application for ethics approval was made through the Canterbury District Health Board, with a result stating that ethics approval was not required. This was due to the project having no interaction with patients as all patient related data had been previously obtained through usual hospital practice, and anonymised.

1.4 Thesis Structure

To provide the reader with the fundamental background needed to understand this study, Chapter Two will cover the background of nuclear medicine imaging, specifically for MPI SPECT, and how Monte Carlo techniques can be utilised for studies in this area. It will also outline how this study fits within the current literature. The methods for each stage of the project are presented in Chapter Three. Chapter Four lays out the results from each stage, with these results discussed further in Chapter Five, including possibilities for future work. Final conclusions are presented in Chapter Six.

2 Background

This chapter introduces the concepts needed to fully appreciate the aims of this study. An overview of what Nuclear Medicine is and how it forms images of organ function within the body, including a selection of different reconstruction methods, is introduced first. The way photon interactions with matter affect this imaging process, particularly within SPECT scans, are described. Quality Assurance (QA) is an important part of ensuring diagnostic confidence for a SPECT system, so the QA steps that take place when working with SPECT are outlined. These steps will be imitated by the Monte Carlo simulation in the validation steps in Chapter 3. Myocardial perfusion imaging (MPI), the imaging scan in use in this study, is then specifically introduced. An overview is given of previous optimisation studies within MPI, including the advantages and disadvantages of doing an optimisation study through computer simulations. To better understand how computer simulation studies are designed, an introduction to Monte Carlo techniques is provided, followed by a brief history of computer generated anatomical phantoms. Specific simulation software types are then discussed, including GATE, TOPAS and SIMIND. Finally, different techniques for measuring image quality are introduced and compared.

2.1 Nuclear Medicine

Nuclear medicine involves using radioactive substances as tools for diagnostics or therapy. A radionuclide is attached to a pharmaceutical to create a radiopharmaceutical [18] and is administered to the patient either by inhalation, swallowing or injection [3]. The pharmaceutical is responsible for guiding the radionuclide to the correct location within the body [19]. Different tissues have a different level of affinity to different pharmaceuticals, meaning the pharmaceuticals are more likely to accumulate in those organs or around those tissue types with highest affinity to the pharmaceutical administered. The radionuclides are chosen based on the nuclear medicine technique being used, with gamma or positron emitters favoured by imaging modalities and alpha or beta emitters favoured by therapeutic modalities [2].

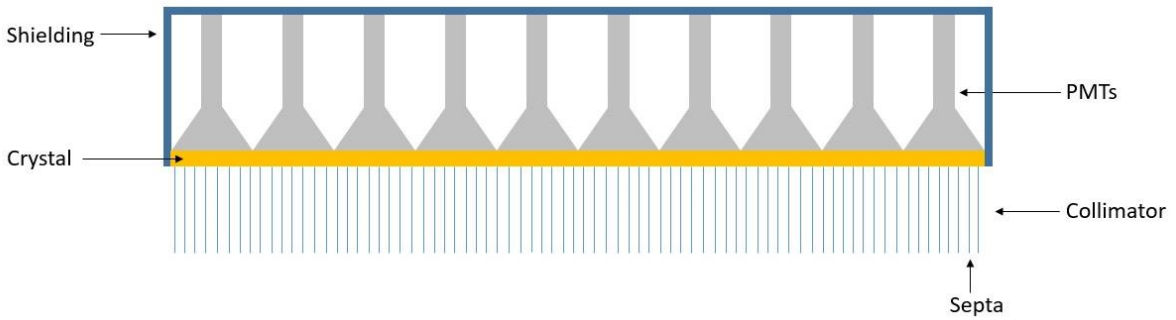

Figure 1: Diagram of a gamma camera, indicating the collimator, septa, scintillating crystal, photomultiplier tubes (PMTs) and shielding.

A gamma camera is a device specially designed to detect photons to form an image of the distribution of a radiopharmaceutical [20]. The basic design of a gamma camera (Figure 1) is a crystal made of a scintillating material, on a grid of photomultiplier tubes (PMTs), with shielding around the back and sides. On the front of the crystal is a collimator. The holes of the collimator are separated by thin lead walls called septa. The diameter and depth of the holes in the collimator affect the sensitivity and resolution of the detector.

Assuming no scatter, the photons emitted by the radiopharmaceutical travel in a straight line from their point of emission, but can be emitted in any direction (Figure 2). This results in photons reaching the gamma camera from a range of angles, distorting the final image as the detector cannot tell what

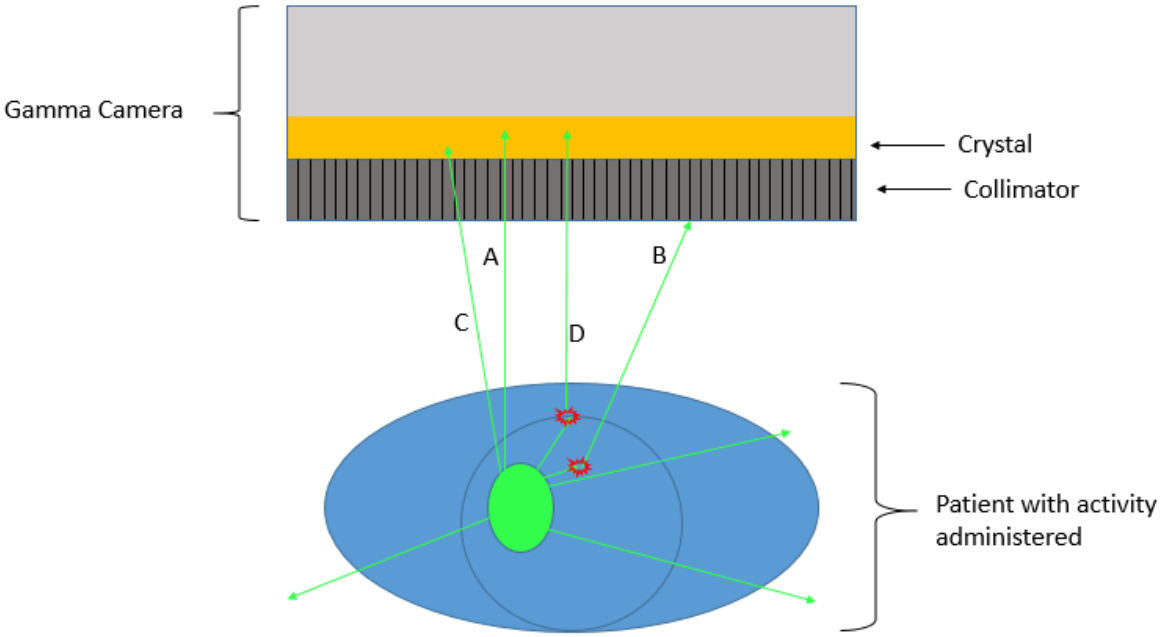

Figure 2: Four different scenarios for photons (green arrows) leaving the site of activity accumulation (green oval). ***A)*** *Photon passes straight through the collimator without passing through a septa or interacting in the body (ideal scenario).* ***B)*** *Photon has interaction within the body and is scattered in a way that it cannot pass through the collimator due to septa interaction.* ***C)*** *Photon leaves the body at a slight angle and passes through one septa and reaches the crystal.* ***D)*** *Photon has interaction within the body and is scattered in a way that it can pass through the collimator without interaction.*

direction the photon originated from. Gamma photons also cannot be focused, the way optical photons can, meaning another method must be used to collect the photons into a clear image. The introduction of a lead collimator on the front of the camera means only those photons travelling approximately perpendicular to the camera surface are detected (Figure 2, Case A). Photons that have been scattered to, or are originally travelling at, directions other than perpendicular to the camera surface are absorbed by the lead septa (Figure 2, Case B) [21]. Some photons pass through the collimator at a slight angle (Figure 2, Case C), or have been scattered within the body before reaching the collimator and therefore are travelling in a different direction than they were originally (Figure 2, Case D). The interaction events that can occur between photons and the material they are passing though are Compton scattering, Rayleigh scattering or Photoelectric interactions.

When the photons interact with the detector crystal constructed of a scintillation material, the crystal scintillates, releasing lower energy photons [20]. These photons are collected by PMTs which boost the signal. The signal then passes through circuitry which only registers the signal with energy corresponding to the selected range around the peak energy of the radiopharmaceutical in use. Only this registered signal is recorded in the image[22]. Photons that are scattered within the body before interacting with the detector crystal may lose sufficient energy to no longer be within the accepted energy range. These photons are not recorded.

After the gamma camera has been in one position relative to the patient long enough to collect sufficient photons to form an image, the camera is rotated about the patient by a few degrees, and photons are captured from this new angle. Each angle of the detector, relative to the patient, relates to one projection image. The time required for a projection image to form depends on the scan protocol but is generally in the range of 15 – 30 seconds [23]. This is repeated over 180° or 360° degrees, producing a series of projection images [24]. The projections are then processed by a computer and used to create a three-dimensional reconstruction of the distribution of the radiopharmaceutical [25], which can be viewed as two-dimensional slices passing through the reconstructed volume in any direction [26]. The process of collecting a series of images by rotating a detector around an object is called tomography.

SPECT is a tomographic imaging technique in nuclear medicine that forms an image from captured photons emitted by gamma emitting radionuclides. The images produced by a SPECT scan show the distribution of the radiopharmaceutical within the body. This distribution information is used to determine how the organ in question is functioning.

2.2 Image Reconstruction Methods

A SPECT scan produces a set of projection images which must be processed to produce an image of the inside of the scanned object. This processing is known as reconstructing the images and can be done following a variety of methods. The two main streams of reconstruction methods for SPECT images are filtered back projection (FBP) and iterative reconstruction.

Before either method can be used, first the projection images must be turned into a set of sinograms (Figure 3). A sinogram is formed by taking the equivalent row of pixels from each projection angle and stacking them into a single image [22]. For any object not fully symmetrical or centred in the field of view, the changing position of peak intensities creates a sinusoidal pattern, giving sinograms their name. A sinogram is formed for every row of pixels in the projection image, and each sinogram relates to one slice through the imaged object. The job of the reconstruction software is to convert this sinogram into an image slice.

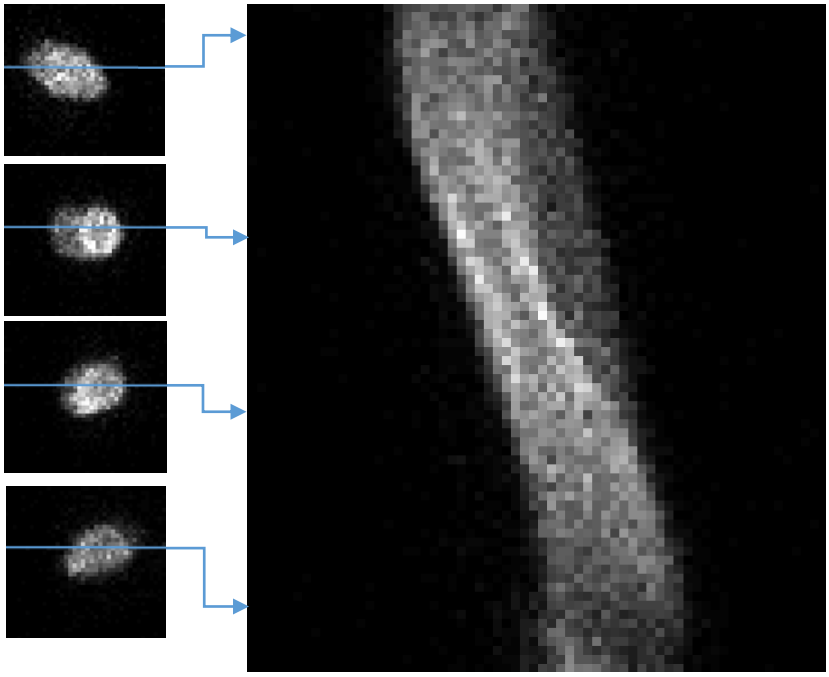

Figure 3: Different projection images (left) each contributing an equivalent row of pixels to form a sinogram (right).

2.2.1 FBP

FBP does the conversion from sinogram to image slice by taking each row of pixels from the sinogram and applying the intensities of that row at the angle the row corresponds to [24]. The more angles in the sinogram, the more refined the final image is (Figure 4).

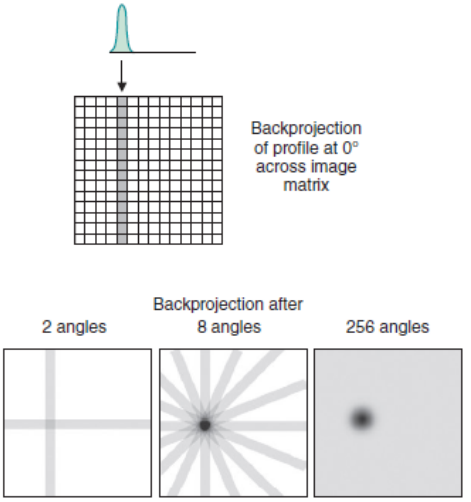

Figure 4: Example of the process of back projection of a point source. Image reproduced from [22].

When this method is applied without a filter the final image has 1/r blurring, due to the nature of the back projection process [22]. This reduces the contrast of the image, so applying a filter helps keep the desired spatial frequencies while cutting out the unwanted spatial frequencies. There are several different kinds of filter that can be applied, depending on which frequencies you want to remove [27]. A Ramp filter (Figure 5), described by Eq. 1 [28], removes the low frequency components of an image, reducing the effect of the 1/r blurring. They are high pass filters, meaning they allow the high frequency components of the image to remain. In nuclear medicine, noise is a large part of the high frequency component of images. For this reason, the Ramp filter on its own is not a good fit for nuclear medicine images [24].

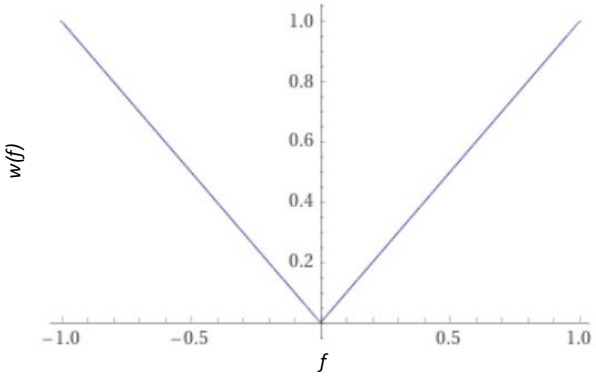

Figure 5: The shape of the Ramp filter in frequency space.

$$w(f) = |f|$$

Eq. 1

Where

Symbol	*Meaning*	*Units*
w(f)	*Filter amplitude*	
f	*Spatial frequencies of the image*	*1/cm*

Another filter is the Butterworth filter, which is a low pass filter [1]. This means it allows low frequency components of the image to remain but filters out the high frequency components. The shape of the Butterworth filter is described by Eq. 2.

$$w(f) = \frac{1}{\sqrt{1 + \left(\frac{f}{f_c}\right)^P}}$$

Eq. 2

Where

Symbol	*Meaning*	*Units*
f_c	*Critical frequency*	*1/cm*
P	*Power factor*	

The critical frequency is the frequency at which the filter starts to roll off towards zero (Figure 6), while the power factor controls how quickly the filter falls away towards zero after the critical frequency. A high power factor relates to a steep roll-off, while a low power factor has a flatter roll-off. The critical frequency determines where along the frequency spectrum the filtering begins.

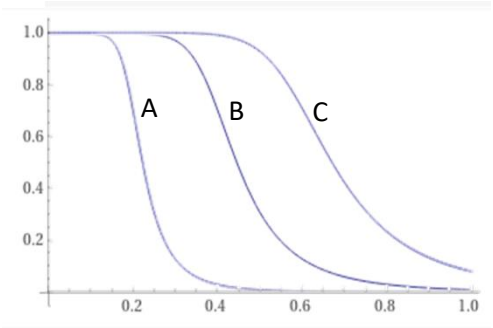

Figure 6: The shape of the Butterworth filter in frequency space, using a power factor of 10 and three different critical frequencies: 0.2 (A), 0.4 (B), and 0.6 (C).

The Hann filter (Figure 7) has a similar shape to the Butterworth filter, also being a low pass filter [1]. The equation (Eq. 3) for the Hann filter is

$$w(f) = 0.5 + 0.5\cos\left(\frac{\pi f}{f_m}\right) \quad if \ \ |f| < f_m$$

Eq. 3

Where

Symbol	***Meaning***	***Units***
f_m	*Cut-off frequency*	*1/cm*

The filter is zero for all frequencies above the cut-off frequency. By increasing the cut-of frequency, more edge detail can be retained within the image. However, the amount of noise retained also increases.

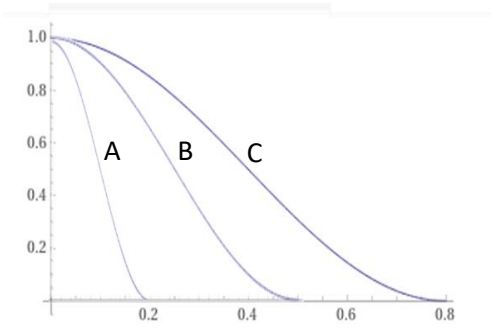

Figure 7: The shape of the Hann filter in frequency space, with three different cut-off frequencies: 0.2 (A), 0.5 (B), and 0.8 (C).

For both the Butterworth and Hann filters, being low pass filters, they do not address the problem of 1/r blurring that occurs during FBP reconstruction. By combining the equation for either the Butterworth or Hann filter with that of the Ramp filter, both the lowest frequencies, relating to the 1/r blur, and the high frequencies, relating to noise, are filtered out [1]. The mid-range frequencies, relating to the bulk of the useful image information, are retained and made clearer.

2.2.2 Iterative Reconstruction

More computationally expensive than FBP, iterative reconstruction methods start with an estimate of the image (Figure 8). This estimate is used to create projection data created using forward projection [24]. These forward projected images are compared with those being reconstructed, and the differences between the two sets are used to update the image estimate [27]. This process is repeated a set number of times or until the difference between the images are below a given threshold [24].

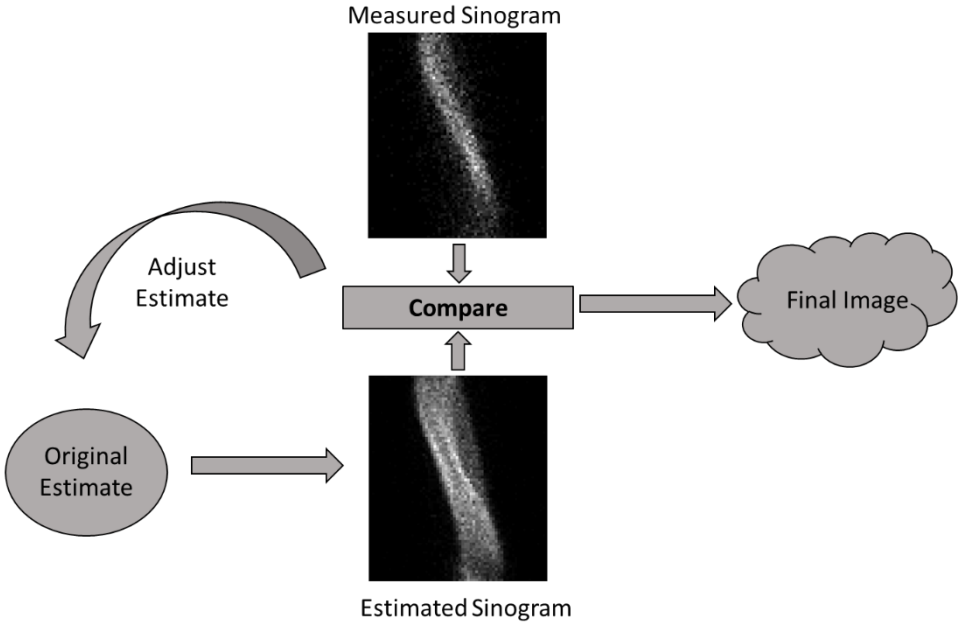

Figure 8: Diagram outlining the process of iterative reconstruction. Starting with an image estimate, a sinogram estimate is formed. This is compared with the measured sinogram. The comparison is used to adjust the original estimate and the cycle is repeated until a final image is produced.

There are many kinds of iterative reconstruction methods, some algebraic and others statistical [1]. A common statistical algorithm used for reconstruction is ordered subsets expectation maximization (OSEM). In this method, the number of projections within a simulation are split evenly into a number of subsets. Each subset then undergoes the iterations of forward projection and comparison, with the reconstruction produced by subset one being the starting estimate for subset two, and so on [1]. Each full rotation of all the subsets is referred to as a single iteration. Several iterations can be done with the starting point for each successive iteration being the final reconstruction from the previous iteration [29].

A further development of the OSEM method is the Flash 3D method released by Siemens. Flash 3D has the added ability to apply both 3D point spread function correction and attenuation correction to its reconstruction images [30]. The correction is based on images produced by a low-dose CT scan that is matched to the field of view of the SPECT scan.

2.3 Photon Interactions with Matter

During nuclear decay, a nucleus is transformed from an excited state to a less-excited, more stable state. The products of nuclear decay are a daughter nucleus and, depending on the decay type, either an alpha particle, a beta particle in the form of a positron or an electron, or a gamma photon. The imaging modalities of nuclear medicine are most interested in the decays producing positrons or gamma photons. Both these decay types result in the emission of a photon – although in a reaction producing positrons, the photons are a secondary product. These photons are able to pass through the patient and be detected by the gamma camera [1]. Radionuclides that emit predominantly alpha or beta particles are not commonly used as they deposit significant energy within the body, with no or very few gamma rays detected by the gamma camera. Some gamma emitters also emit an alpha or beta particle as part of their decay scheme, but ideally the radionuclide chosen is a pure gamma emitter. On the way to the camera, and within the camera itself, there are four types of interactions that can occur between the photon and the matter it is passing through: Compton scattering, Rayleigh scattering, photoelectric interactions, and pair production. It is important to understand these processes as they explain how the photons can be detected to form the image. They also explain the appearance of scattering within the image. As pair production does not occur at the energy levels used for SPECT imaging, it is not discussed here – an interested reader can find more information in [31].

2.3.1 Compton Scattering

Compton scattering occurs when a photon interacts with an electron in the outermost shell of an atom [22]. The photon's path changes by an angle θ and some of its energy is transferred to the electron, which is then freed from the atom (Figure 9) [32]. The angle of scattering, θ, can be anywhere between 0° - 180°. The energy transferred to the electron is proportional to the scattering angle [31]. A

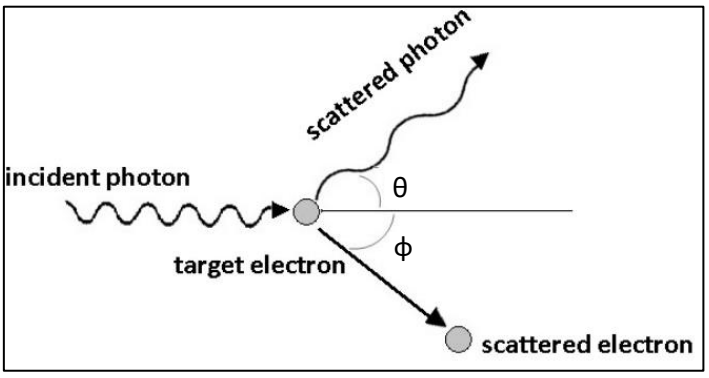

Figure 9: Diagram of a Compton Scattering event, where φ is the angle of the scattered electron and ϑ the angle of the scattered photon, relative to the direction of travel of the incident photon. Reproduced from [32].

scattering angle of 0° transfers very little energy to the electron. A scattering angle of 180° transfers the maximum energy to the electron.

When Compton scattering occurs during a SPECT scan, it results in either a reduction in the number of photons reaching the detector, or an increase in the blurring of the image. A photon that is originally emitted in the direction of the detector can be scattered so its path is no longer perpendicular to the gamma camera. This will result in the photon either being absorbed by the collimator, or missing the camera completely, reducing the number of photons captured by the detector. A photon that is originally emitted at an angle slightly off perpendicular to the gamma camera can be scattered at a small angle, so it is now lined up to pass through the holes in the collimator. As the photon was only scattered at a small angle, it would not have lost much energy and could still be within the accepted energy window. This will result in the misplacement of the photon within the image, increasing blur.

2.3.2 Rayleigh Scattering

Rayleigh scattering occurs when a photon interacts with a whole atom, rather than just an outer electron [22]. The photon is scattered without losing a significant amount of energy to the atom (Figure 10), due to the relatively large mass of the atom [33]. Rayleigh scattering does not, therefore, result in absorption of energy by the scattering material, but does alter the path of the photon which can then appear in the wrong place in the detector. As Rayleigh scattering is most observable at low energies, it has less effect on the quality of the final image as Compton scattering [22].

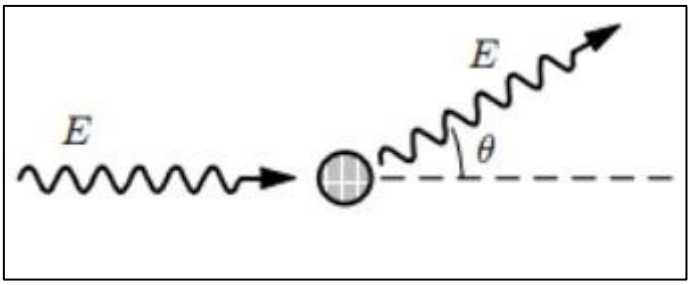

Figure 10: Diagram of a Rayleigh scattering event, where θ is the angle the photon is scattered by, while the energy remains the same. Reproduced from [33].

2.3.3 Photoelectric Effect

The photoelectric effect (Figure 11) occurs when a photon is absorbed by an atom, rather than just being scattered [22]. The energy absorbed from the photon is used to free an electron, known as a photoelectron. Any energy not used in the freeing of the electron is given to the electron as kinetic energy [31]. When the freed electron is from an inner shell, the gap left behind is then filled by an electron from a higher shell dropping down into it. The change of energy level for this electron leads to the production of characteristic x-rays or Auger electrons.

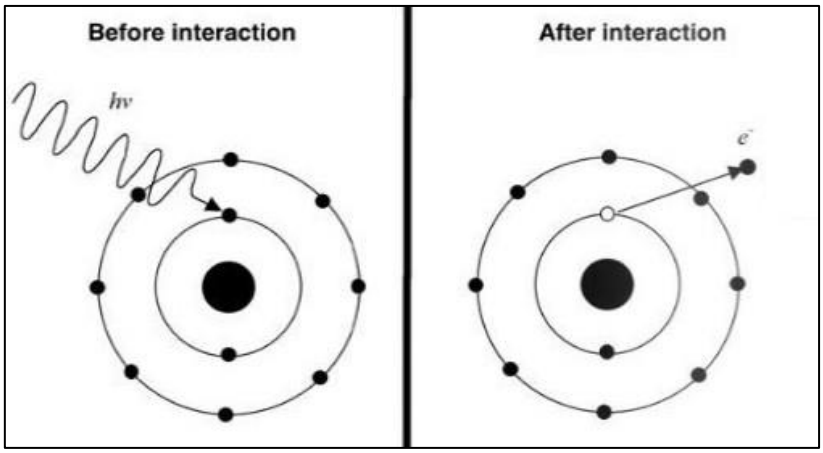

Figure 11: A diagram of the photoelectric effect, showing the absorption of the incident photon, followed by the emission of an inner-shell electron. Reproduced from [31].

When the photoelectric effect occurs within the patient, it does not produce any photons that might be detectable by the gamma camera. This affects the image quality as fewer photons reach the detector. It is also an important factor in the potential dose to the patient, as the energy of the photon is deposited within the body by the freed electron. Once photons reach the detector, it is through the photoelectric effect that the photon is absorbed by the scintillating crystal, forming a signal pulse.

For photons of the same energy, the relative likelihood of whether a photon will undergo Compton scattering or a photoelectric interaction depends on the atomic number (Z) of the material the photon is passing through (Figure 12) [34]. Z is the number of protons within the nucleus of each atom of the material [22]. Materials with high Z, such as the material used in the detector crystal [35], are more likely to have a photoelectric interaction. Low Z materials, such as soft tissue in patients [36], are more likely to cause Compton scattering. This is why photons emitted in the patient can pass through the body but then be detected by a relatively thin crystal.

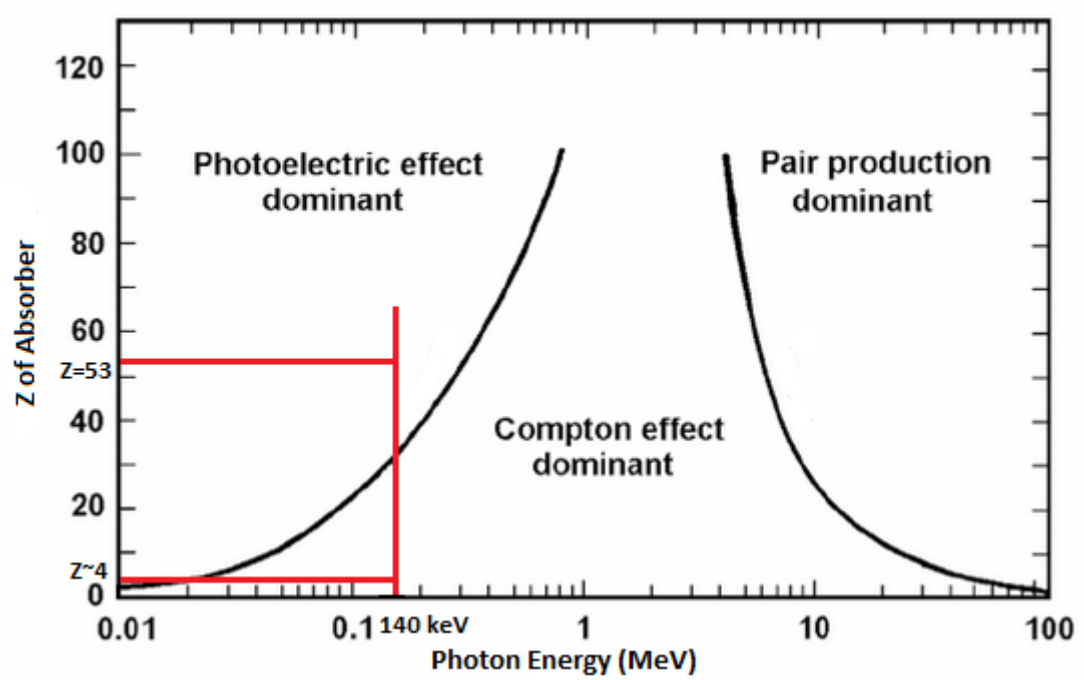

Figure 12: The dominance of different photon absorption methods, as they vary with photon energy and Z of the absorbing material. Red vertical line marking 140 keV, the energy used for many SPECT scans. Red horizontal lines marking the Z of Iodine (Z=53 [31]) in the photoelectric effect dominant region and the effective Z of soft tissue (Z~4 [32]) in the Compton Effect dominant region. Figure adapted from [34].

2.4 Quality Assurance

Quality assurance (QA) refers to those tasks completed on a regular basis that show whether the systems in question are operating within expected parameters [22]. In SPECT, QA tests are carried out on a daily, weekly, monthly, quarterly, and yearly basis. These tests measure things such as (but not limited to) gamma camera uniformity, intrinsic and extrinsic spatial resolution, and energy resolution [37].

For the image acquired using a gamma camera to be uniform, the sensitivity across the face of the camera must be consistent. Uniformity can be measured either intrinsically (without a collimator) or extrinsically (with a collimator). Intrinsic uniformity measurements are performed using a point source, set at a distance of several fields of view from the detector [22]. At such a distance, the variation in distance from the point source to the detector between the centre and edges of the detector results in minimal change in the intensity of the signal. Intrinsic uniformity measurements are a measure of the uniformity of the crystal and PMTs. An extrinsic uniformity measurement is completed using a planar source placed on top of the collimator [22]. Extrinsic uniformity is important to determine the state of the collimator, and the underlying detector. If the collimator has septa that are damaged in some way, the collimator will not allow photons to pass through evenly.

Spatial resolution can also be separated into intrinsic and extrinsic spatial resolution. Intrinsic resolution is affected by the thickness of the detector crystal [38]. Thinner crystals allow for greater spatial resolution as the scintillation photon cone has less room to spread before being captured by the PMT. However, this does lead to a decrease in sensitivity of the detector as a thinner crystal means it is more likely gamma photons will not be absorbed by the crystal, meaning these photons will not contribute towards the image. Extrinsic resolution is affected by the collimator design [22]. Collimator hole diameter, septa thickness, and collimator hole length are all components that affect the extrinsic resolution.

Energy resolution is the ability of a system to differentiate between two photons of different energies [39]. Photons entering the detector have specific energies, dependant on their source and what scattering events they underwent before reaching the detector. This would result in very sharp spectra, with the exact energy of each photon being recognised. However, what is observed is a broader spectrum with its mean relating to the expected photon energy (Figure 13). This broadening of the spectrum is due to statistical fluctuations throughout the process of converting the gamma photon detection into output signal [22]. The broader this peak is, the greater the difference between two photon energies must be for them to be distinguishable in the final spectrum.

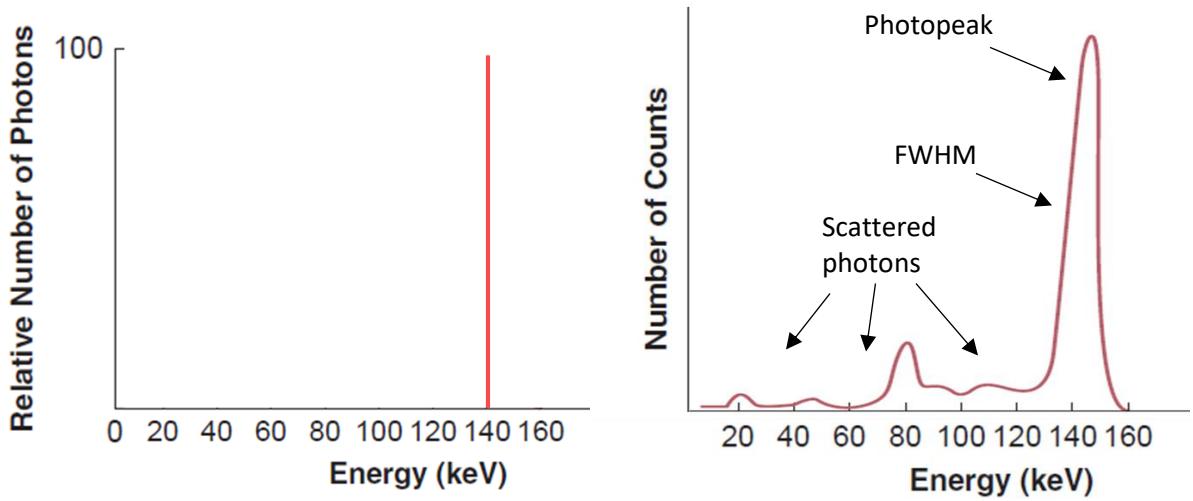

Figure 13: Comparison between the energy of photons emitted by 99m-Tc (left) and the detected energy spectrum (right). The FWHM of the photopeak is determined by the energy resolution of the detection system. Other signal is produced by the various interactions photons undergo before detection. Image adapted from [39].

2.5 Myocardial Perfusion Imaging (MPI)

MPI is a nuclear medicine functional scan of the heart, specifically interested in the blood flow through the myocardium [40]. Two radiopharmaceuticals often used for MPI is technecium-99m (^{99m}Tc) labelled to tetrofosmin [41] and ^{99m}Tc-labelled sestamibi. This study will focus on tetrofosmin because that is the pharmaceutical of choice at Christchurch Hospital. An MPI scan can involve two procedures: a rest test or a stress test. In a rest test, the MPI scan is completed with the patient at rest. No extra strain is put on the heart and it is imaged while beating at its normal rate. In a stress test, the heart is put under stress through the patient exercising, or through the introduction of a second pharmaceutical designed to increase the patient's heart rate [40]. Once the heart is at the required level of stress, the radiopharmaceutical is injected and the SPECT scan is acquired. Rest and stress tests are often taken in pairs to compare the images and identify blood flow defects that might be correctable. The order of the tests depends on the preference of the particular nuclear medicine department [41],[40].

Figure 14: Example of a two-head SPECT setup, with heads of 76 ° to each other. Image from [43].

MPI scans are most often conducted using two gamma cameras, often set at an angle of 90° or 76° from each other (Figure 14). The two cameras together can rotate a range of 180° around the heart, which is typically placed at or close to the centre of rotation for the gantry [4]. The angle of rotation of the heads covers mainly the front and left hand side of the chest, as the right and back of the chest provide areas of greater scattering [3]. The collimators commonly used for MPI scans using ^{99m}Tc based agents are Low Energy High Resolution (LEHR) parallel hole collimators [42]. The septa on these

collimators are thinner than the ones used for high energy gamma photons, as lower energy photons are more easily absorbed via photoelectric process and so require less lead to absorb them [26].

2.5.1 Current Hospital Protocol

The Nuclear Medicine Department at Christchurch Hospital follows a one day rest-stress protocol for the majority of MPI scans [41]. For each of the rest and stress stages, a static image is taken first, at 70°, followed by the gated tomographic acquisition. The tomographic acquisition is taken with the two detector heads placed 76° apart and rotating around the patient in 37 steps. The two head system rotates a total of 104° during the acquisition, collecting images across a 180° range around the patient.

The administered activity depends on whether it is being injected for a rest test or a stress test. At Christchurch Hospital, the range of activity for a rest test is 300 – 400 MBq. The range of activity for a stress test is 900 – 1000 MBq [41]. The optimisation of these ranges is the purpose for which a SPECT simulation is being developed in this thesis.

2.6 Previous Optimisation Studies

While the optimisation of activity for a myocardial perfusion scan has been studied previously, there is still no agreement as to the best scaling technique for patients with a large body habitus. SPECT set up and administration protocols change from department to department, affecting how the administered activity needs to be scaled to produce diagnostic quality images. Looking into how previous optimisation studies have been conducted can help shape this study. By becoming familiar with previous studies in terms of what kind of data they used, what activity ranges they looked at and how they interpreted image quality, this study can be designed most efficiently.

The studies analysed below all related to adult patients, particularly those with average to large body habitus. There are other techniques in place that would be worth involving in future studies to accommodate for adults with smaller than average body habitus, or paediatric patients.

Previous studies of the adjustment of administered activity for myocardial perfusion imaging are based largely on clinical data that either have been gathered for the purpose of the study or are gathered retrospectively from scans previously performed in the clinic. Some studies collect data over the course of several months, only using scans that come back normal [44]. Others use data retrospectively that the clinic has collected over the past several years of regular study [45].

Often in a clinical study of optimisation, a standard amount of administered activity is used as a starting point; to test it gives clinical quality images. Some studies used a set amount of administered activity across a range of different body sizes [46], [47]. Other studies [48] kept a fixed administered activity up to a threshold of 90 kg, above which they applied a correction to factor in the greater tissue volume. One example uses the following equation (Eq. 4) [48]

$$AA = \frac{W}{70} \times 600$$

Eq. 4

Where

Symbol	***Meaning***	***Units***
AA	*Administered Activity*	*MBq*
W	*Patient Weight over 90 kg*	*Kg*
70	*Weight of Average Adult*	*Kg*
600	*Administered Activity used up to 90 Kg threshold*	*MBq*

In a key study [49], the patients' administered activity was adjusted to observe the change of image quality. In this case, they adjusted the administered activities based on a recommendation from an IAEA publication [50] (Eq. 5).

$$AA = \frac{259}{\left(\frac{W}{70}\right)^{\alpha}}$$

Eq. 5

Where

Symbol	***Meaning***	***Units***
W	*Patient Weight*	*Kg*
259	*Recommended average administered activity for patients up to 70 kg*	*MBq*
α	*-0.871 (^{99m}Tc-MIBI) or -0.834 (^{99m}TC-tetrofosmin)*	*-*

According to the original publication of Eq. 5 [50], the scaling factors applied were designed to maintain patient radiation dose across the range of patient weights, and so did not necessarily relate to image quality.

Another example of using adjusted administered activities over a certain value is from Notghi et al. [44], who adjusted their administered activity according to a table they developed during their 2003 study (Table 1). This table adjusted the administered activity by weight for patients over 100 kg.

Table 1: Table of injection activity for patients of weight greater than 100 kg, proposed by Notghi et al. (2003) and used in their 2008 study [47]

Patients weight (kg)	Injection activity (MBq)
100-109	520-570
110-119	570-630
120-129	640-710
130-139	720-820
140-149	830-960
>149	1000

In a study of optimization, a metric must be defined to compare the reconstructed images. There were several ways previous studies did this. Papanastasiou et al. [49] used the ratio of detector count rate to administered activity as one test to show that, when following the recommended IAEA protocol for activity scaling [50], image quality was not affected by weight. They also looked at the relationship between normal myocardial mean count rate, with and without attenuation correction, and the administered activity.

As a further test of image quality, Ramon et al. [45] inserted lesions into their reconstructed data and ran the images through clinically validated model observer software. This allowed them to see which activity levels allowed the lesions to be reliably detected in a clinical setting.

A qualitative test of image quality that has been used involves experienced physicians assessing the quality of the reconstructed images and asking the team of assessors to determine the clarity of the images using a five point scale [10], [13], [51]. An image given a 5 was of clear clinical quality; an image given a 1 was extremely unclear. An image with a rating below 3 was considered not fit for clinical use. This technique for image quality rating is subjective as the experience of each physician will affect their confidence and accuracy in stating the image clarity.

The potential problem with each of the above studies is that they each rely solely on the weight of the patient. While in general, weight may be an acceptable variable for providing an initial estimate on how much activity may be required, in order to keep the administered activity level as low as diagnostically feasible, other body measurements would be required. Two patients of the same weight but different height would be very likely to have a different chest circumference, which would affect the detected signal. Getting a large enough sample of patient heights and weights to give a clear indication on the effect of each variable, without undue influence from other random variations, would be a time consuming process.

2.6.1 Simulation Studies

As seen above, several studies on administered activity optimisation have been conducted at a clinical level [13], [44]–[46], [49]. These studies face one problem that limits the rigorousness of the optimisation tests: they rely on human patients, for whom it is unknown at the time of the study whether a lesion is present or not. There are also strict guidelines surrounding the experimentation of administered radioactivity in clinical trials. In a simulation study, the patient is represented by a phantom which has a known state (defect or normal) [52] and for which there is no restriction of justifying the level of administered activity. In those phantoms with lesions present, the size of each lesion is known and this size can be varied across the test series. Another benefit of a simulation study is that several simulations can be run with identical initial conditions, which allows for controlled testing of a particular parameter that is difficult to accomplish in a clinical study [52].

A disadvantage of a simulation study is the time each simulation takes to complete, especially when using Monte Carlo methods. This time is long because each photon and secondary particles produced in the simulation are tracked from the source until they either exit the simulation volume (the simulation "world"), or are absorbed. This occurs for every photon produced even though only around 0.02% of the total number of events contribute to counts in the image [15]. To counter this, the geometry and physical processes being modelled can be simplified to reduce the computational time [52]. The level of accuracy needed in a simulation determines the approximations that can be made by the simulation. For example, in a simulation tracking photons passing through a medium, any electrons that are released during the process can generally be ignored by the simulation calculations, reducing computing time.

2.7 Monte Carlo Methods

The Monte Carlo method uses random number generation and probability distribution functions (PDFs) in the simulation of a specific situation [15]. For the simulation of radiation transport to take place, there is information about the simulation that it is necessary to define – for example, a description of the radioactive source including the half-life of the modelled radionuclide, the type of particles produced, and their energy. Other necessary information includes the geometry being simulated, the materials of each object and the time frame the simulations occurs over. Which particle decays, the direction it travels in, how far it will travel, and the kind of interaction it has with the material it passes through is based on the known statistical probability (based on the PDF) of that event occurring and the random number generated [53].

A PDF is a way of expressing the likelihood a continuous variable has of falling within a range of values. All the information given to the program about the scenario being simulated affects the probability of a particular outcome occurring. For example, the type of radionuclide being modelled affects the emitted particle type and energy. Its type affects what kind of interactions it might have, and its energy affects how far it might travel before those interactions might take place. The density of the medium the emitted particles are passing through also contributes to the probability of particular interactions taking place.

For example, if the simulation is set up to produce 100 primary particles, the random number generator will produce 100 random numbers, each relating to a primary particle – i.e. either a photon or an electron. In a simulation that produces photons 80% of the time and an electron 20% of the time, the probabilities for each are 0.8 and 0.2, respectively. The random number generator is based on a PDF which defines the relative probability of each number in the range being generated. In this example, any number is equally likely, so the PDF would be flat. Other examples may use a Gaussian shaped PDF or a stepped function. For this example, the random number generator might produce numbers 1 – 700 with equal probability. If the generator produces a number that is 560 or below, a photon is produced. If the number is 561 or above, an electron is produced. Each primary particle is then followed with each step being defined based on a calculation utilising subsequent random numbers, based on appropriately shaped PDFs, and the probability of being absorbed, scattered, or transmitted guiding the progress of each particle through the simulation.

The ability to produce a string of uncorrelated, yet reproducible, random numbers is an important part of any Monte Carlo random number generator. The period of the string, or how many numbers it can produce before it starts the loop again, must be long, to account for the number of particles being tracked through a given simulation.

The initial number given to the random number generator is called the seed [54]. The seed is what the next number is generated from, meaning the same seed with the same random number generator will give the same series of random numbers. While this can be useful when comparing the output of two systems, to ensure they are set up identically, other situations require each simulation to start with a different seed, to produce a different string of random numbers.

There are many scenarios that can make use of Monte Carlo modelling, particularly those relating to physical situations that don't have a simple analytical solution. One early example of Monte Carlo style techniques was used to calculate the value of π [55]. With widespread use of digital computers, Monte Carlo has become well known in the medical physics community for its usefulness in particle tracking simulations, both in dosimetry and in imaging.

2.8 Simulation Software

Several Monte Carlo codes have been developed for medical physics. Some are optimised for dosimetry and therapy planning, while others are designed for imaging modalities. There are some toolkits and programs that have the capabilities to do both, but most are originally designed with one aspect in mind and only later expanded to a wider field. This section looks at some examples of Monte Carlo codes, ranging from general purpose to specific focus. Some require advanced computer science skills to be able to be used. These options often have the most flexibility when it comes to what the user is able to model but the extent of its capabilities are often not easily understood by most users [56]. Others require little computer science knowledge, but because of this are rather inflexible in what can be modelled. These programs are often designed for simulating a particular modality (only SPECT or only PET, for example) which can greatly increase the speed of the calculations due to the limited range of particles and energies the program is designed for [57]. Others fall somewhere in between on a spectrum of flexible but complex to specific and user friendly.

The Monte Carlo simulation toolkit for Geometry and Tracking (Geant4) is a complex toolkit. It is written in C++ and was developed as a collaborative project between scientists across the world, for use by CERN at the Large Hadron Collider (LHC) [58]. The strength of Geant4 is its modelling of the physics of different interactions, along with its ability to model a large range of particles and energy levels [59]. As it was not originally designed with nuclear medicine in mind, a drawback of Geant4 is that it can be difficult to tailor to SPECT and PET [60]. To do so would require experience with C++ and a significant amount of time available to dedicate to development. Due to this difficulty, applications were created to harness the capabilities of Geant4, in a more user friendly environment. Two examples of such applications are GATE and TOPAS.

The Geant4 Application for Tomographic Emission (GATE) was developed by the OpenGATE Collaboration [60]. Built on the powerful Monte Carlo calculation capabilities of Geant4, GATE was developed to allow the user to access what Geant4 had to offer, without needing to understand C++ coding [60]. Rather, the user can set up and run simulations to their specifications using simple text files called macros. Within these macros the user defines each part of the simulation – geometry, physics, source, acquisition time, and detector digitization. Within a macro, a user can call other macros, which results in a user being able to set up one main macro which calls all the required components for that simulation in a modular fashion. Each component can then be used in multiple simulation definitions, or for the same setup to be tested with varying levels of geometric complexity. This allows GATE to keep a lot of its flexibility while being straightforward to understand and use.

The focus of GATE is on medical imaging and radiotherapy. Complicated detector geometries can be modelled within GATE, while still providing full access to the physics libraries within Geant4 [60]. A strength of GATE over other Monte Carlo simulation programs, in regards to this project, is its ability to manage the decaying of sources over time. It also has the ability to accurately and simply define the detector geometry and electronic characteristics, as well as other time-dependent phenomena [15]. A weakness of the program is that GATE is not multi-threaded – each instance of GATE can only run a simulation on a single CPU at a time. This reduces the potential processing power available for a given simulation, increasing the time required for the calculations to take place. While GATE can simulate highly accurate detector and source set-ups, the payment for this is a reduction of simulation speed.

The Tool for Particle Simulation (TOPAS) was also developed using the Geant4 toolkit[56], so, again, users would not need to write C++ [16]. TOPAS was originally developed for proton therapy but has been further developed for use in radiobiology modelling, x-ray and electron therapy, and medical imaging [16], [56]. A computing advantage of TOPAS is that it is inherently multithreaded, meaning it automatically spreads its workload over available CPUs to decrease computation time [16]. A point of interest, in differentiating the use of TOPAS and GATE, is that while GATE was originally designed to simulate tomographic studies [60], TOPAS was originally designed to simulate proton therapy and other areas of radiation therapy [61]. Both GATE and TOPAS have developed beyond their initial scope but their strengths still align with their original uses.

There are other Monte Carlo codes that can be used for nuclear medicine outside of those developed with Geant4. For example, the Simulating Medical Imaging Nuclear Detectors (SIMIND) Monte Carlo program is designed for use in simulations of SPECT scans [52]. It is written in FORTRAN and made up of two programs, SIMIND and CHANGE [17]. CHANGE is where the simulation is defined, through a menu-driven method that then writes the simulation parameters to an external file. This file is read by SIMIND, where the calculations are done, and the results are written to a data file [52]. Due to its focus on SPECT scans, therefore not incorporating the particle interactions that do not contribute to the simulation intentions, the speed of the simulations are faster than those of general application software [57]. The downside to SIMIND is that it has a limited ability to simulate complicated detector geometries meaning not all systems can be accurately modelled. The choice of simulation software for this project is discussed in Section 3.1.

2.9 Modelling of Humans Using Digital Phantoms

When simulating a SPECT scan, not only does the detector head geometry need modelling, but so does the patient anatomy. Physical phantoms, such as objects taking the place of humans in calibration tests of equipment, have been used in medical physics for quite some time [62]. Digital phantoms, for use in computer simulations, have also been developed due to their ability to be used to test a wide range of situations that would otherwise be difficult to test physically. This thesis will focus on the use of digital phantoms, which from here on will be referred to simply as “phantoms”.

There are three main classes of anthropomorphic phantom: mathematical, voxelised, and hybrid. Each class has its advantages and disadvantages. They have been developed over time to produce phantoms that represent the human body with increasing accuracy.

Mathematical phantoms have surfaces that are described by equations [63]. These phantoms are easily adapted to represent different sizes of patient just by changing the coefficient of the surface equation. However, they are limited to simple geometries, such as ellipses and rectangles, to describe shapes due to the increased complexity of equations describing complex volumes.

The Mathematical Cardiac-Torso (MCAT) phantom is an example of a mathematical phantom [64]. The MCAT phantom (Figure 15) is constructed using basic geometric shapes to represent various organs,

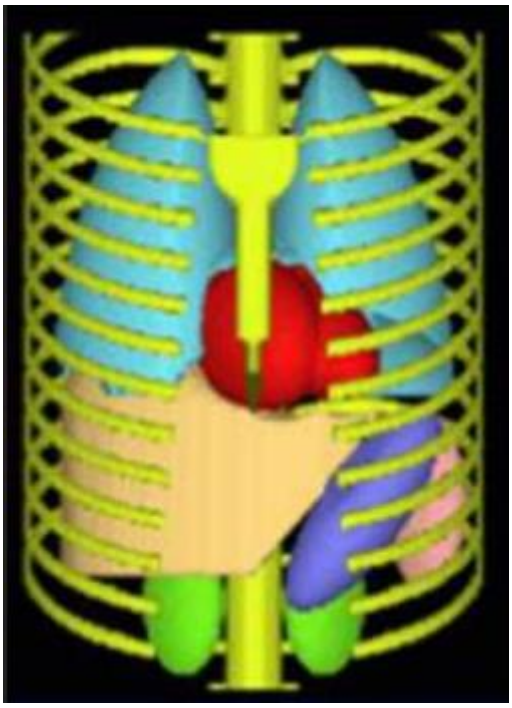

Figure 15: Anterior view of the MCAT Phantom, with organs based on simple geometric shapes. Image reproduced from [62].

with overlap and slices being used to more accurately represent organ shapes in comparison to previous mathematical phantoms [62], [65]. The phantom has two modes: creating an attenuation map based on a given photon energy, and creating an activity map based on a given distribution of a particular radiopharmaceutical [66]. As it is a mathematical phantom, the MCAT can be made any size or resolution before it is stored as a voxelised phantom to be imported into the simulation software. Despite being more geometrically correct than previous mathematical phantoms, the MCAT is still a reasonably crude approximation of human anatomy.

Voxelised phantoms can better represent the geometry of the human body. However, they do not have the same flexibility in changing size as the mathematical phantoms. A voxelised phantom is normally created from a medical image, such as a computer tomography (CT) scan [67]. It is a three dimensional representation of the image data, broken down into voxel volumes, analogous to the way a picture is broken down into pixel areas [68]. The size of these voxels determines the resolution of the phantom. While this results in highly accurate phantoms, the voxels limit the scaling that can be applied to the phantom.

Hybrid phantoms are designed with the accurate geometry as described by voxelised phantoms but are coupled with the flexibility of change that the mathematical phantoms contain. This is done by using a Non-uniform Rational B-Spline (NURBS) surface [62]. This surface is controlled by a grid of control points which can be adjusted easily to change the shape or size of a phantom, while keeping an accurate physiological representation.

The NURBS-based Cardiac-Torso (NCAT) phantom (Figure 16) was developed in response to some of the problems in the MCAT phantom [69]. Created using NURBS surfaces, the NCAT phantom is an example of a hybrid phantom. Using the multiple control points that are present on a NURBS surface,

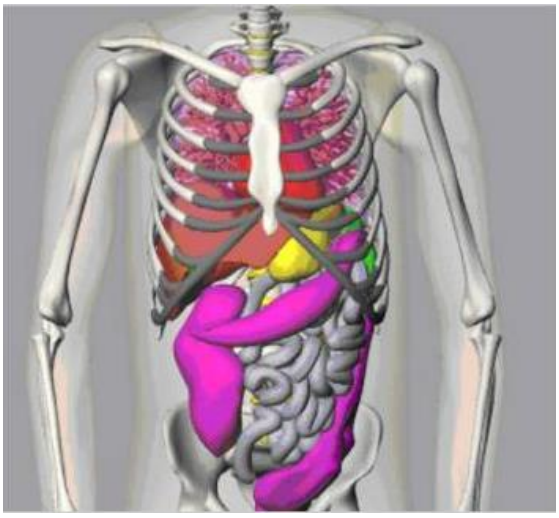

Figure 16: Anterior view of the NCAT Phantom. Image reproduced from [69].

more complex geometries are able to be created, without the computational increase that more complex mathematical surfaces require [62]. While the NCAT phantom is far more anatomically correct than the MCAT, they both have the shortcoming of only being modelled as male phantoms. When a female phantom is used, the user defines an amount of breast tissue to place on the chest, with all other dimensions based on the male CT data used to create the phantom [66].

The Extended Cardiac-Torso (XCAT) phantom is the next generation of the NCAT phantom. Rather than just modelling the torso, the XCAT phantom models the whole body. Also, XCAT has both a male and female definition, developed separately [70]. The XCAT phantom was developed with greater detail than NCAT, so it could be used for simulating high resolution modalities, not just the low resolution modalities that MCAT and NCAT were originally developed for [66].

The XCAT phantom (Figure 17) is the most up-to-date of the NURBS phantoms and is well recognised as being anatomically accurate [71], [72]. Within XCAT, there is the option to create 3-dimensional activity and attenuation maps and import these into GATE as voxelised phantoms. The attenuation map is used as the phantom itself, while the activity map indicates to the simulation where the activity is located, and at what levels. It is also possible to export the phantom from XCAT as a mesh. With this option, each organ is imported into GATE individually as a stereolithography (STL) file. STL files represent the surface of an object as a mesh of triangular planes. Each STL file has a material assigned to it. While this second option is more time consuming in its set up than importing the voxelised

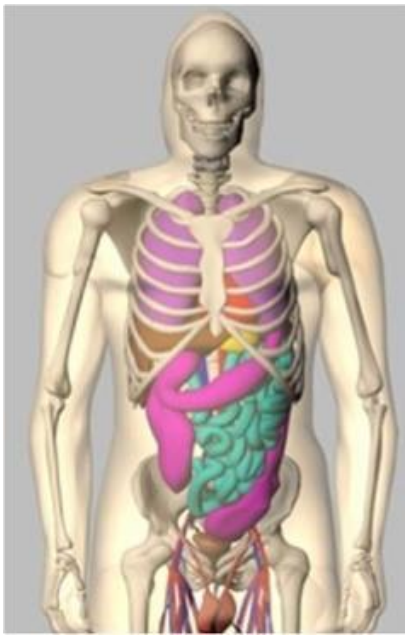

Figure 17: Anterior view of the XCAT Phantom, which extends beyond imaging only the torso and can include smaller structures such as veins and nerves. Image reproduced from [69].

phantoms, the simulation calculations can be completed faster as the photons are not stopped at each voxel boundary for their interaction likelihood to be recalculated. Within the STL file the material is homogeneous so one calculation can be done upon entering, to find the average distance the photon will travel before interacting, and it can travel this distance before a further calculation needs to be done, or it reaches a boundary with another STL file.

2.10 Image Quality

To quantitatively assess whether images obtained with varying amounts of activity or across a range of patient sizes are diagnostically different, image quality metrics need to be defined. Commonly used measures of image quality are contrast, spatial resolution, signal-to-noise ratio, and contrast-to-noise ratio. These measures can be used in a range of combinations and are formally defined below.

In Section 2.4, spatial resolution was used to describe the quality of images acquired with a gamma camera and was discussed in terms of intrinsic and extrinsic resolution. This section is looking at the quality of the image, depending on the system as a whole. A system's spatial resolution describes the level of detail that can be seen on an image (Figure 18). The spatial resolution of a system can be found through the Point Spread Function (PSF), which describes how much an image of a point source is blurred, compared with the original source [73]. As a line source can be approximated as a string of point sources, a point on a line source can be used to find the PSF. Two objects can be distinguished as different if they are separated by a distance greater than the full width half max (FWHM) of the PSF [74]. In most cases, the PSF can be approximated by a Gaussian, meaning the resolution of a system can be measured by the FWHM of a Gaussian fitted to the profile of a line source [73]. The closer together two object can be, and still be identified as separate objects, the better the spatial resolution.

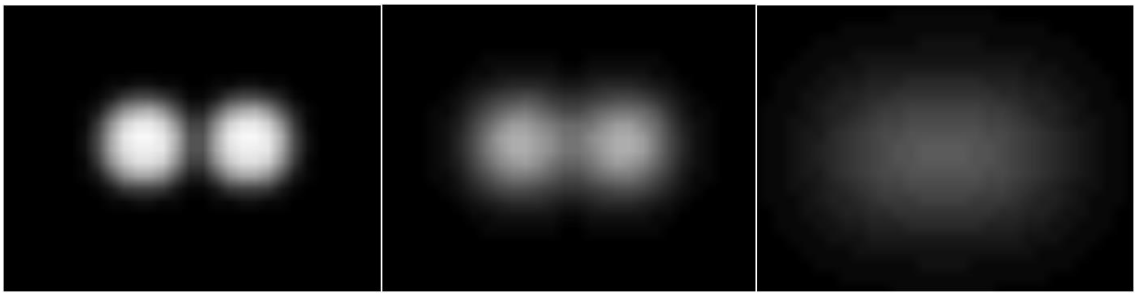

Figure 18: Image of two point-like sources with increasingly poor spatial resolution

The contrast resolution of a system relates to the ability to observe subtle changes in grey scale when using that system [39]. This is particularly important when trying to distinguish a subtle change in the grey scale of the object being imaged from noise in the image, such as the presence of a defect in the myocardium reducing the grey value of the pixels in its image. The main source of contrast within a

nuclear medicine image is the difference in signal between an area of high activity uptake and an area of low uptake [75].

The contrast-to-noise ratio (CNR) is a measure of the strength of an object's signal compared to a noisy background (Eq. 6) [51]. CNR is independent of the size of the object being viewed, as it uses the average signal of both the object and background [39].

$$CNR = \frac{|\mu_1 - \mu_2|}{\sqrt{\sigma_1^2 - \sigma_2^2}}$$

Eq. 6

Where

Symbol	***Meaning***	***Units***
μ_1	*Average signal of object of interest*	*Counts*
μ_2	*Average signal of background*	*Counts*
σ_1	*Standard deviation of* μ_1	*Counts*
σ_2	*Standard deviation of* μ_2	*Counts*

The signal-to-noise ratio (SNR) is a measure of an object's ability to be seen in an image (Eq. 7) [51]. While similar to the CNR, SNR is dependent on the size of the object as well as its signal strength [39]. CNR is a measure of the difference in average signal between two areas of the image, whereas SNR is a measure of the total signal of an object within an image. The *Rose Criterion* states that an object will always be detectable with an SNR ≥ 5 [76].

$$SNR = \frac{\mu}{\sigma}$$

Eq. 7

Where

Symbol	***Meaning***	***Units***
μ	*Average signal of object of interest*	*Counts*
σ	*Standard deviation of the image background*	*Counts*

It is important to use a range of measures of image quality, rather than relying solely on one, because of the different information provided by each assessment. For example, to talk only about SNR does not take into account the difference in signal in different parts of the image. The SNR is an indication

of whether an object can be seen, while contrast or CNR are an indication of whether two areas of different signal strength can be distinguished. For this work, SNR and CNR will be used as the main measures of image quality.

2.10.1 Screen Quality

As well as the quality of the image, another important factor is the quality of the screen the images are viewed on. A high resolution image will still appear low resolution if it is viewed on a low resolution screen. To ensure the resolution of the screen meets diagnostic quality, standardised test patterns are used to find optimal settings of contrast and brightness for a screen. One such pattern is the American Association of Physicists in Medicine Task Group 18 Quality Control (AAPM TG18-QC) test pattern (Figure 19) [77]. The test pattern is made of several different regions, each evaluating a different aspect of screen image quality. Areas being evaluated include geometric distortions, luminance response, resolution, contrast detectability and contouring artefacts [77].

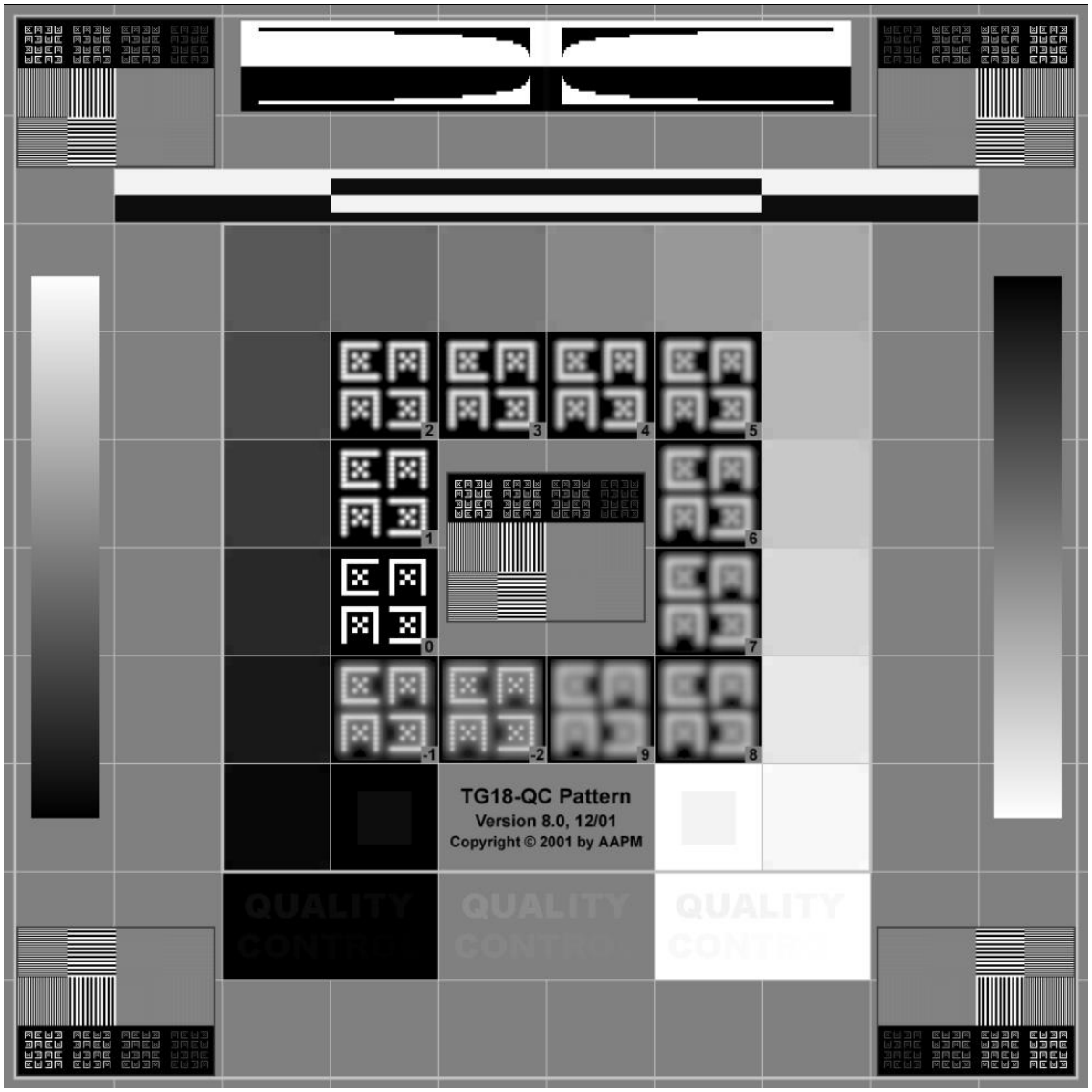

Figure 19: The AAPM TG18-QC test pattern used to assess the image quality of a computer display. Figure reproduced from [76].

3 Methods

This project took place over three stages – simulation development, phantom characterisation, and a proof of concept application. The proof of concept study is built on the first two sections, with both the simulation and the phantom first being validated. The method for each stage is outlined in this chapter.

3.1 Development of a Monte Carlo simulation

This part of the thesis focuses on the development of a Monte Carlo simulation to model the clinical use of a SPECT system. The system being modelled is the Symbia T2 gamma camera at Christchurch Hospital, as it is used for MPI scans. Section 3.1.1 discusses the choice of Monte Carlo software. Section 3.1.2 covers the development of the system, while Section 3.1.3 outlines the validation of the simulation system against a Symbia T2.

3.1.1 Simulation Software

As outlined in chapter 2, there are several options of software that could be used to set up the simulation, and it was a matter of deciding which combination would be the best fit for the situation being modelled. The software chosen for this project was the latest version (at the time of writing) of GATE (version 9.0). It has significant flexibility in the simulation set up, compared to some of the other available software, and the macro files are written following a command structure that is relatively easy to learn. The openGATE Collaboration [78] has a mailing list set up for all GATE users, through which further support is available to the user and software developments can be followed. While becoming familiar with GATE, and while developing simulations, a virtual GATE environment, vGATE, can be used without the need for a native install. This allows the user to develop and test a simulation on a virtual machine. GATE does have the disadvantage of slow simulation times, due in part to its high level of accuracy in modelling the interactions taking place. The fact it is not multithreaded also increases the time simulations take to complete. There has been discussion within the GATE community about making GATE multithreaded, but due to the nature of the legacy code, there is reluctance to do so in case it creates a range of new errors within the program. The problem of simulation speed has prompted the development of simulation acceleration techniques that can be applied to reduce the effect of this problem as discussed in Section 3.2.2.

3.1.2 Simulation Development

The simulation produced in this thesis was built using an example provided in the GATE GitHub repository [79] as a starting point. This example provided most of the components required to accurately simulate a SPECT detector head. Using the specifications provided in the Symbia T2 Manual [80], the sizes of each layer of the detector were applied and the crystal and collimator were set to the correct thickness. The final settings are shown in Appendix A.

A key addition to the example code was providing the ability to model two detector heads at once. Real SPECT systems often use two detector heads, so creating a model with two detectors was essential to make the simulation realistic. The addition of a second head also allowed the simulation to run faster than if each angle had to be simulated individually. There were several ways to do this outlined in the GATE manual. One option was to create two separate detector heads and place them manually. This would require specifying the Cartesian coordinates and rotation angle for each detector head in every projection angle as they rotated around the patient. A simpler solution was to use the "circular repeater" function, which copies the original detector heads and places the copies at given intervals around a circle. It was possible to use this function to place two detector heads so they were separated by the required 76°. For the detector heads to be 76° apart, the angle entered into the repeater function had to be 104°, due to a difference in the point of reference (Figure 20). The repeater function defines the angle as that around the origin of the simulation setup, whereas the program

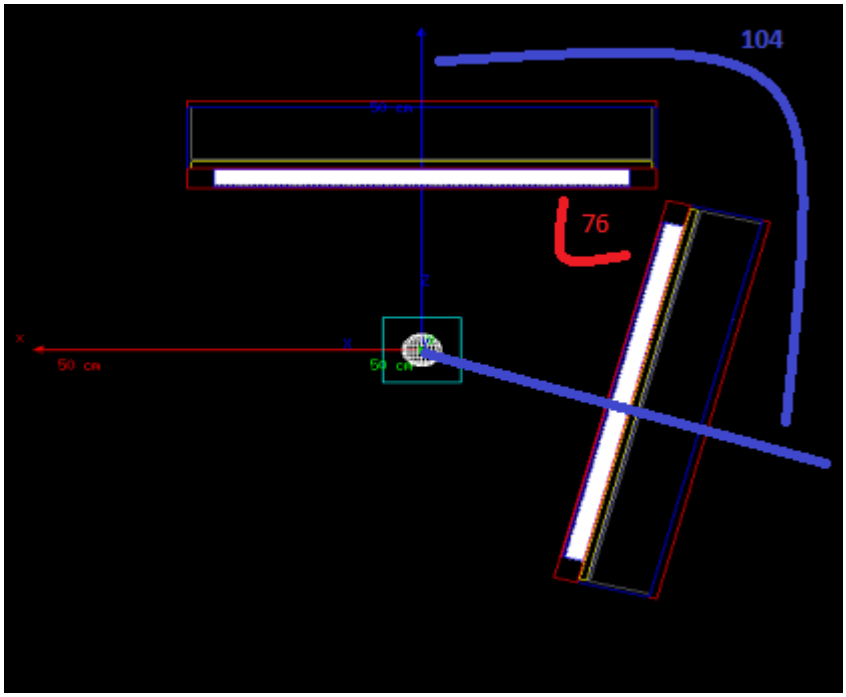

Figure 20: Detector head positions, relative to each other. For the required 76° between the two heads (red arc), the second head was placed at 104°, measured from the setup origin (blue arc).

controlling the placement of the gamma cameras at Christchurch Hospital defines the angle as that from camera 1 to camera 2. Then, when the new position for one head was given for each new projection image, the other was automatically placed correctly. The down-side to this method was that the two heads could not have their radii of rotation changed independently of each other, making simulation of body contour imaging impossible.

The circular repeater approach avoided a scoring issue that the manual placement approach had. In the manual placement approach, when two detector heads were specified within the macros, a bug in the GATE code meant only detection information from the first detector head would be recorded in the output. This error was present whether one system was identified with two detectors associated to it, or two separate systems identified with a single detector each. The circular repeater approach allowed two detector heads to be present and detection data to be recorded -Z both. Therefore, even though radii of rotation were not independently movable, the circular repeater approach was taken. It was the approach that reliably gave the correct relative placements and allowed collection of data from both detector heads.

Section 2.1 of this thesis described the purpose of PMTs. In GATE, the simulation of the PMTs was performed by a piece of code called the digitizer. While the electronics themselves were not modelled, the potential scattering effect of these electronics was modelled by an 8 cm thick block, allocated the material type “Pyrex” [81].

Another important alteration to the original script was in the orientation of the collimator septa. When adjusting the septa to fit the specifications of the LEHR collimator, the resulting test output appeared to have greater septal penetration than was expected. In a hexagonal-hole collimator, partial penetration of the septa by the incident photons results in a staring effect when viewing a point-like source. The number of rays seen is expected to be six, due to the six sides of each collimator hole. This setup was producing 12 (Figure 21A). Close inspection of the septa arrangement in the simulation showed the hexagons were incorrectly aligned in the GATE provided example. Correcting this, by changing the repeating vectors used to make the holes, resulted in the number of septal penetration rays being reduced to six, as expected (Figure 21B). This finding was brought to the attention of the GATE developers and has been corrected for future updates. This result demonstrates the importance of simulation verification.

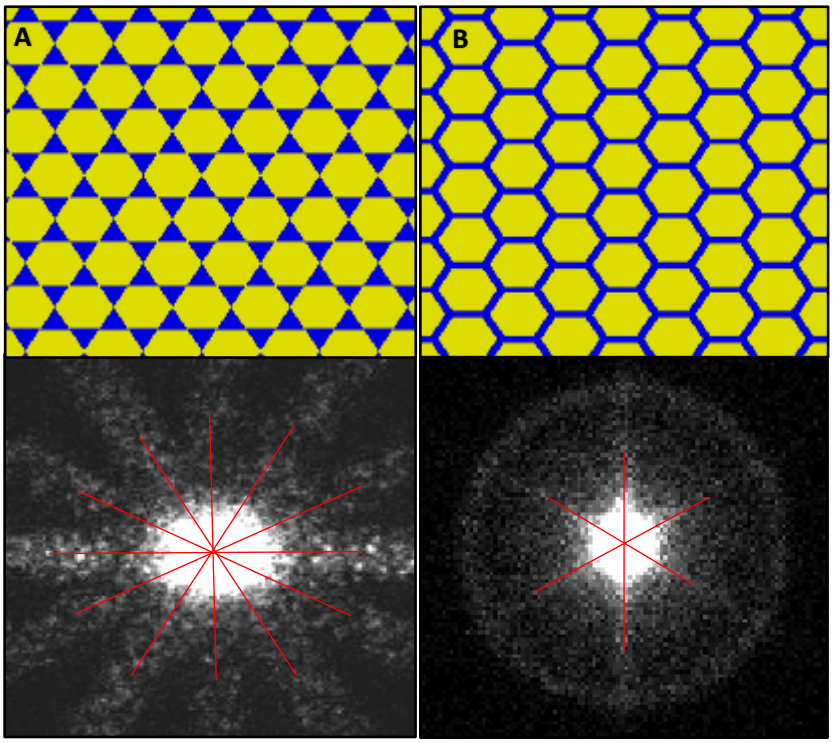

Figure 21: A: A visualisation of the original arrangement of collimator holes (yellow) and septa (blue) in the simulation collimator (top) and Projection image of a point source with the original collimator settings (bottom). B: The updated arrangement of collimator holes and septa, matching the arrangement in the Hospital collimator (top) and Projection image of a point source with the updated collimator settings (bottom). Red lines indicate the "rays" caused by septal penetration.

3.1.3 Simulation Verification

Before beginning the phantom simulations, the simulated gamma camera was validated against the Symbia T2 gamma camera used clinically in Christchurch Hospital. The specifications for the detector head of this system [80], particularly the crystal size and collimator specifications, were used to model the system in GATE as closely as possible (Table 2).

Table 2: Specifications for Symbia T2 Gamma Camera, as outlined in [80].

Symbia T2 Specifications for MPI Study	
Detector Field of View	53.3 x 38.7 cm
Crystal Size	59.1 x 44.5 cm
Crystal Thickness	9.5 mm
Collimator type	Low Energy High Resolution (LEHR)
Hole Shape	Hexagon
Hole Length	24.05 mm
Septal Thickness	0.16 mm
Hole Diameter (across flats)	1.11 mm

To test how accurately the simulation represents the Symbia T2 gamma camera, a series of tests were performed that mimic those carried out on the gamma camera at Christchurch Hospital as part of regular quality assurance checks. These tests are designed to measure the spatial resolution, energy resolution and count sensitivity of the gamma cameras.

A line source phantom is commonly used to measure the spatial resolution of a SPECT system [50]. To measure the spatial resolution of the simulation SPECT system, the specifications of the line source phantom used at Christchurch Hospital were used to create an equivalent digital source within the simulation software. The phantom was setup with the source positioned vertically, the detector head at 90°, a radius of rotation of 20.2 cm, and set to simulate 120 MBq of ^{99m}Tc for 10 minutes. The projection image was analysed with ImageJ (v1.52a), where a profile of the image intensity was plotted. The FWHM was then measured by transferring the profile plot to MATLAB and fitting a Gaussian to the data. The FWHM was taken from this plot and compared with the FWHM found using the same process on the projection image obtained by the clinical SPECT system.

Energy resolution was measured by collecting the energy spectrum using the GateToTree class of GATE output. The energy of each hit within the detector crystal was recorded in a text file. This was then opened in MATLAB and a histogram was created to represent the energy spectrum. A Gaussian was then fitted to the histogram, from which the FWHM was read and matched with the measured clinical SPECT energy resolution.

A measure was also made of the extrinsic uniformity of the simulation output. A flood field source (60 cm x 40 cm, 100 MBq) was simulated 1 cm in front of the face of the detector head (Figure 22). A total of 60 seconds were simulated, split across 60 CPUs, each with a different seed. The outputs were then added together in ImageJ, to produce the final flood field image. This image was inspected for uniformity using the ImageJ “Plot Profile” tool.

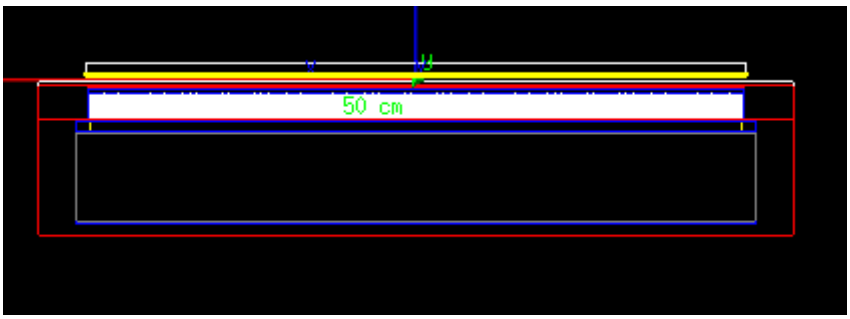

Figure 22: Simulation setup to measure the extrinsic uniformity of the output. A flood filed source (yellow) was simulated 1 cm above the face of the gamma camera (red outline).

Due to the computational demand of the study, three different servers were used to maximise the number of CPU cores available to run projections. The University of Canterbury linux servers were Puppis, with 10 of 40 CPU cores available, Fornax, with 20 of 24 CPU cores available, and Curie, with 100 od 104 CPU cores available. Each server had the same version of both GATE installed. The specifications for each server are outlined in Table 3.

Table 3: Specifications of the servers used (Puppis, Fornax, Curie)

	Puppis	Fornax	Curie
CPU(s)	40	24	104
Model name	Intel® Xeon® Silver 4114 CPU @ 2.20GHz	AMD Ryzen 9 3900X 12-Core Processor	Intel® Xeon® Gold 6230R CPU @ 2.10GHz
CPU max MHz	3000	3800	4000
CPU min MHz	800	2200	1000

To ensure the same results would be achieved using any combination of cores, a test simulation was designed. In this simulation a 120 MBq line source was placed between two detector heads, separated by 180°. The seed engine chosen was Mersenne Twister, with the same seed value of 20210608. The simulation was completed on a single CPU of each server, and outputs compared.

3.2 Characterisation of a Digital Phantom

Within a SPECT simulation, there are two important sets of geometry that need to be included – the detector (described above) and the patient. This chapter describes the process of correctly characterising the chosen digital phantom, and including it within the developed SPECT simulation. As simulation time is a major consideration for this project, an effort was made to reduce the time a simulation took to complete. These techniques are outlined in Section 3.2.2

3.2.1 Phantom Preparation

The digital phantom chosen to represent human anatomy in the simulation was the 4 dimensional extended cardiac-torso (XCAT) phantom developed by Professor Paul Segars [70]. The phantoms were produced either in voxelised form or in mesh form. This project implemented the mesh files option due to their contribution to reducing the simulation time. In voxelised phantom form, each voxel is viewed by the passing photons as a different volume, and the mesh phantoms are believed to help decrease the time of the simulations as the only boundaries are between different mesh files, reducing

the number of boundary-related calculations [82]. The meshes are also able to be visualised within GATE, whereas the voxelised phantoms are only represented by a single slice, which makes ensuring the system is aligned correctly much simpler.

The XCAT program produces six files in raw triangle format: body, heart, organs, veins, muscles, and bones. The body file provided the skin outline of the phantom, encapsulating the whole body volume without containing any other organs itself. All the other files fit within the body file. The organ file needs to be separated out into the different organ types as, within GATE, one mesh file can only have one material associated with it. To reduce the number of boundaries, and therefore decrease the simulation time, some of the detail of complex organs were removed. This included using only the outer surface of the brain, lungs and kidneys. As these organs were not the focus of the study, their main function was to mimic the scattering environments the photons emitted from the heart pass through, from the heart to the detector. As long as the overall material of the lungs were “lung” and the shape, size and position was correct, the inner detail did not serve to increase the accuracy of the simulation enough to account for the increase in time that the detail would cause. Also, not every organ was included, with priority given to those nearest the heart and therefore most likely to be involved in scattering events. The organs included were:

Brain, Lungs, Stomach, Liver, Kidneys, Small and Large Intestines, Pancreas, Spleen, Bones, Muscles and Skin (Figure 23). The heart was included as a source, represented by the pericardium.

The phantoms were created with no arms, and the legs were removed. This was a reasonable exclusion to make, as myocardial perfusion studies at Christchurch Hospital are completed with arms raised about the head, so they are out of the field of view of the detector. The legs are far enough away from the detector field of view to contribute very little in terms of scattering.

To use the meshes in GATE, they were converted into STL files by Rhinoceros 6, a 3-dimensional modelling program [83]. Other amendments were made to the files in Rhinoceros 6 to make them better suited to the goals of the simulation. This included choosing a specific origin point that is common to each phantom, regardless of size; separating the organ file into individual organs; and making sure all mesh vertices within the phantom were aligned.

Initially, the phantom origin point was located between and at the level of the feet. For ease of inclusion in the simulation, shifting the origin to be on the central axis of the patient, at the level of the heart in the chest was important. This translation would be possible within GATE but as the phantoms were to be of a range of sizes, having each already centred at the same point in their chest made alignment of many parts within GATE significantly simpler. The new point of origin was

transferred to the other organ files belonging to the same phantom by applying the same “Move” command, with the same start and end coordinates as determined by the “body” file.

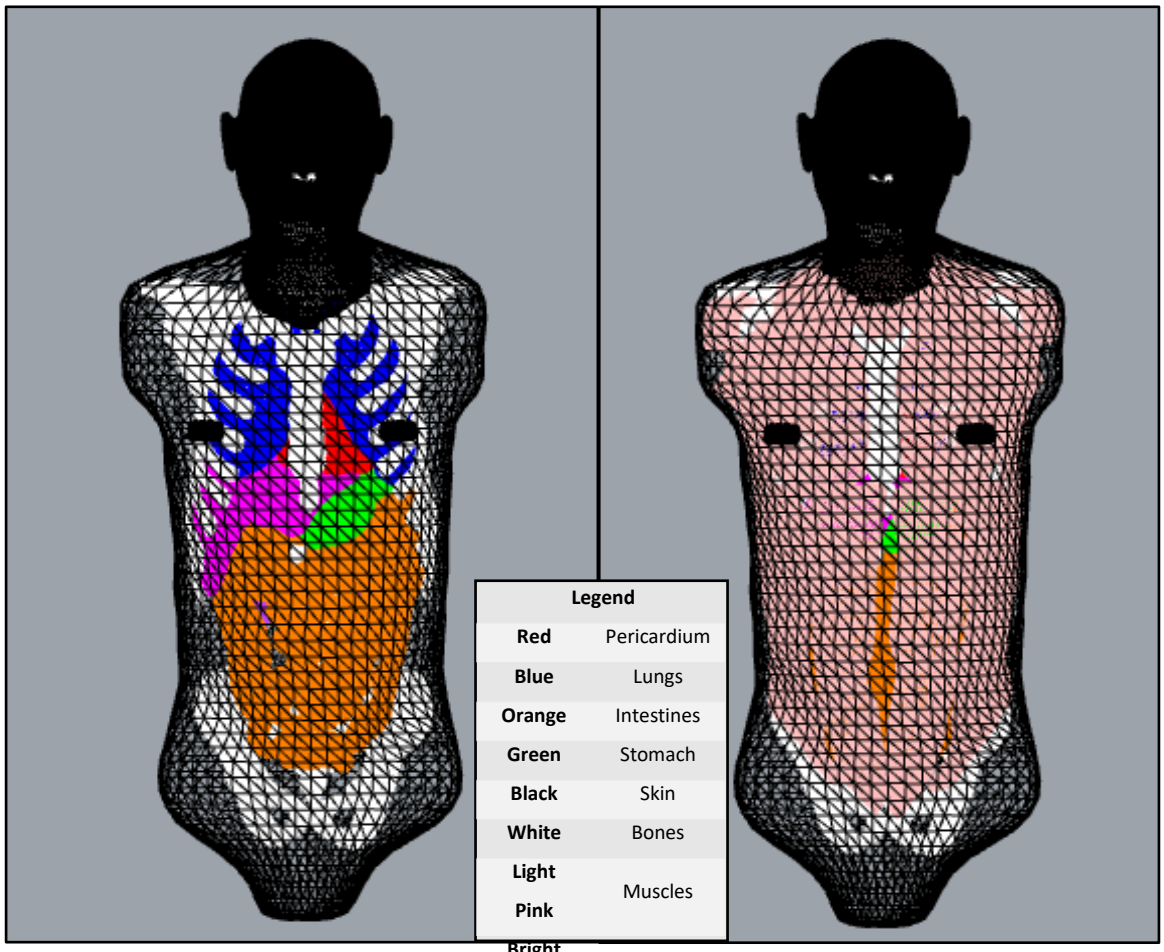

Figure 23: XCAT phantom as visualised in Rhino 6. Left: Showing organs where they are placed within the body, excluding muscle. Right: Organ location including muscles.

3.2.2 Simulation Time Reduction Techniques

As discussed in Section 1.2, a key limitation with this project was computing time. Due to this, there were several attempts made to reduce the time each simulation would take. In decreasing the simulation time, however, care had to be taken to not reduce the quality of the output to the point that it would not be useful for producing clinically relevant conclusions. The main methods used to reduce simulation time were to reduce the amount of activity being simulated, introduce phase space files as the source, and utilising more computer cores through parallelisation.

Simulated Activity

As the focus for this study was MPI scans, simulations were run using only the heart as a source. In the human body ^{99m}Tc labelled tetrofosmin is taken up not only by the heart muscle, but also by the thyroid, salivary glands, kidneys and the liver [84]. Choosing to only simulate the activity that is present within the heart wall decreased the simulation time by a factor of about 100. Using the ICRP 128 guide of fractional distribution of ^{99m}Tc-labelled tetrofosmin, for a total administered activity of 400 MBq, the uptake in the heart wall, and therefore the amount of activity to be simulated, is 4.8 MBq, or 1.2% of the total administered activity [84].

$$\begin{aligned} A_M &= A_A \times 1.2\% \\ &= 400\ MBq \times 1.2\% \\ &= 4.8\ MBq \end{aligned}$$

Eq. 8

Where

Symbol	Meaning	Units
A_M	Activity within the myocardium	MBq
A_A	Total administered activity	MBq

While the presence of activity in the blood within the ventricles of the heart will not make a large difference to the visibility of the myocardium, it was included in the simulation to get as accurate a contrast within the heart as possible, within the given time constraints. To get a realistic ratio of activity between the myocardium and the ventricles, the total volume of the left and right ventricles, and left and right atria, was calculated from the XCAT phantom log file.

$$\begin{aligned} V_H &= V_{lv} + V_{rv} + V_{la} + V_{ra} \\ &= 135.990692 + 102.162361 + 34.580231 + 50.077438 \\ &= 322.810722\ mL \\ &= 0.322810722\ L \end{aligned}$$

Eq. 9

Where

Symbol	Meaning	Units
V_H	Total volume of the heart chambers	mL
V_{lv}	Volume of the left ventricle at end-diastole	mL
V_{rv}	Volume of the right ventricle at end-diastole	mL
V_{la}	Volume of the left atrium at end-diastole	mL
V_{ra}	Volume of the right atrium at end-diastole	mL

This was used to calculate the percentage of the total body blood volume that is in the heart at end-diastole (Eq. 10). The total body blood volume for an average male is 5.5 L [85].

$$P_{TBV} = \frac{V_H}{V_{TB}} \times 100$$
$$= \frac{0.322810722\ L}{5.5\ L} \times 100$$
$$= 5.86928585\%$$

Eq. 10

Where

Symbol	Meaning	Units
P_{TBV}	Percentage of the total body blood volume within the heart chambers	%
V_{TB}	Total body blood volume	MBq

According to the ICRP report 128, the amount of activity within the blood after five minutes is less than 5%. To be certain of not underestimating the effect of the ventricle activity on contrast, the total body blood activity level will be taken as 5%. The amount of activity that would be found in the blood within the heart ventricles was calculated to be approximately 0.29% of the total administered activity (Eq. 11), or 1.17 MBq for a total administered activity of 400 MBq (Eq. 12).

$$P_{HA} = P_{BA} \times P_{TBV}$$
$$= 5\% \times 5.869\%$$
$$= 0.293464292\%$$

Eq. 11

$$A_H = A_A \times P_{HA}$$
$$= 400\ MBq \times 0.29\%$$
$$= 1.17\ MBq$$

Eq. 12

Where

Symbol	Meaning	Units
P_{HA}	Percentage of administered activity within the blood in the heart chambers	%
P_{BA}	Percentage of administered activity within the total body blood volume	%
A_H	Activity within the heart chambers	MBq

To represent a total administered activity of 400 MBq, a simulated activity of 5.97 MBq was used (Eq. 13). 4.8 MBq was place within in the myocardium and 1.17 MBq in the blood pool within the heart.

$$\begin{aligned} A_S &= A_M + A_H \\ &= 4.8\ MBq + 1.17\ MBq \\ &= 5.97\ MBq \end{aligned}$$

Eq. 13

Where

Symbol	Meaning	Units
A_S	Total activity simulated	MBq

Layering the different activities within the heart was accomplished within GATE by using the "confine" and "forbid" commands. The heart was imported into the simulation in two layers – the outer layer representing the outermost surface of the myocardium and the inner layer representing the innermost layer of the myocardium, or the surface of the ventricle cavities. The first step was to confine the main source to the shape of the outer heart layer. Then the main source was forbidden from the inner layer heart, meaning no activity was present there. Finally, a second source was introduced that was confined to the shape of the inner heart layer. The first source was found only between the two heart surfaces and the second source was found only within the inner heart surface (Figure 24 and Figure 25).

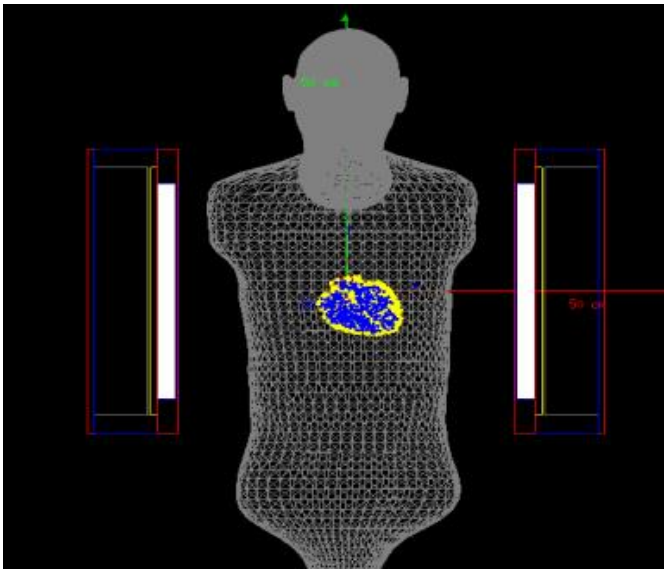

Figure 24: Visualisation of the different layers of source within the heart to create the phase space source file. The main source (yellow) was located in the myocardium. The trace activity in the blood (blue) was located in the ventricles.

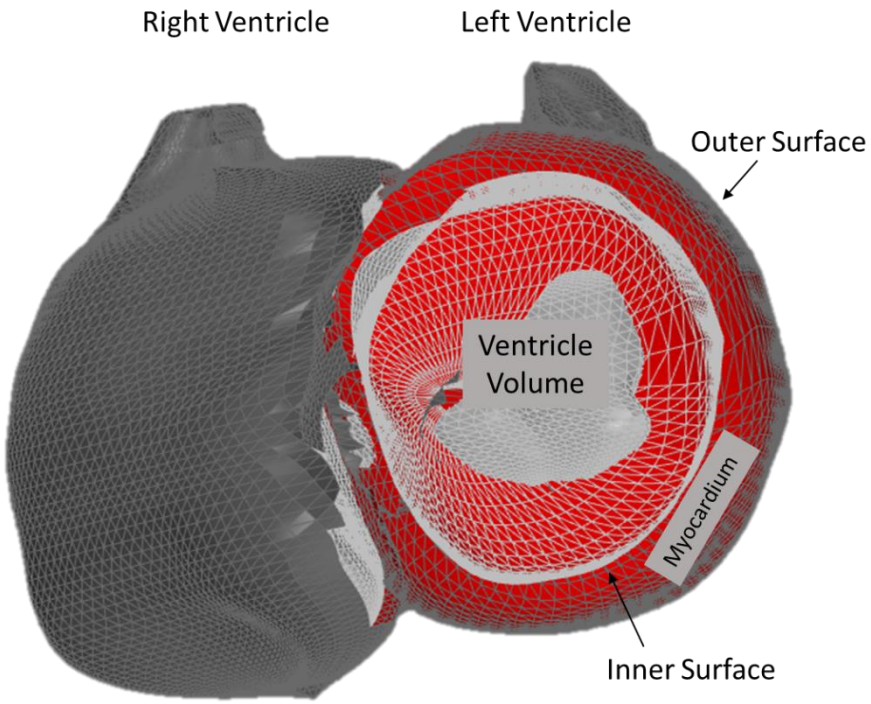

Figure 25: A cross section of the left ventricle, as displayed by the mesh files in Rhino 6. The area between the Outer Surface and Inner Surface was defined as the Myocardium, and was the main area activity was introduced to. The volume within the Inner Surface was defined as the Ventricle Volume. The same definitions were applied to the Right Ventricle.

Phase Space Files

One of the key factors in reducing the time each simulation took was the introduction of phase space files as sources. Phase space files are a way to capture a snapshot of the particle fluence at a particular location in space. This can be used to effectively simplify the source geometry of a simulation, without altering the outcome. To generate a phase space file, a surface was defined and the particles that passed through this surface had their positions and energies saved to the file. The phase space file is then selected as the source for the simulation. The activity of the simulation can be any amount, not limited to the number of photons saved to the phase space file. However, going over the activity level saved in the file can lead to

For this project, an enclosed surface with a basic geometry was defined which encapsulated the source volume. Only photons were recorded. This surface was then used as the source, with the saved photons emitted with the same energy and in the same direction as when they were captured. This resulted in the projection image being the shape of the original source, not of the surface the photons were saved to. The shape of the surface the photons are saved to also impacts the speed of the simulation, with simpler shapes (planes, spheres) completing in less time. The most basic shape relating to the needs of this project is a sphere, but it was decided to use the pericardium surface that was provided with the XCAT phantom files. The pericardium surface was a relatively basic geometry,

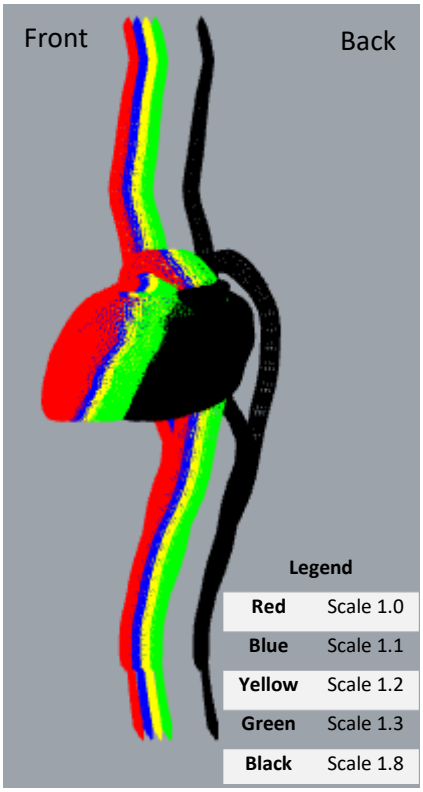

Figure 26: Visualisation of the heart from different scale phantoms, showing the slight movement of organs from one phantom size to the next.

meaning the simulation time was not greatly increased in comparison to the sphere. The sphere would also have overlapped other anatomy, such as the lungs and spine, which reduced the attenuation effects of those organs by decreasing their apparent volume. The pericardium file had the added benefit of having the same origin point as the other organ files, meaning it was automatically positioned correctly, in comparison with the other organs. This was particularly useful as the location of the organs within the body shifted slightly between phantoms of different sizes (Figure 26). A spherical surface would have required manual placement.

To make sure the phase space source and the basic source produced equivalent images, equivalent simulations were run of just the heart and source in a vacuum. The projection angle for this comparison test was 0°. The projection image produced by each simulation were compared visually, as an initial indication the simulation was incorporating the phase space file correctly.

Parallelisation of the Simulation

It is possible to set up a SPECT simulation within GATE where the rotation of the detector head is programmed into the simulation. It was decided, for this project, to not use the feature of GATE and, instead, treat each projection angle as an individual simulation. This way, the different projection angles could be run in parallel as a further way to decrease the time of the total simulation. GATE was not able to run jobs across different cores itself as it is not multi-threaded. It would be possible to manually run each projection as a separate instance of GATE. It was even more efficient to utilise the software GNU Parallel [86] to send different projection simulations to different computer cores within the available servers. The servers are further described below.

By using GNU Parallel, the projection angles and radius of rotation for each phantom size only needed entering in the script once, limiting the possibilities of typos within commands altering the simulation outcome. GNU Parallel was called using the following command line:

parallel ~/MCSims/spectCATv2.0/runSim2.sh --projAngles {1} --index {2} –j37 '>' {2}.log';' rm {1}.log ::: x :::+ y

where: runSim2.sh was the script that opened the simulation in GATE (Appendix A); projAngles refers to the projection angle of a particular simulation; index refers to the time index, with the first projection beginning at time = 0 seconds; the character '>' tells GNU to send the output from the simulations to a temporary log file which was then deleted at the end of the simulation; x represents the angles used for projAngles; and y represents the indices of each projection, with values of 0 – 36, which were used to calculate the activity present at the start of each projection. The actual angles of

the simulation, x, started at 52° and decreased in steps of 2.81° to end at -49.19°, as this matches the settings used at Christchurch Hospital.

GNU Parallel split the simulation into individual projections, which then were run on an individual CPU core. The same version of GNU Parallel was installed on each server.

By adjusting the amount of activity simulated and making use of phase space files, the time for a single projection to be simulated was reduced from around four years to around five days, for the average sized phantom. The parallelisation allowed all 37 projections to be completed simultaneously, rather than having to be done one at a time, which produced another significant decrease in time required to complete the simulations (Table 4).

Table 4: Effect of the time reduction techniques used. The number of projections included in the Full Simulation Run Time column is 37, as each projection collects data from two detector heads, resulting in a full scan.

Simulation Settings	Run Time (days per projection)	Full Simulation Run Time (days)
400 MBq (Rest Test) Basic Source	1500	11,100
5 MBq Basic Source	20	740
5 MBq Phase Space Source	5	185
5 MBq Phase Space Source Running Parallel	5	5

3.2.3 Investigation of Simulation Artefact

Continuing from the single projection validation tests performed in the previous section, a full simulation of all projection angles was completed, using all the time reduction techniques described. The purpose of this test was to confirm the method for data collection and reconstruction before beginning the proof of concept study described in Section 3.3. During the analysis of the output from these simulations, the appearance of a dim band across the projection images produced by the GATE simulation was noted in all reconstruction techniques (Figure 27). This band resulted in an apparent defect in the reconstructed image, which was not expected. A set of simulations were then designed to identify the cause of the problem. In a physical system, the first test would often be of the uniformity of the detector. For the simulation system, this test was already completed in the setup verification stage (see Section 3.1.3). As there had been no adjustment of the detector code since this testing, it was ruled out as a cause of the defect.

All simulations in this diagnostic series used the same projection angle (-136.32°) as this was the angle at which the apparent defect was most visible. Each of the steps involving the heart anatomy used the same phase space file and activity level (6 MBq with a 25 second acquisition time). The first test had a different source setup due to using spheres rather than a heart, and different activity (10 MBq with a 20 second acquisition time).

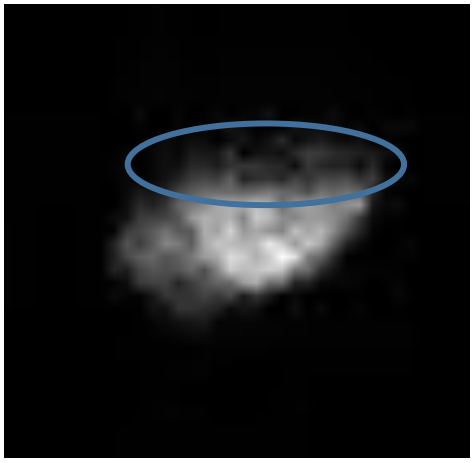

Figure 27: A projection image showing the dim band (indicated in blue) which resulted in an apparent defect in the final reconstruction.

To discover the cause of the reduced counts defect, the tests were designed to find at which point in the simulation process the defect first appears. This was achieved by starting with a very simplistic set up and slowly adding complexity. The most simplistic simulation contained a spherical source only (no anatomy) and the detection system. The source was defined with an area of no activity at its centre (Figure 28).

It was expected that the outcome of this step would be a ring projection with a dimmer circle in the middle, which would confirm that non-uniformity within the detector was not the cause of the defect. This result would also be used as a reference image for later tests.

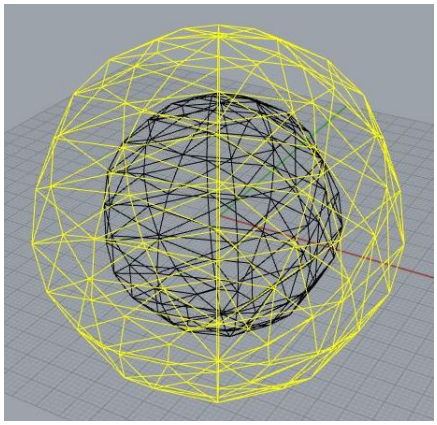

Figure 28: The depiction of a spherical source (yellow) with a second sphere (black) with no activity within it, as produced within the Rhino 6 software. The activity was all placed between the surface of the yellow sphere and the surface of the black sphere.

The next level of complexity was to replace the source with a phase space file, to ensure the defect was not related to the creation of the phase space file. Again, a single projection was acquired, which this time was for the pericardium, with the phase space file for a heart source attached. No other anatomy was present in the simulation at this point, to limit the possible causes if the defect were to appear.

The next test was to place an attenuating medium around the heart. To do this, a large sphere (16 cm radius) was placed around the heart with the material designated as “Water”. The output from this was expected to be the same shape as that from the previous test, with the addition of more scattered photons.

To make sure the problem was not related to the material type, the next step was to change the sphere material from “Water” to “Body”. Once more, it was expected that the output to this test was very similar to the output from the previous tests.

These tests were designed to show if the cause of the defect was not the detector, the phase space file, or the body material. Step five was then to introduce the anatomy as defined in the Body STL file. No other organs were included in this test, other than the pericardium to which the source was attached.

When the defect appeared, and the aspect of the simulation it related to was identified, the full set of projections were simulated once more, with the correction in place. Further explanation of the artefact, and how it was overcome, are described in Section 4.2 and Section 5.2.

While the focus of this section has been on the phantom heart, the processes followed could be followed for any organ of interest. Calculating activity, creating phase space files and testing for anomalies in results are important steps in including any patient geometry into a SPECT simulation.

3.3 Application of the Monte Carlo Simulation with the XCAT Phantom

As the Monte Carlo model of the SPECT system has been validated against the Symbia T2 system, it can be used for any study related to the Symbia T2 gamma camera. One such study is the optimisation of administered activities for MPI scans. While the time frame of this thesis did not allow for a full optimisation study to occur, an investigation was done, as a proof of concept, into the relationship between patient size and image quality. This was done to provide an example of the type of data that can be gathered using this simulation as developed. The aim of this exercise was to show and quantify the expected decrease in image quality in MPI scans as patient habitus increases, and then to explore any limitations on simulation results. The XCAT phantom (Section 2.9) was used to represent the patient where each patient was administered the same amount of activity.

With the goal of this study being to develop a simulation that will produce accurate results that can be used in an optimisation study for Christchurch Hospital, the next stage after validation of the simulation setup was to test the type of scenarios that will be completed in the optimisation part of the greater project. This included showing the simulation gave the expected results relating patient size to image quality for a given administered activity.

3.3.1 Relationship between Patient Size and Image Quality

The developed simulation has been shown to be an accurate model of the Symbia T2 system. However, it is important to show that the simulation image quality, when combined with the digital phantom, is sensitive to changes in patient size. A range of phantom patients of different sizes were created, and the same activity of ^{99m}Tc was simulated to be within each heart. The reference XCAT phantom chosen was designed to represent the average adult male. It is 176 cm tall and weighs 75.6 kg. All the other phantoms used in this study were made by scaling this phantom from 1.0x to 1.8x, in steps of 0.2x. The scaling factors were applied to the chest skin long axis, chest skin short axis, abdomen skin long axis, and abdomen skin short axis. The amount of material attributed to the volume within these surfaces then increases, as the scaling factor only affected the skin outline for that section, the internal organs retained their original size. Each of the five phantoms were the same height (Figure 29) to only observe the effect of the increased chest circumference, due to added fat, of an otherwise average stature person.

To be able to apply results from this project clinically, a relationship must be found between the phantom sizes, so far referred to arbitrarily by their scale factor, and the measurements made of

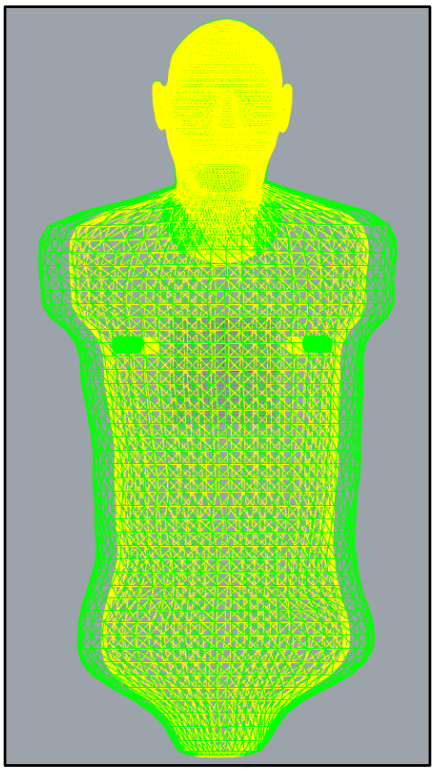

Figure 29: Comparison of MaleScale1.0 (yellow) and MaleScale1.2 (green), showing height remains the same while width dimensions are increased.

patients at Christchurch Hospital. The most direct relationship is the chest circumference. This measurement is not currently recorded at Christchurch Hospital but can be estimated from CT scans for past patients, or implemented for future patients. It is, however, a value directly provided by the XCAT software when it produces the phantom. This makes chest circumference a reliable value, with only error relating to the uncertainty within the software itself likely. Another possibility is to take the values provided by the XCAT software and use them to calculate an estimate of the phantom's weight. The equation developed by Trüb et al. used the chest circumference, the circumference of the midpoint of the upper arm and the height of a person to estimate their weight [87]. Their equation (Eq. 14) was found to have a 90% confidence interval of ±10%.

$$W = -102.53 + 0.50C + 1.81A + 0.44H$$

Eq. 14

Where

Symbol	Meaning	Units
W	Weight	kg
C	Chest circumference	cm
A	Arm circumference	cm
H	Height	cm

Applying this equation to the different size phantoms gives an estimate of their weight (Table 5). These weight estimates can then be used to compare results from the simulation with results found clinically.

Table 5: Estimating the weights of the different scale phantoms, based on chest circumference, height (175.2 cm for all) and upper arm circumference.

Scale	Chest Circumference (cm)	Arm Circumference (cm)	Weight Estimate (kg) (±10% range)
1.0	99.4	33.3	84.5 (76.1 – 93.0)
1.2	118.9	33.6	94.8 (85.3 – 104.3)
1.4	138.4	38.0	112.5 (101.3 – 123.8)
1.6	157.9	44.4	133.9 (120.5 - 147.3)
1.8	177.4	52.1	157.6 (141.8 – 173.4)

As discussed in Section 3.2.2, the total activity simulated in each heart was 5.97 MBq made up of 4.8 MBq in the myocardium and 1.17 MBq within the ventricles. 74 projection angles were collected, two at a time across 37 simulations. The projection angles were calculated in degrees around the patient, with 0° being when the detector was directly above the patient, parallel with the ground. Following the Christchurch Hospital protocol, projection angles began at 52° and continued in steps of -2.81° around to -153.19°. Each simulation represented 25 seconds of real-time, for a total simulated time of 15 minutes 25 seconds. The run time of each simulation varied, depending on the scale of the phantom and how many other tasks the computer was completing. The time of a simulation increased with patient size due to the increased potential for the photons to interact within the body. As the body volume increases, and the potential for interaction increases, the number of calculations completed by the simulation to determine which photons are scattered and/or detected also increases. The radius of rotation was fixed for each patient, and was calculated to be the radius at the widest point of the patient plus 2 cm.

After each simulation completed, the projection data were reconstructed using a range of methods. The first, most simplistic, method was achieved using a combination of MATLAB and Python. The projection images were converted into sinograms (Section 2.2) in Python, and then underwent FBP,

using the inverse Radon function, in MATLAB to produce each reconstructed slice (Appendix B). The filter used for the reconstruction was a Hann filter (Section 2.2.1).

After the FBP reconstructions were completed, the clinical reconstructions were prepared. These reconstructions were done using the Siemens Syngo MI software (version VB21) [88] on a clinical workstation at Christchurch Hospital. The projection images produced by GATE had to be converted to DICOM format [89], to allow them to be reconstructed using Syngo. The conversion to DICOM format was not straightforward due to Siemens requiring the inclusion of information outside of the basic information required for an image to be DICOM compliant. To make sure all the data tags required were included, a sample DICOM file was produced, matching the simulation specifications. The projection images produced by GATE were then saved to the sample header information, replacing the sample images. This conversion was achieved in Python, after it was discovered that an identification tag automatically included by Matlab resulted in Syngo being unable to read the file. Any header details that needed changing between the different simulations, such as the detector radius of rotation, were edited in Python. The Python conversion script is provided in Appendix C. The image quality of these reconstructed images were then evaluated, to find any relationship between image quality and patient size.

The settings for the reconstruction were chosen to match those used clinically at Christchurch Hospital. For each image, three reconstructions were completed – one using filtered back projection (FBP), and two using the iterative reconstruction method Siemens refer to as Flash3D. The two Flash3D methods used differed in the use of attenuation correction. The first of these Flash3D methods applied attenuation correction by utilising CT images of the patient anatomy acquired at the time of the MPI scan; the second method did not apply any attenuation correction. The iterative Flash3D reconstructions were performed with ten iterations and four subsets (Section 2.2.2).

To provide Syngo with the relevant CT data sets to achieve the attenuation correction, the attenuation map setting of XCAT was used (Figure 30). Once more, the settings of image matrix and slice thickness for these images were matched to those used clinically. A sample set of CT images were created, matching the sample DICOM file used above, and the hear information from these were paired up with the XCAT attenuation images so they could be imported as DICOM images. Each CT image is imported as an individual image and placed relative to the others based off its position data, rather than being imported as an image stack in the way the projection images are. It was necessary, then, to ensure each image was saved to the correct header. If the files were saved in the wrong order, or with the same position data as another image, the CT images would be misplaced and the attenuation

correction would be negatively affected. As above, the conversion from XCAT output to DICOM format was completed in Python.

3.3.2 Relationship between Administered Activity and Image Quality

In this series of simulations, the goal was to show how the image quality affects the visibility of lesions within the heart. A lesion of known size and location was included within the heart, creating the potential for a defect to appear within the reconstructed image. The phantom sizes for this set of simulations match those used in the previous set of simulations, to have a direct comparison between

Figure 30: A sample slice of the XCAT attenuation map, which was provided to Syngo as CT data for the attenuation correction reconstruction method.

images with and without the lesion present. The projections from each simulation were reconstructed using the same process as described in Section 3.3.1. These images were used to observe the change in contrast between the lesion (area of no activity) and the myocardium (area of higher activity).

The defect was produced by XCAT and designed to have the same global origin as the rest of the phantom geometry, allowing it to be placed within the heart without the need for manual placement. The defect dimensions (Table 6) were chosen to show the difference in visibility between images with low and high contrast. The dimensions were based on those used in previous myocardial perfusion simulation studies, and selected as they are at the large end of the commonly used range [90], [91].

Table 6: XCAT settings for the heart lesion.

	Large
Theta Centre	0°
Theta Width	130°
X Centre Index	0.5
X Width Index	3.1 cm
Wall Fraction	1.0

3.3.3 ROI Selection and Image Analysis

The measures of image quality chosen to describe the observed change as patient habitus increases are mean signal, signal to noise ratio (SNR) and contrast to noise ratio (CNR). The equation used for SNR (Eq. 15) is a metric commonly used in other simulation MPI studies [92].

$$SNR = \frac{\mu_{myo}}{\sigma_{bkg}}$$

Eq. 15

Where

Symbol	Meaning
μ_{myo}	Mean signal of the myocardium ROI
σ_{bkg}	Standard deviation of background ROI

The equation used for CNR (Eq. 16) was also used as it was defined in other simulation MPI studies [92].

$$CNR = \frac{\mu_1 - \mu_2}{\sqrt{\sigma_1^2 - \sigma_2^2}}$$

Eq. 16

Where

Symbol	Meaning
μ_1	Mean signal of ROI 1
μ_2	Mean signal of ROI 2
σ_1	Standard deviation of ROI 1
σ_2	Standard deviation of ROI 2

The images were processed using the software ImageJ (version 1.53c) [93]. For each phantom scale and reconstruction algorithm, an equivalent slice was selected and three regions of interest (ROIs) were selected that represented the myocardium, left ventricle and a background region. To select the myocardium ROI, the threshold function within ImageJ was used. The "Auto Threshold" option was applied, using the method "Otsu", and the selection created to match the outline of the pixels that had values above this threshold value. The same ROI was used on each scale phantom; permitted by the fact each heart was known to be the same size and in the same location. Any apparent broadening of the myocardium, or shrinking of the left ventricle, was due to the increase in scatter within a larger patient, rather than a change in heart size or shape. The inner surface of the myocardium ROI was used to create the left ventricle ROI, while the background ROI was chosen as an arbitrary region outside, but nearby, the heart.

The background ROI should represent the noise or background signal present throughout the image. Due to the nature of this simulation, however, no realistic background is present. In the interest of decreasing simulation time, a decision was made only to simulate the activity within the heart, rather than that over the whole body. This means there is no background blood pool of signal present in regions outside the heart, as would be normal for a myocardial perfusion image. All signal outside the heart is due to photons scattered after they are emitted from the heart, or due to limitations of the reconstruction algorithms. To get the best estimate at a good background level, three background ROI's were chosen and compared in an SNR calculation (Figure 31). Background One was right next to the boundary of the myocardium ROI. Background Two was two pixels further out laterally than

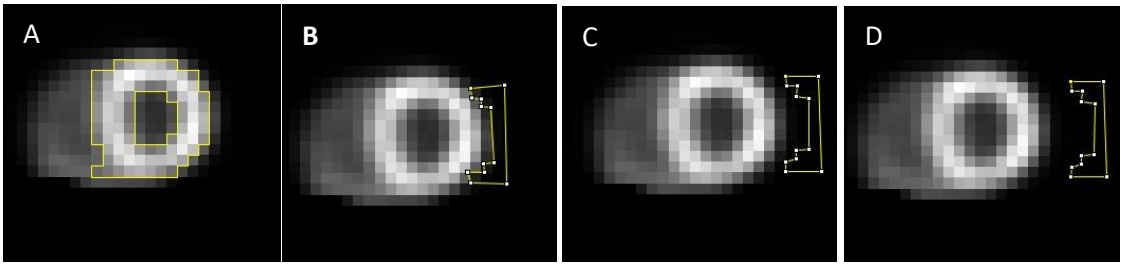

Figure 31: Placement of ROIs for myocardium (A) and background options (B, C, D). Background ROI placement in C was chosen for SNR calculations.

Background One. Background Three was a further two pixels further out from the myocardium ROI. All three background ROI's were the same size and shape. The background ROI chosen was Background Two (Figure 31C). Justification for this choice is given in Section 734.3.3.

For each ROI measurement, the ImageJ function "Histogram" was used, providing the ROI size, mean signal and standard deviation of the signal, along with the minimum and maximum value in the ROI.

Fitting curves to the data was done using Graphical Analysis [94]. The equation and standard error of the line fit was again provided by Graphical Analysis, and the standard error was multiplied by the relevant t-value to report the 95%CI uncertainty of the equations. Uncertainty bars on the graphs for each data point were the standard deviation of the signal per voxel within the ROI.

3.3.4 Qualitative Observation Study

As the images from the simulation may eventually be used to guide clinical practise, it is important to get a measure of how the image quality changed from the physician's perspective. The requirements for this study were that the physicians could not know which image related to which phantom size. They were also not told which images had lesions, nor were they told what reconstruction algorithm was used to produce the images. These requirements were to reduce bias in the image rating.

There were 20 simulated images in the study, each produced using the FLASH3D-AC reconstruction method, to match clinical processing. Of the 20 images, 10 contained a lesion and 10 did not. Each phantom size, representing a range of patient habitus, was represented by a single slice in each of the short axis and vertical long axis views. The images were adjusted in ImageJ to produced images of appropriate orientation that better match how images are regularly viewed in Nuclear Medicine. The only adjustment of noise characteristics was through interpolation for zoomed images, to avoid the pixilated appearance of the reconstructed images. Interpolation was turned on under the Appearance Options, with the Bicubic interpolation method selected under the Image Scale settings within ImageJ (Figure 32). The original images were 64 x 64 pixels, and were interpolated onto 512 x 512 pixels. The adjustments were all completed on a screen checked using the AAPM TG18QA test pattern, and the physicians were requested to view the images on a DICOM Part 14 calibrated display, to get the most accurate reading.

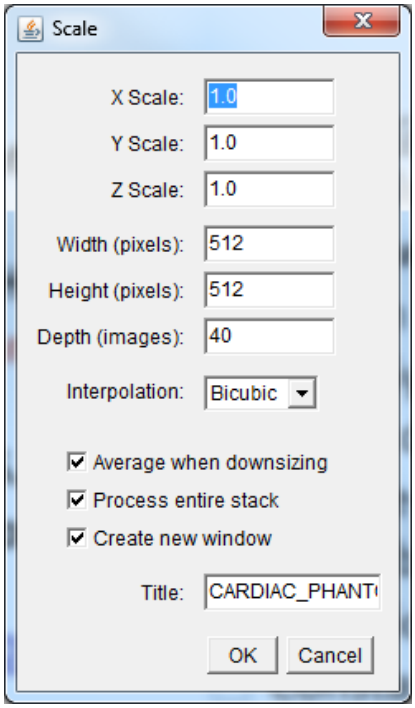

Figure 32: Settings used to create the interpolated images used in the qualitative image comparison. Settings found in ImageJ under Image | Scale.

The images were copied into a word document in a random order, to avoid the results returned by the physicians being influenced by any trend in the image order. The document was saved as a high quality PDF, with the TG18QC test pattern attached to the last page of the document. The test pattern was included to check for any image quality degradation due to the PDF conversion process.

Following similar methods previously used in observation studies [51], the physicians were asked to judge the provided images on a scale from 1 – 5 in two areas: overall image quality and lesion visibility. For each image, the overall image quality was to be given a rating. Then, the presence or absence of a lesion within the image was to be indicated, followed by a rating on the confidence of that indication. The rating scale used is outlined below (Table 7).

Table 7: The five-point scale provided to the physicians, against which each image was judged.

Rating	Image Quality	Lesion Visibility
1	Non-diagnostic	Unfavourable lesion contrast/Very low confidence
2	Acceptable	Low diagnostic confidence
3	Equivalent to routine clinical quality	Equivalent to routine clinical quality/Reasonable confidence
4	Better than average	High confidence
5	Excellent	Sharp lesion depiction/Full confidence

As part of the analysis of the results, the sensitivity and specificity of the observations are measured [95]. Sensitivity (Eq. 17) is a measure of the number of detected lesions (true positives) compared with the total number of lesions (true positives and false negatives). Specificity (Eq. 18) is a measure of the number of lesion-free images (true negatives) compared with the total number of lesion free images (true negatives and false positives).

$$Sensitivity = \frac{true\ positive}{true\ positive + false\ negative}$$

Eq. 17

$$Specificity = \frac{true\ negative}{true\ negative + false\ positive}$$

Eq. 18

An ideal dataset would have a sensitivity and specificity of one, meaning all lesions and lesion free images are identified correctly.

4 Results

4.1 Development of a Monte Carlo simulation

Figure 33 shows the comparison between the projection images of the line source phantom used at Christchurch Hospital, and the simulated line source phantom. To compare the spatial resolution of the two systems (Section 3.1.3), the profile of each projection image was plotted.

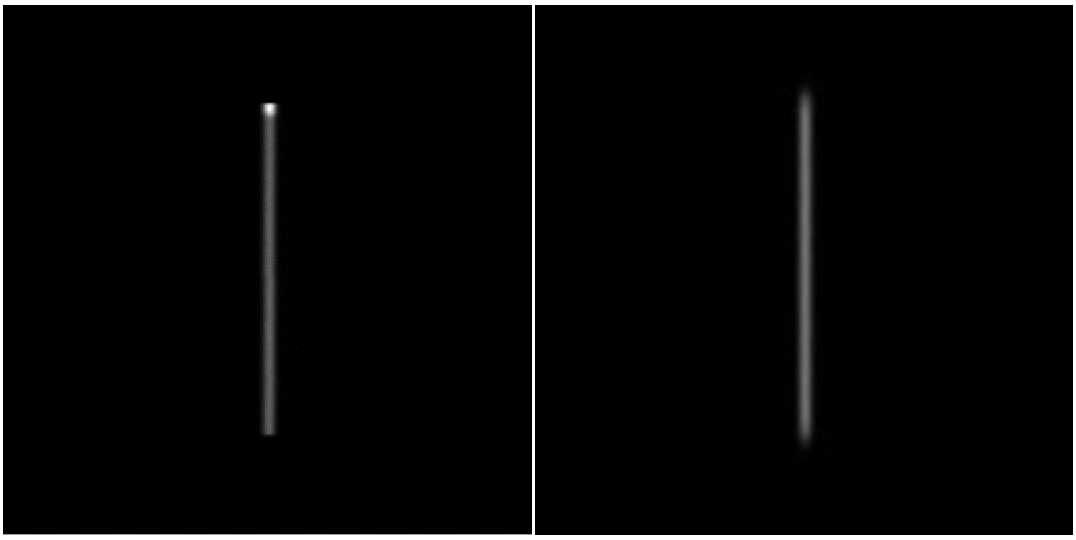

Figure 33: Projection images of the line source phantom, to compare the spatial resolution of the simulated system with the physical system. Left: Projection image from Symbia in Christchurch Hospital. Right: Projection image from the simulation. The 'hot' spot at the top of the left image was accumulated activity in the line source filling port.

These plots were imported into MATLAB where a Gaussian was fitted to the data (Figure 34 and Figure 35), from which the FWHM was calculated (Eq. 19). MATLAB provided the values of *c,* where *c* is equal to $\sigma\sqrt{2}$.

$$FWHM = 2 \times \sqrt{2\ln(2)} \times \frac{c}{\sqrt{2}}$$

Eq. 19

MATLAB also provided the values of c bounding the 95% confidence interval. These were used to calculate the uncertainty in the FWHM. A coverage factor, k, of 1.96 was included so the expanded uncertainty indicated the 95% confidence interval (Eq. 20).

$$c_{lower} + k \cdot u(c) = c_{upper}$$

$$U = k \cdot u(c)$$
$$c_{lower} + U = c_{upper}$$

Eq. 20

Where

Symbol	Meaning
c_{lower}	Value of *c* attributed to the lower bound of the 95% CI
c_{upper}	Value of *c* attributed to the upper bound of the 95% CI
k	Coverage factor
u(c)	Uncertainty in c
U	Expanded uncertainty in c

This was then used to calculate the expanded uncertainty of the FWHM (Eq. 21).

$$U(FWHM) = \frac{d(FWHM)}{dc} \cdot U$$

Eq. 21

Where

Symbol	Meaning
U(FWHM)	Expanded uncertainty in FWHM

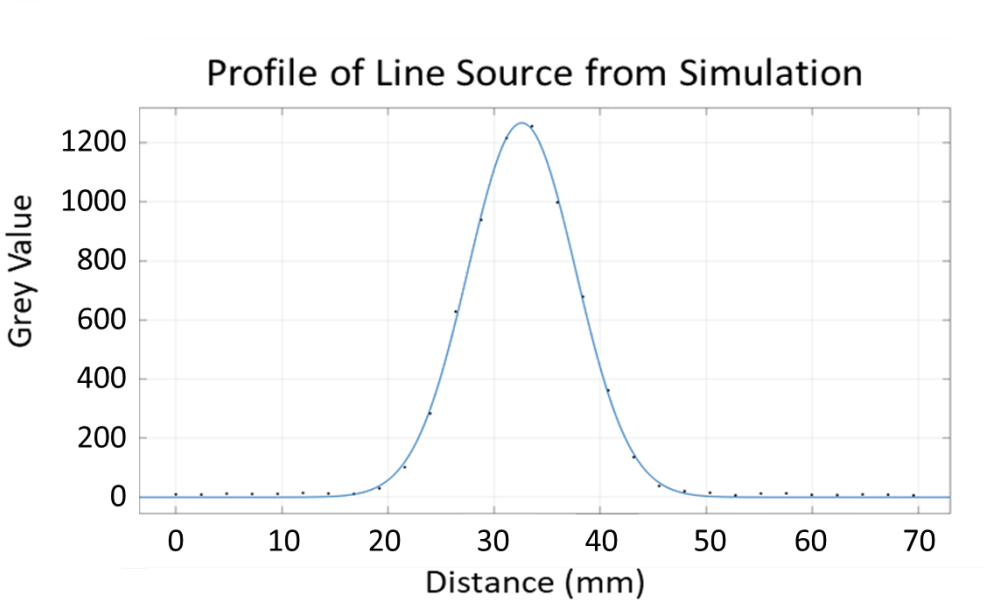

Figure 34: Profile of the line source phantom from the simulation, plotted in MATLAB with a Gaussian fit. R^2=0.999

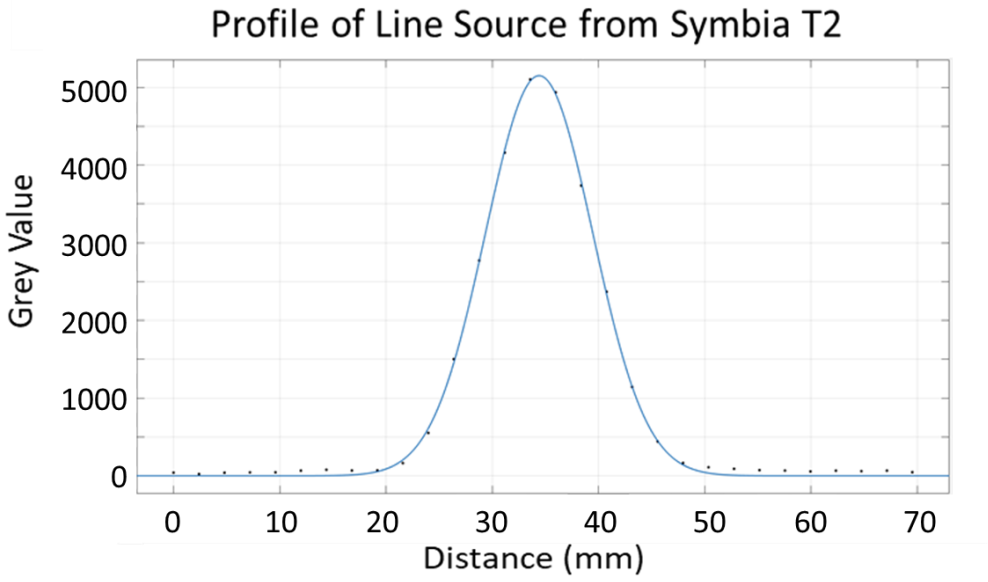

Figure 35: Profile of the line source from Symbia T2 in Christchurch Hospital, plotted in MATLAB with a Gaussian fit. R^2=0.9985

The measured values of *c*, and the resulting calculations of the FWHM for both the simulation and Symbia T2 are presented in Table 8. The overlap in uncertainty ranges for the two values show the simulation is a good representation of the Symbia T2.

Table 8: Measured values of c used to calculate the FWHM and expanded uncertainties relating to the spatial resolution of both the simulation and Symbia T2 system, and the energy resolution of the simulation system.

	c	c_{lower}	c_{upper}	FWHM	Expanded Uncertainty (FWHM)
Simulation (Spatial)	2.995	2.948	3.041	11.96 mm	0.20 mm
Symbia T2 (Spatial)	7.127	7.042	7.211	11.87 mm	0.15 mm
Simulation (Energy)	0.007937	0.007798	0.008075	9.43%	0.17%

The energy resolution of the simulation system was measured in a similar way to the spatial resolution (Section 3.1.3). The energy of each photon interacting in the detector crystal was recorded, and used to make a histogram in MATLAB (Figure 36). The peak values of each bin of the histogram were then plotted and a Gaussian was fitted to the graph. The FWHM of the Gaussian was calculated from the given values, and the given 95% confidence bounds were used to calculate uncertainty.

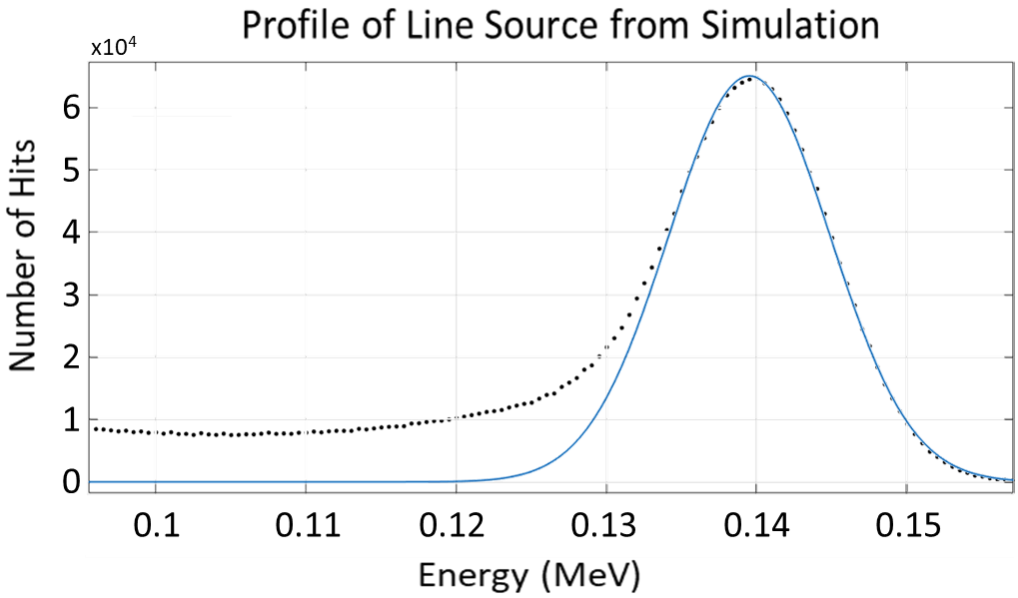

Figure 36: Energy spectrum of the simulation detector system, plotted in MATLAB with a Gaussian fit. R^2=0.9692 for the peak region.

The flood field source (Figure 37), along with its profile plot (Figure 38) shows an even distribution of counts across the detector. While there is slight variation across the image, this is to be expected when working with random processes.

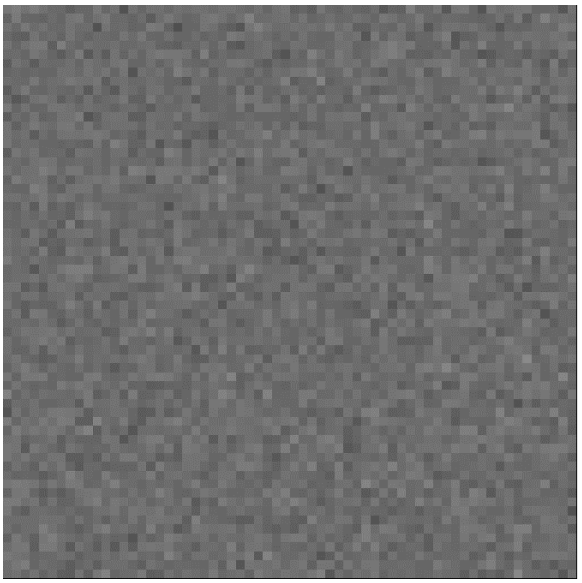

Figure 37: Image from a flood field source showing an even distribution of the source detection

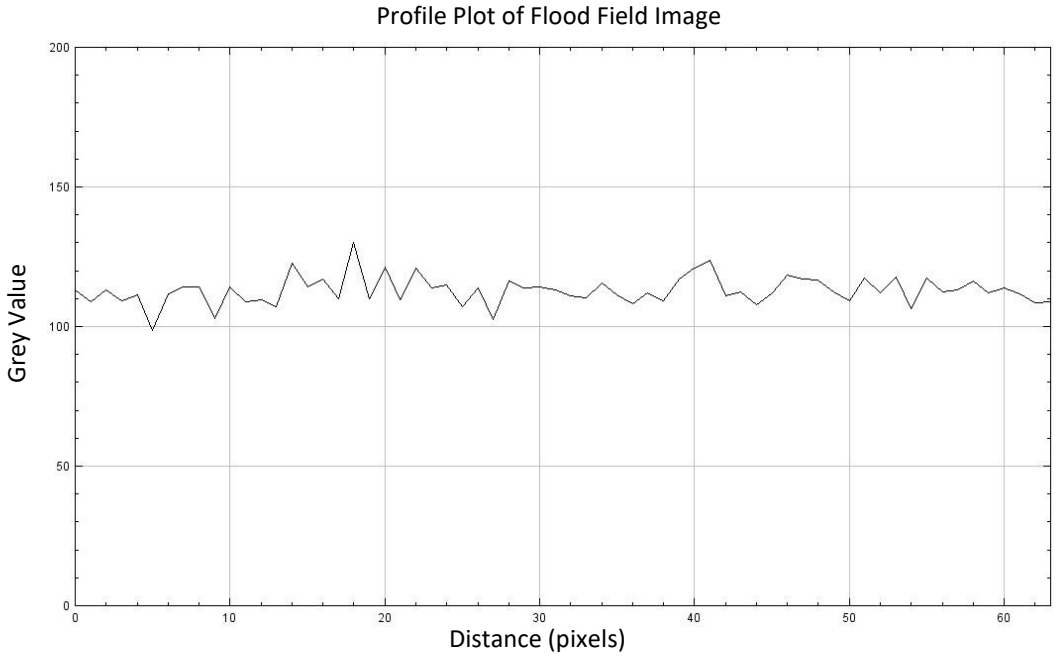

Figure 38: A plot of the cumulated grey values across the flood field image, showing only slight variation in detection count across the image.

The output for the simulation of a line source from each of the three servers were compared to make sure each system gave the same results. The three sets of simulation output were opened in ImageJ and compared visually. The images produced by Fornax (Figure 39A), Puppis (Figure 39B) and Curie (Figure 39C) appeared identical to each other. This initial qualitative visual assessment was confirmed quantitatively by subtracting the images from each other. The image produced by Fornax was subtracted from the image produced by Puppis. The resulting image was completely blank, indicating the images were identical. The image produced by Curie was then also subtracted from the image produced by Puppis, and once more the resulting image was blank. These images show that the three servers gave the same result when given the same starting information.

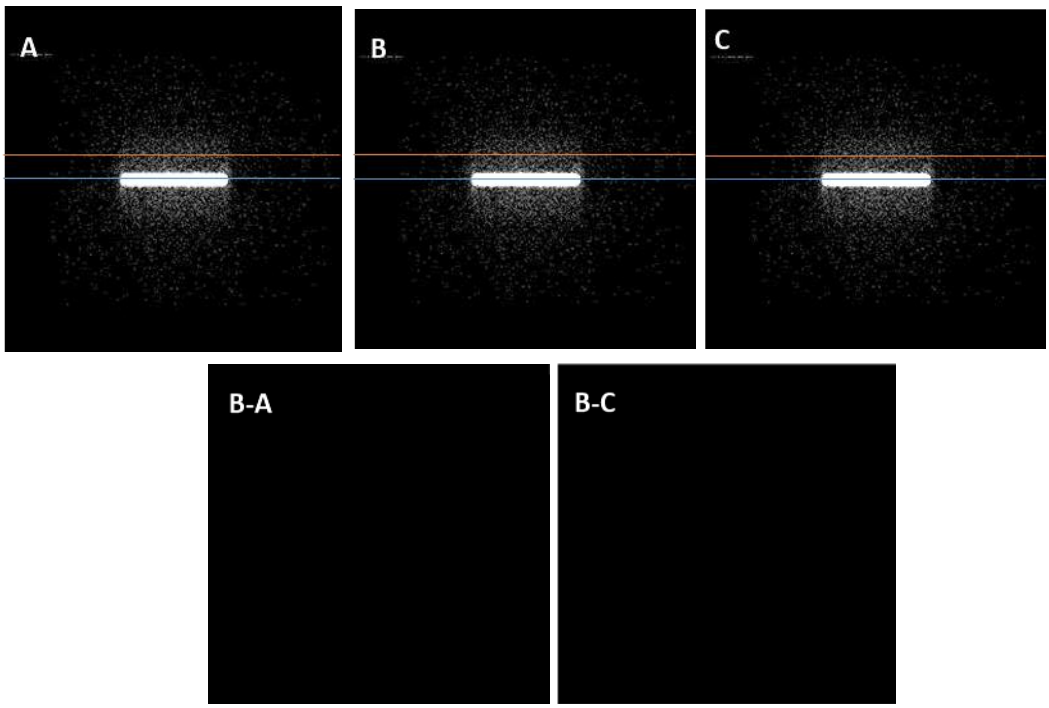

Figure 39: Line source test result from A) FORNAX, B) PUPPIS, and C) Curie. The levels the two profiles were measured are marked in orange (y=110) and blue (y=127). B-A shows the remainder when image A is subtracted from image B. B-C shows the remainder when image C is subtracted from image B.

Further evidence of the identical nature of the images was collected through the analysis of profile plots taken along y=110 and y=127 (Figure 40). One plot (y=127) passes straight through the region of the encapsulated source, to show the same peak values. The other plots (y=110) pass through an area outside the encapsulated source, showing the same placement of individual counts.

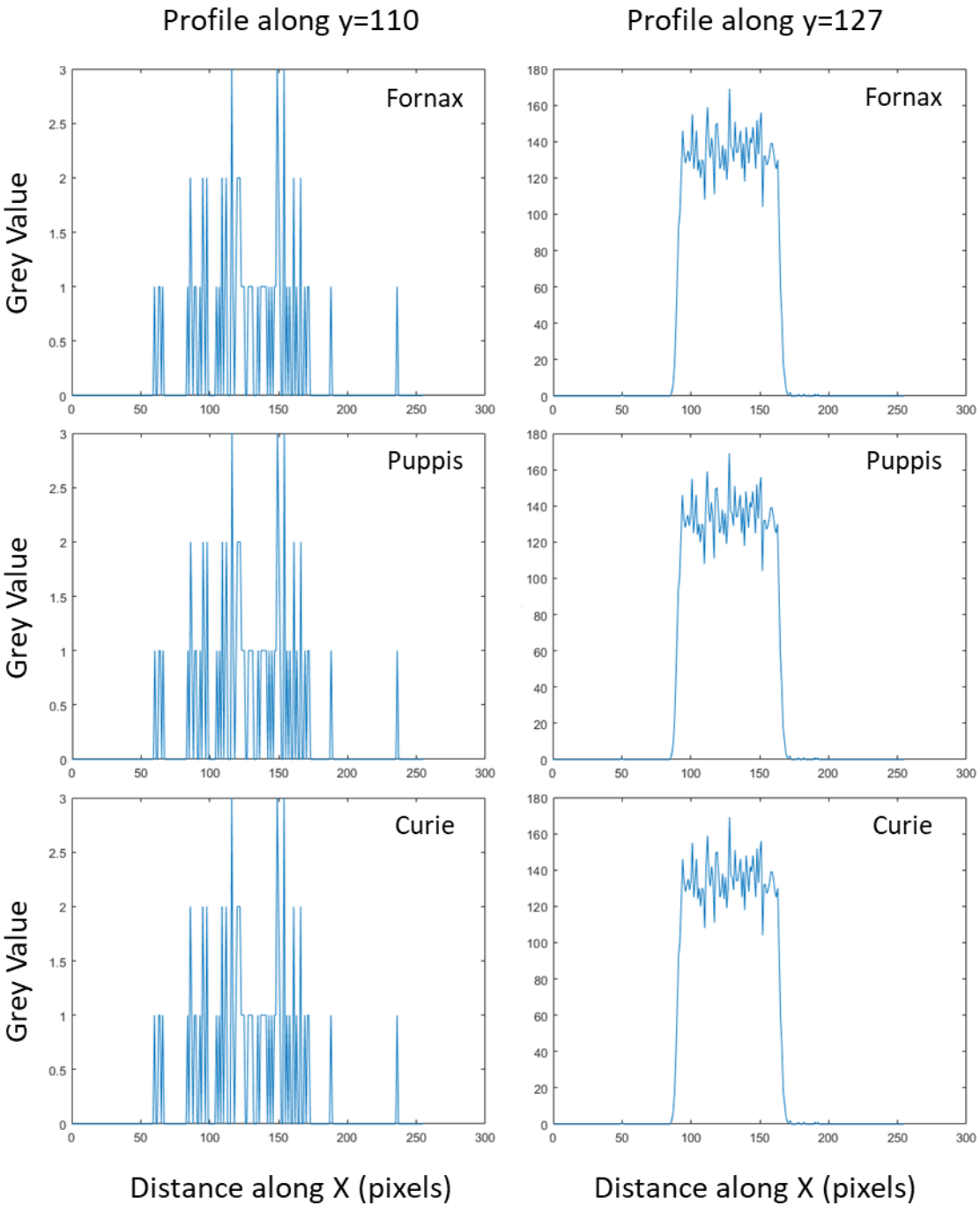

Figure 40: Comparison plots of the profile a y=110 (left) and y=127 (right) for the line source produced by Fornax (top), Puppis (middle) and Curie (bottom).

4.2 Characterisation of a Digital Phantom

To show the phase space file is correctly saving the photons released by the heart source, a projection image at 0° was collected. The expected result in this projection image was for a thick outer ring of counts, with a dimmer region within it to represent the lower activity with the left ventricles. Figure 41 appears to show this, qualitatively, and the quantitative profile plot taken across the centre of the image confirms this result (Figure 42).

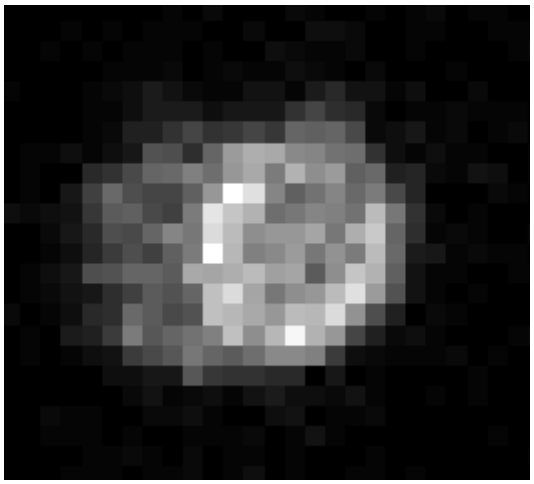

Figure 41: The projection image from angle 0°, using the phase space file, to show the detected image relates to the shape of the original heart source.

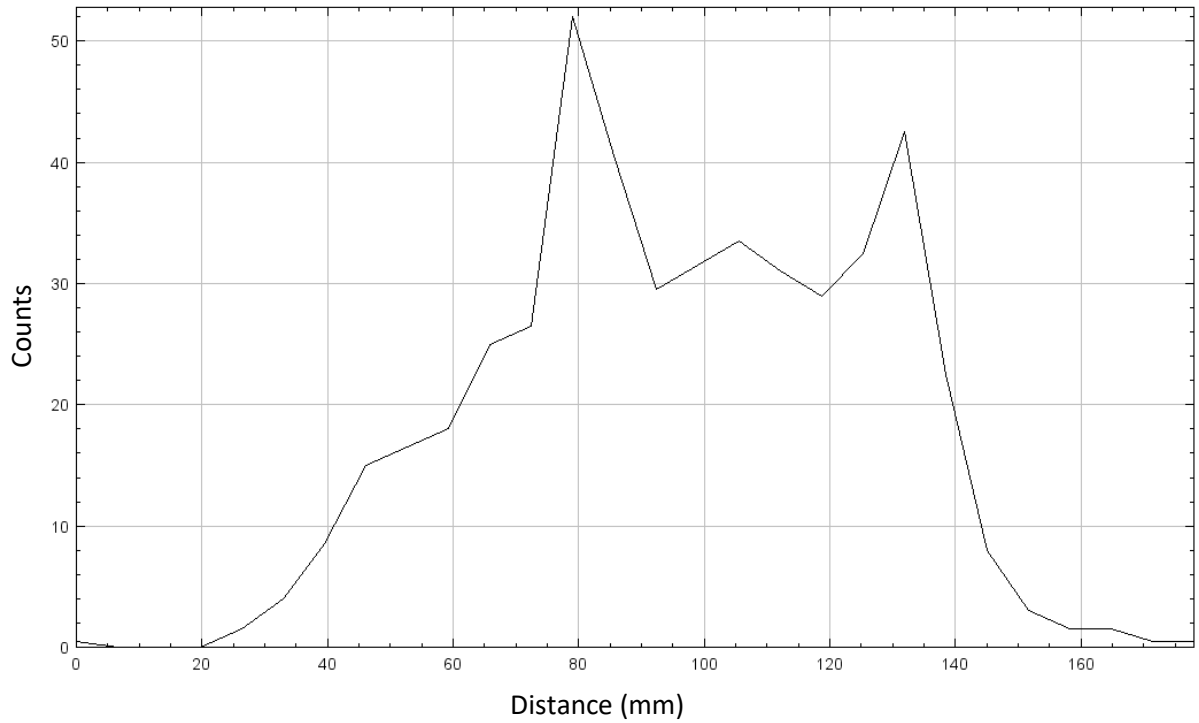

Figure 42: The profile of the projection image at 0°, showing the decrease in counts within the left ventricle, as expected.

While all appeared well at 0°, a full simulation discovered an artefact within the projection images, particularly those around -136°. A series of steps were taken, beginning simple and each introducing a greater level of complexity to the simulation, in order to identify the cause of the artefact. The defect appeared when the Body STL file was introduced to the simulation. This indicated it was related to the Body STL file in some way. Inspecting the image with the defect, and comparing it with the previous tests, it was found that the apparent dim patch was actually the part of the image that matched the number of counts expected. The rest of the heart had more counts than expected, so the defect was actually an increased count defect rather than a decreased count defect.

To try and locate the issue within the body file, the body STL file was modified by the removal of the nipple mesh using the Rhino6 software. The previous test was then repeated using this new body file. The output from this test showed no defect, indicating it relates to the presence of the nipple mesh and how it interacts with GATE.

To confirm the body file was the cause of the defect in the reconstructed image, a full set of projection data were acquired using the nipple free body STL file. A transmission image of each body file was also acquired. Both the reconstructed image and transmission image showed a defect using the original body file, and a defect-free image using the modified, nipple free, body file (Figure 43). The new body file was used for all simulations from this point.

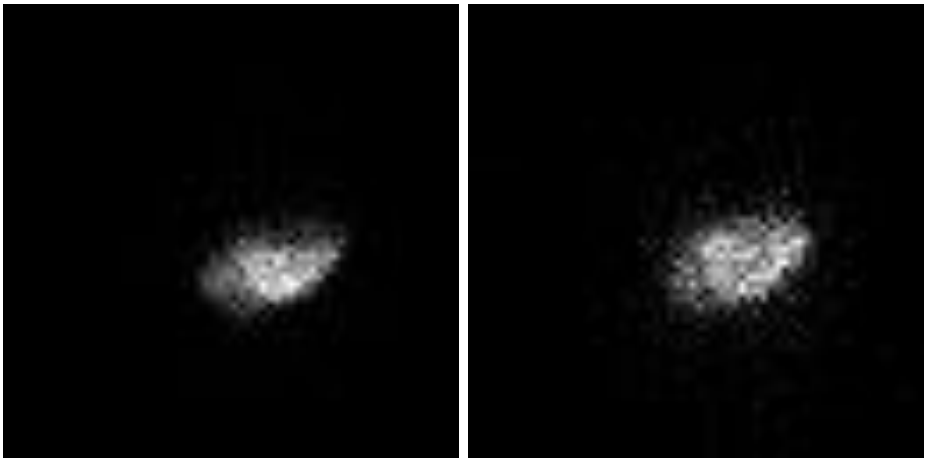

Figure 43: Comparison between body file with original nipple mesh placement (left) and body file without nipple mesh present (right).

4.3 Application of the Monte Carlo Simulation with the XCAT Phantom

Images produced by the simulation as described earlier in this thesis are presented in this section, accompanied by their reconstructed counterparts. Of the 74 projection images for each phantom, every 10th projection is shown (Figure 44 - Figure 48). The reconstructions were completed using four different methods: inverse Radon transformation in MATLAB; filtered back projection (FBP) in Syngo; iterative reconstruction in Syngo with attenuation correction (Flash3D-AC); and iterative reconstruction in Syngo without attenuation correction (Flash3D-NoAC). The iterative reconstruction method, both with and without attenuation correction, was the Flash3D method commonly used at Christchurch Hospital. These reconstructions are represented by four equivalent slices along the vertical long axis.

4.3.1 GATE Output

Assessed visually, the images produced by GATE (Figure 44 - Figure 48) show a decrease in signal as patient diameter increases. The visual observation of this decrease was confirmed by the measurement of mean signal per pixel from a selected angle from each stack of projection images (Figure 49). As explained in Section 3.3.3, the uncertainty bars represent the standard deviation of the number of counts per pixel within the ROI. Projection 51, relating to projection angle -88.54°, was chosen for this comparison.

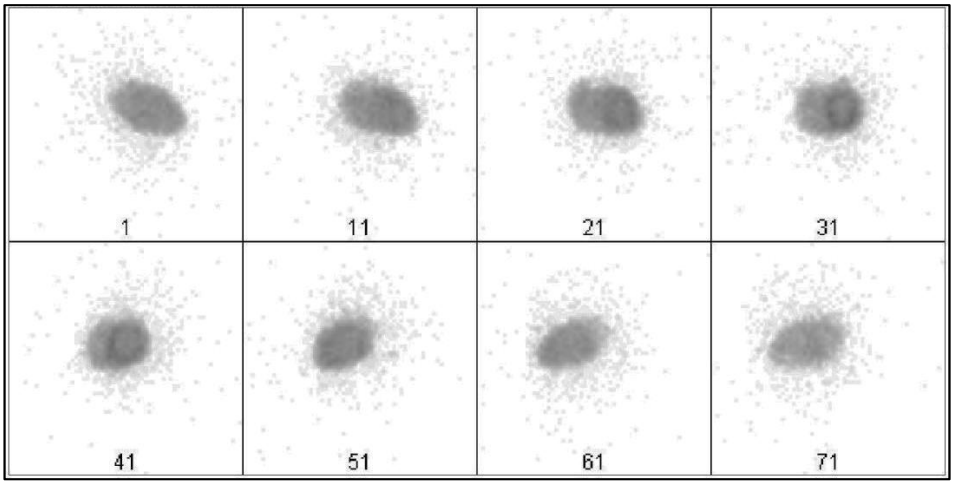

Figure 44: Montage of simulation output of projection images for PhantomScale1.0.

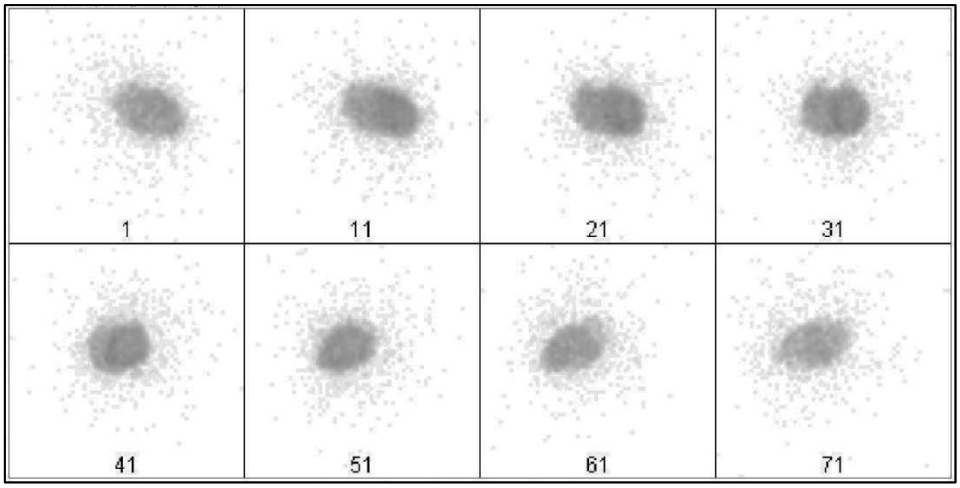

Figure 45: Montage of simulation output of projection images for PhantomScale1.2

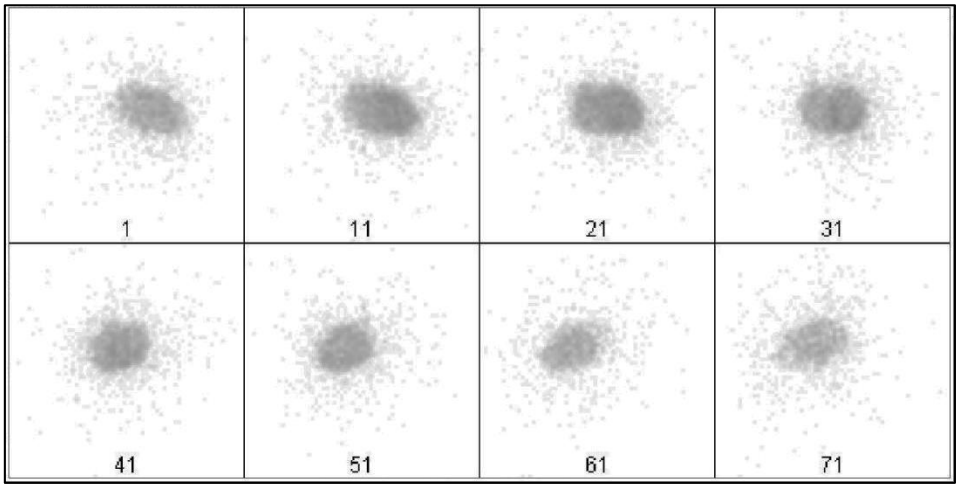

Figure 46: Montage of simulation output of projection images for PhantomScale1.4

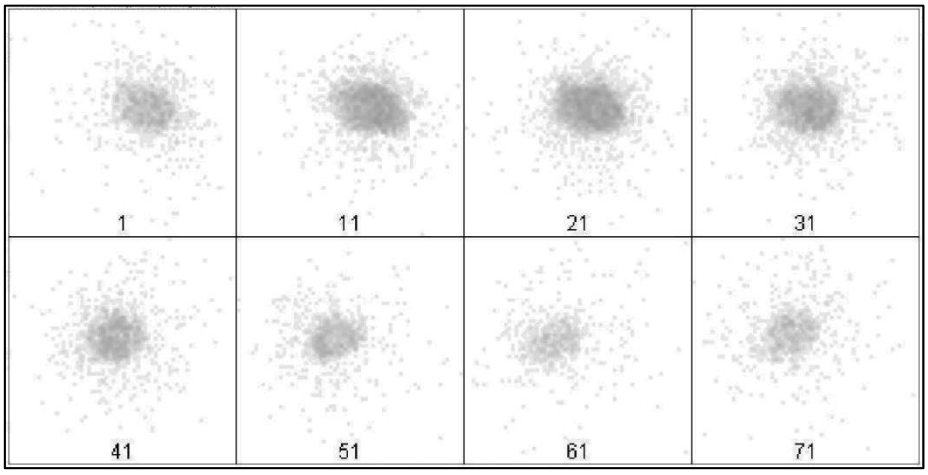

Figure 47: Montage of simulation output of projection images for PhantomScale1.6

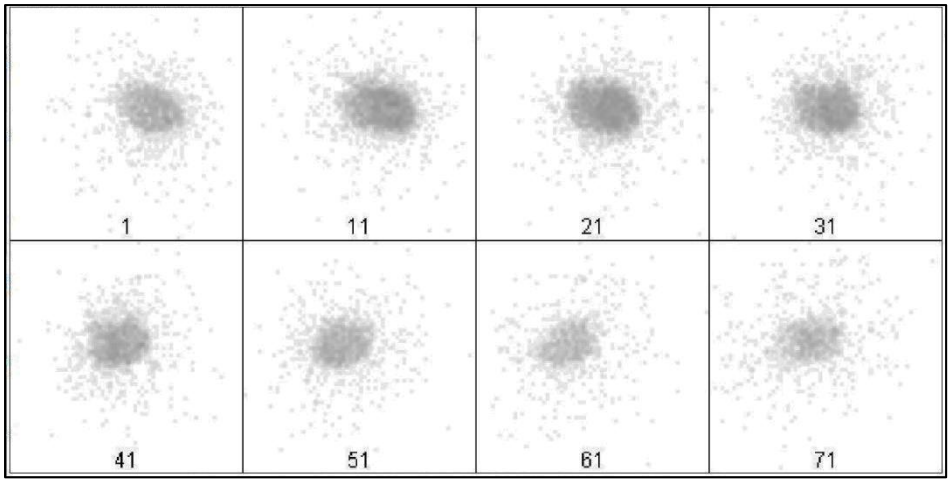

Figure 48: Montage of simulation output of projection images for PhantomScale1.8

Rather than being greatly interested in the trend the decrease in counts in the projection image follows, this measurement was taken as proof that a change did occur. As has been stated, the goal of this proof of concept part of the project is to show that the simulation and phantom together are sensitive to changes in the system, such as the changed patient diameter. The observation of the decrease in mean counts per voxel within the heart region of the projection images shows that the simulation set up is indeed sensitive to such changes. The following sections explore this relationship further, and if there is any dependence on the reconstruction method on the observed trends.

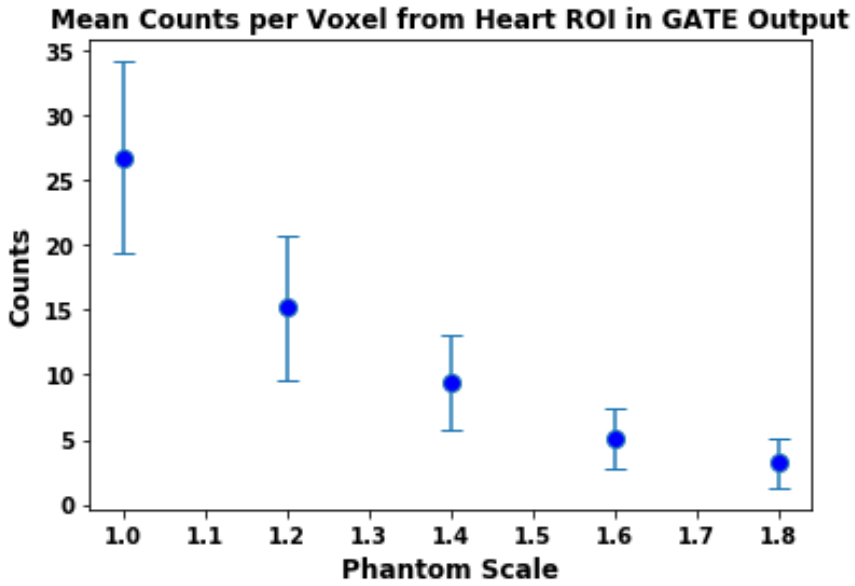

Figure 49: Mean signal per voxel of the heart ROI in projection 51 of the GATE output for each phantom size. Uncertainty bars display ±SD, depicting variability in counts per voxel.

4.3.2 MATLAB Reconstruction

The first reconstruction was achieved using MATLAB. The code for this reconstruction is provided in Appendix B. This was to observe the raw patterns of the data using inverse Radon transformation with a Hann filter. A threshold was applied to the reconstructed image, below which all values were set to zero. The mean and standard deviation of all non-zero values were then calculated and recorded. The plot of the mean number of counts per voxel as phantom size increases (Figure 50) shows a relationship between signal and phantom size of approximately $1/r^3$, where r represents the radius of the patient. This relationship indicates that as the patient gets larger and the volume of tissue the photons must pass through increases, the level of signal reaching the detector drops away proportional to the increase in volume.

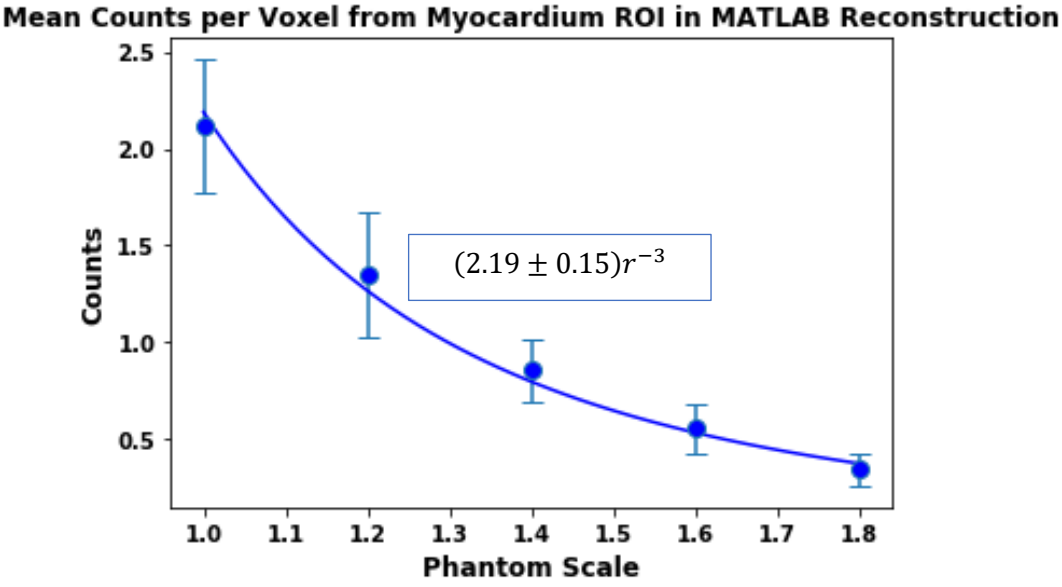

Figure 50: The relationship between the mean number of counts per voxel within the myocardium and the increase in patient diameter follows a 1/r^3 relationship, as reconstructed in MATLAB using a Hann filter. Uncertainty bars display ±SD, depicting variability in counts per voxel.

4.3.3 Syngo Reconstructions

While the MATLAB results give a useful indication of how the simulation is responding to the changing patient parameters, the clinically useful information comes from looking at the reconstructions completed using the Siemens Syngo MI software.

The three reconstructions using each of the three algorithms – FBP, FLASH3D-AC and FLASH3D-NoAC – are depicted below (Figure 51 - Figure 53). The mean and standard deviation of the myocardial signal, ventricle signal and background were measured for an equivalent slice of each reconstruction.

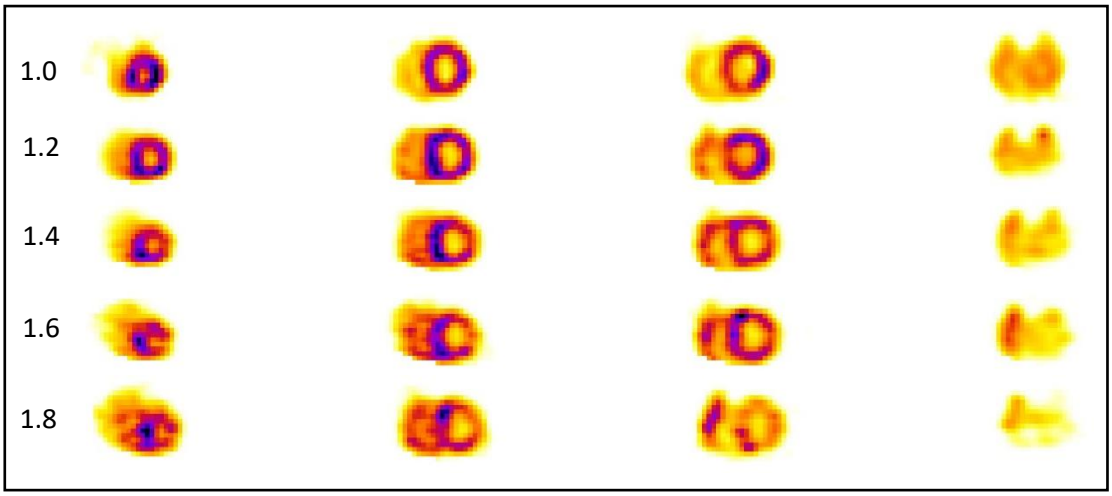

Figure 51: Montage of FLASH3D-AC reconstruction for each phantom size.

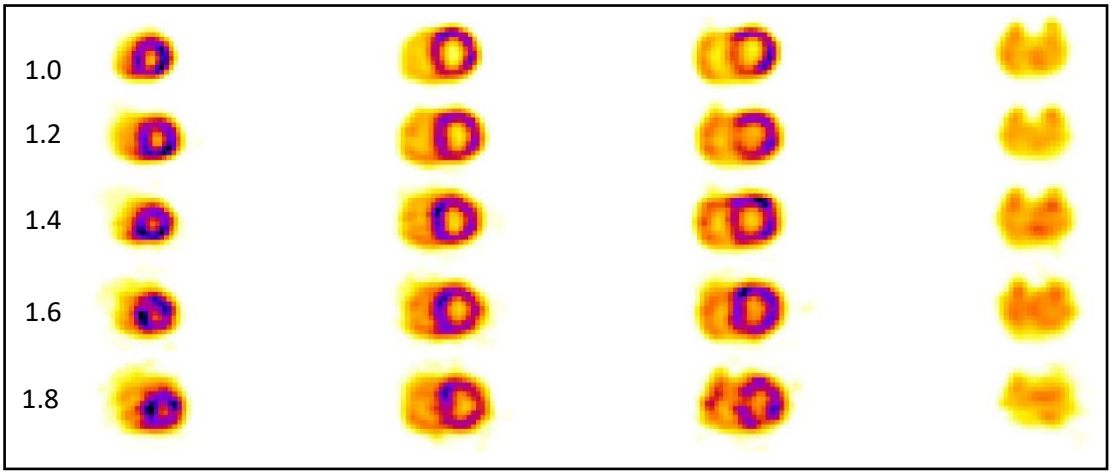

Figure 52: Montage of FLASH3D-NoAC reconstruction for each phantom size.

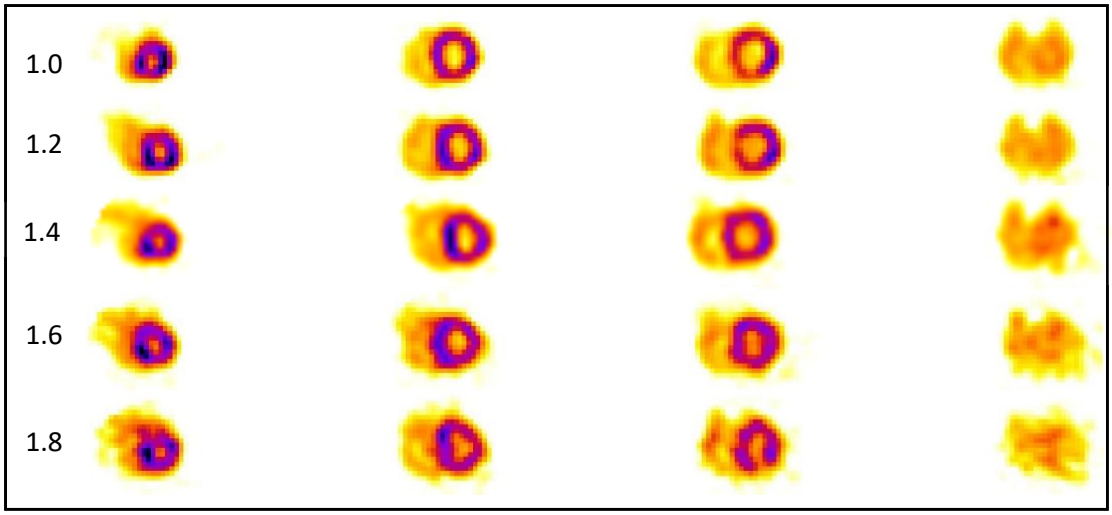

Figure 53: Montage of Syngo FBP reconstruction for each phantom size.

A visual comparison of the reconstructed images shows the three methods produce very similar images. The 1.0 scale phantoms for each method shows a clear ring of signal within the myocardium. As the phantom scale factor increases, the edges of the ring in each slice becomes less sharp, especially for the FBP images. The Flash3D-AC images retain the most contrast between the signal from the myocardium and the signal from within the ventricles. The change in appearance as the phantom scale factor increases is gradual in each reconstruction method, and quantitative analysis is needed to get a true idea of the trends. It is clear, however, that the images relating to the 1.8 scale phantom are of lower quality than the 1.0 scale phantom images.

In terms of quantitative analysis, the three types of reconstruction are compared directly, beginning with the signal. A first look at the reconstructed images showed an unusual spike in counts for the largest two phantoms (Figure 54). A closer look at the reconstruction settings showed the reason for this to be the inclusion of the "Preserve Data Precision" setting in the Siemens reconstruction software. This setting automatically scales the counts observed to better observe the difference between areas of low contrast.

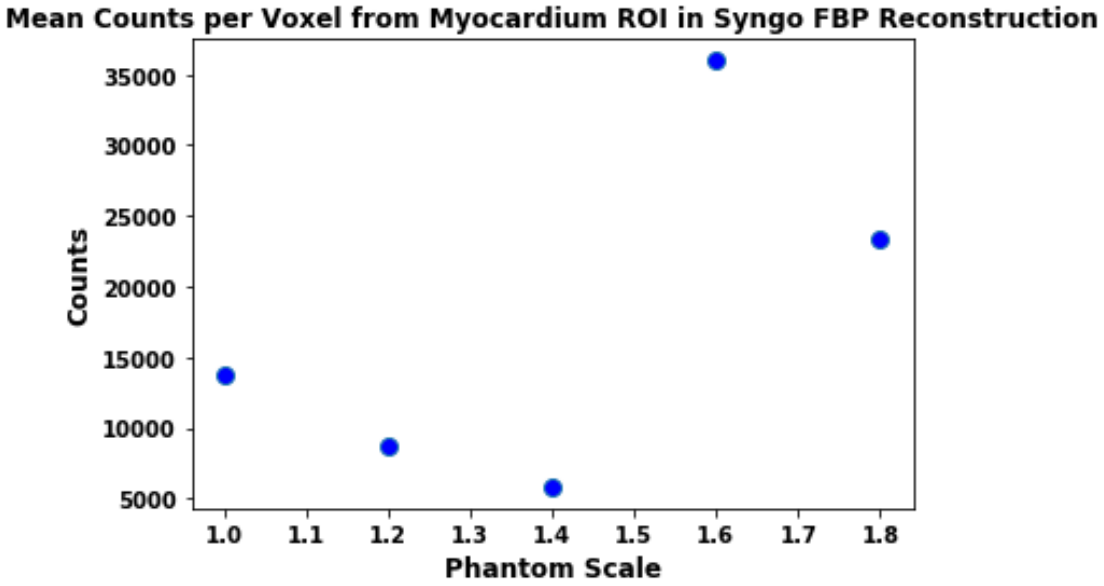

Figure 54: Plot of the mean signal of the heart volume for each phantom using the FBP reconstruction method. The data points for the largest two phantoms are significantly higher than those of the smaller three phantoms. This increase is due to an increased scaling factor used by the "Preserve Data Precision" setting.

The "Preserve Data Precision" scaling factor for each phantom is saved in the DICOM metadata. By disabling the "Preserve Data Precision" setting it was possible to observe the trends outside of this signal boost. The plot of mean signal without the scaling factor applied (Figure 55) shows a non-linear decrease as patient circumference increases. The following observations of signal and contrast trends are done with the Preserve Data Precision scaling factor removed. Any observations of SNR or CNR

are done with Preserve Data Precision in place, as the factor is a constant within the ratio, and therefore does not affect the observed trend.

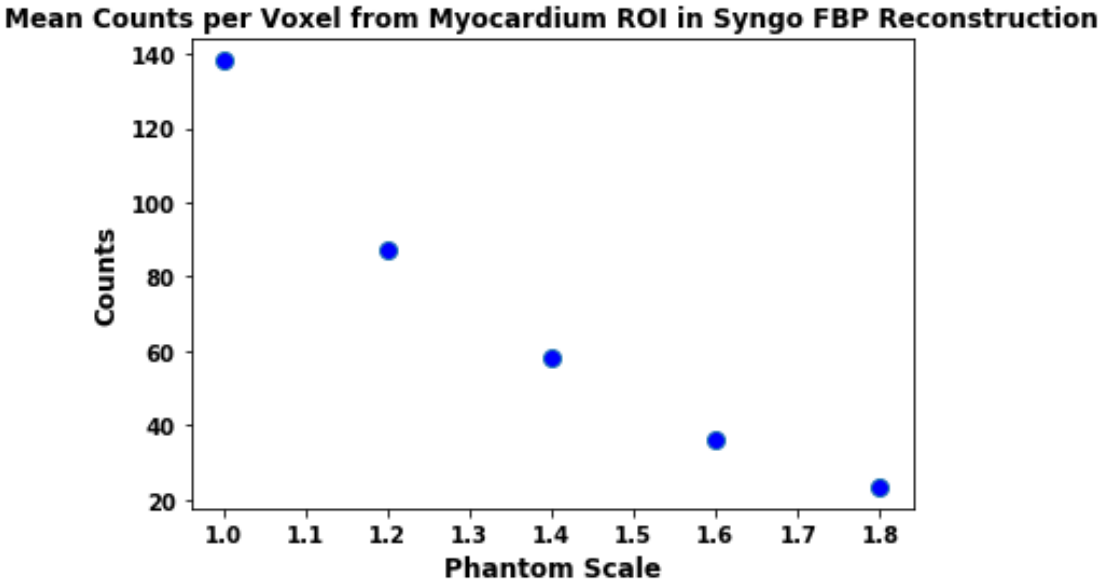

Figure 55: Plot of the mean signal of the heart volume without the scaling factor applied by the "Preserve Data Precision" setting.

Signal

The analyses were completed by viewing slices of the short axis. For both FBP and FLASH3D-NoAC, the decrease in signal as patient chest circumference increases follows an approximate $1/r^3$ trend for r values starting at the phantom scale of 1.0 (Figure 56).

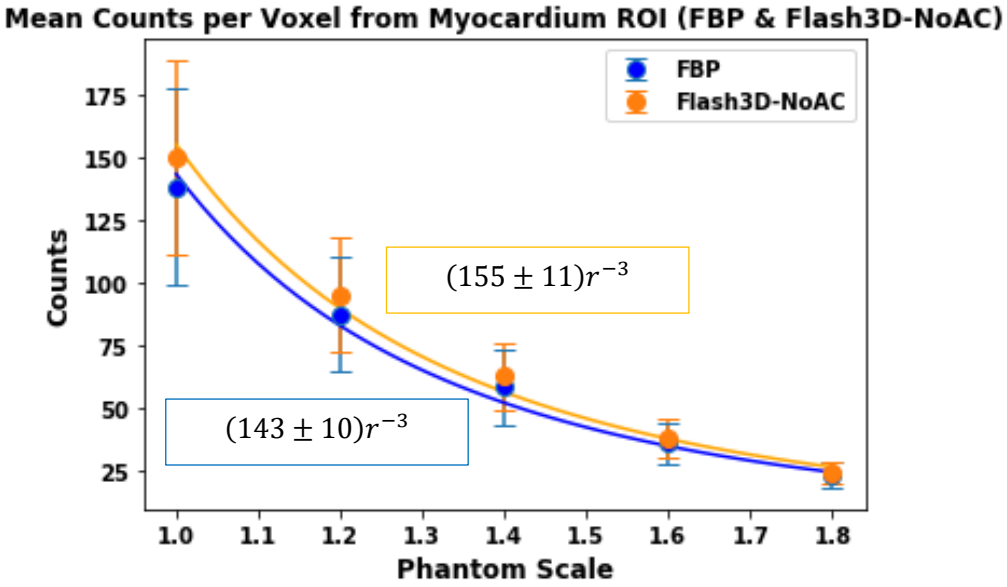

Figure 56: Comparison between mean signal counts from the myocardium using FBP (blue) and FLASH3D-NoAC (orange) reconstructions, showing matching trends.The trend follows a $1/r^3$ curve. Uncertainty bars display ±SD, depicting variability in counts per voxel.

The Flash3D-AC reconstruction follows a different pattern (Figure 57). The plot is not clear, due to the limited number of data points. It could be said that the graph has a curve which peaks at phantom scale 1.2, then follows an exponential decline. Another interpretation could be that the whole range follows exponential decline with the first few data points fluctuating around the trend lines. A further possibility is that the results from the first three patient sizes are fluctuating around a mean value, with the largest two phantoms dropping away from this value

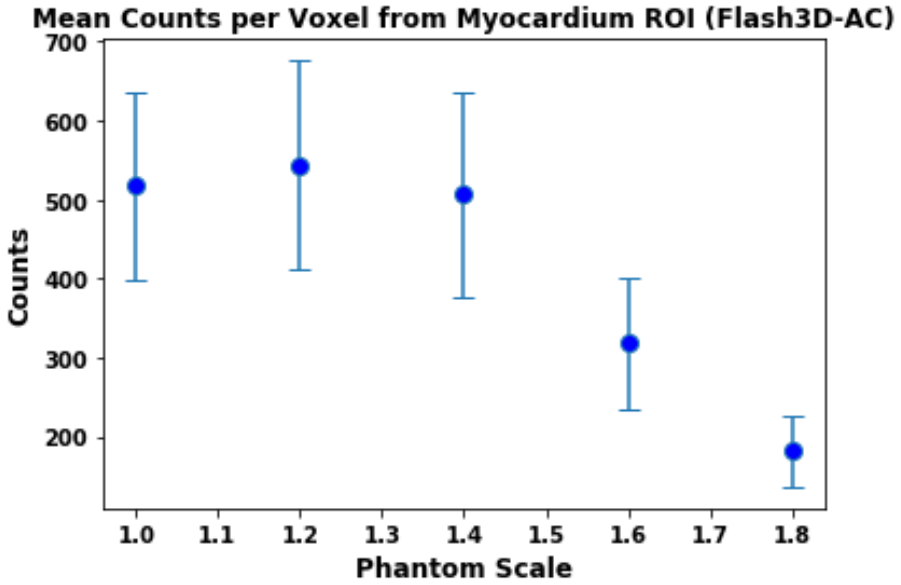

Figure 57: Mean signal counts from the myocardium using FLASH3D-AC reconstructions. The trend for this reconstruction method does not appear to follow the $1/r^3$ trend. Uncertainty bars display ±SD, depicting variability in counts per voxel.

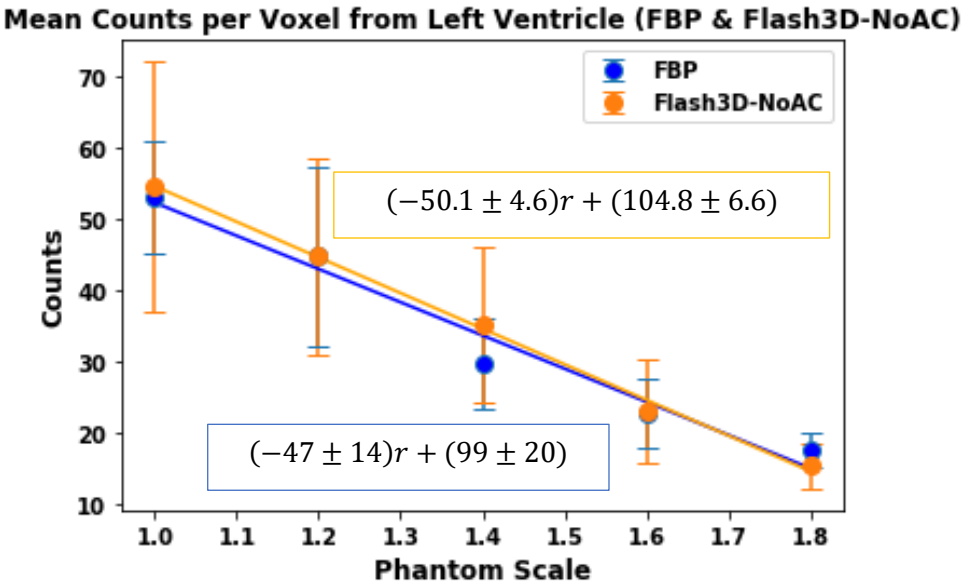

Figure 58: Comparison between mean signal counts from the left ventricle using FBP (blue) and FLASH3D-NoAC (orange) reconstructions, showing matching trends. The trend appears linear. Uncertainty bars display ±SD, depicting variability in counts per voxel.

While the myocardial signal in images using FBP and FLASH3D-NoAC appears to change with $1/r^3$, the signal from within the ventricle appears to follow a more linear decrease with patient size (Figure 58).

The signal from within the ventricle itself is likely to follow the same trend across patient sizes, however the ventricle ROI is likely to include a greater number of scattered photons from the myocardium as patient thickness increases. It is proposed that the competing mechanisms result in an approximately linear decrease in signal overall.

Background ROI Selection

To be able to calculate SNR, an area must be selected which is representative of the background. Three background ROIs were selected, and the SNR calculated using each. The graph of SNR using Background One (Section 3.3.3) showed a rough shape (Figure 59), indicating interference from the myocardium.

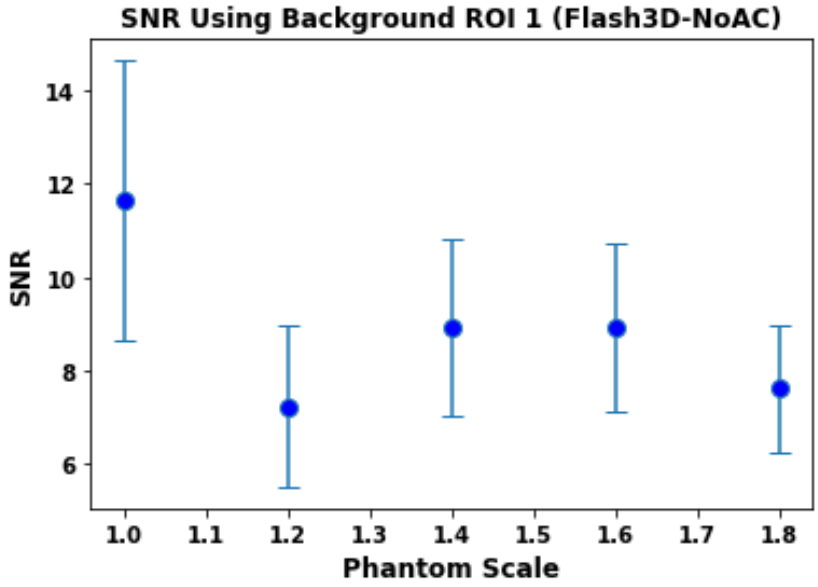

Figure 59: The SNR measured using Background ROI 1. Uncertainty bars display ±SD, depicting variability in counts per voxel.

As the patient increases in size, the level of scatter is expected to increase. As the scatter increases, the region immediately outside the myocardium will increase in signal relative to the myocardium's signal. This poses a problem for the background reading. Background Three (Figure 61) has the opposite problem – a signal that far away from the myocardium must be scattered a great distance before reaching the detector, meaning most photons from that area would no longer have energy within the required window for detection. Therefore Background Two (Figure 60) was used, as it was sufficiently far away from the myocardium ROI to not clip the edge of the heart, but not so far away that the signal drops away to zero.

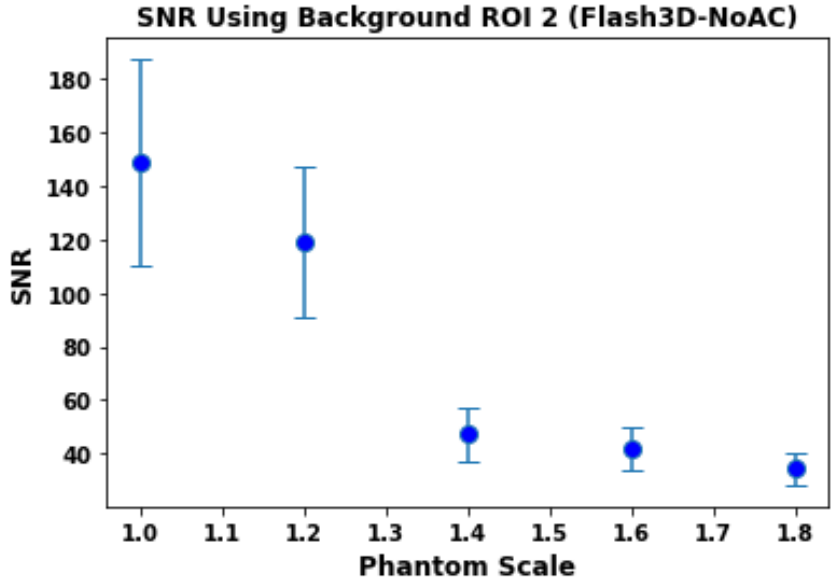

Figure 60: The SNR measured using Background ROI 2. Uncertainty bars display ±SD, depicting variability in counts per voxel.

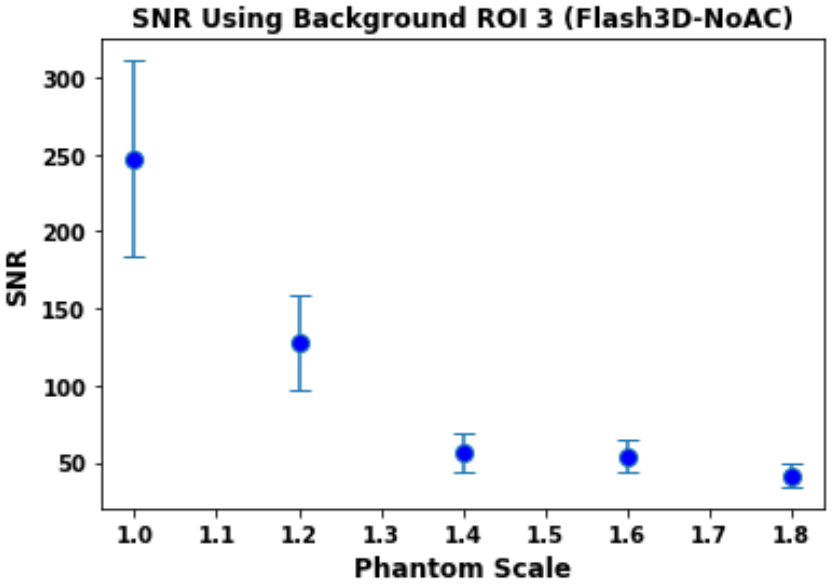

Figure 61: The SNR measured using Background ROI 3. Uncertainty bars display ±SD, depicting variability in counts per voxel.

SNR

In terms of SNR, both FBP and FLASH3D-AC follow similar trends of approximately an exponential decrease as phantom scale increases (Figure 62). FLASH3D-NoAC appears flatter than the other two reconstruction methods, and could be better described with $1/r^3$ than exponential decrease (Figure 63).

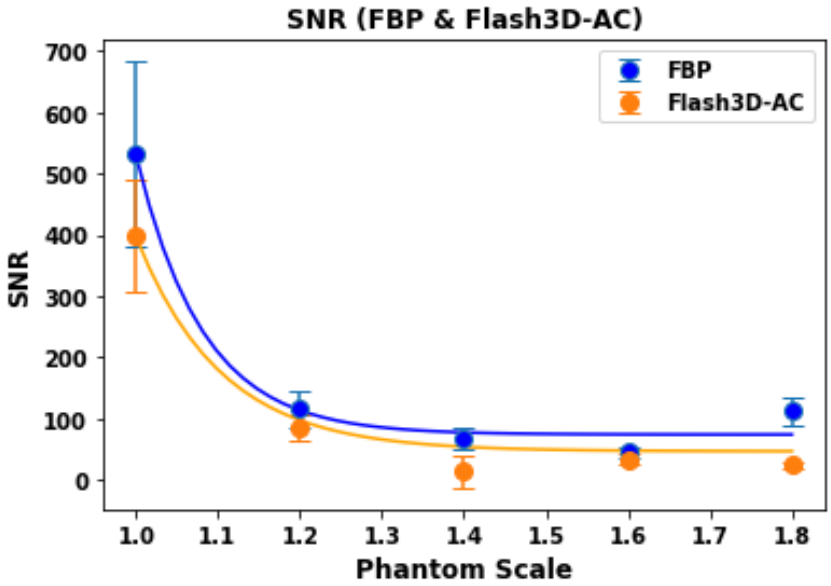

Figure 62: Comparison of SNR for reconstructions using FBP (blue) and Flash3D-AC (orange), both showing an exponential decrease. Uncertainty bars display ±SD, depicting variability in counts per voxel.

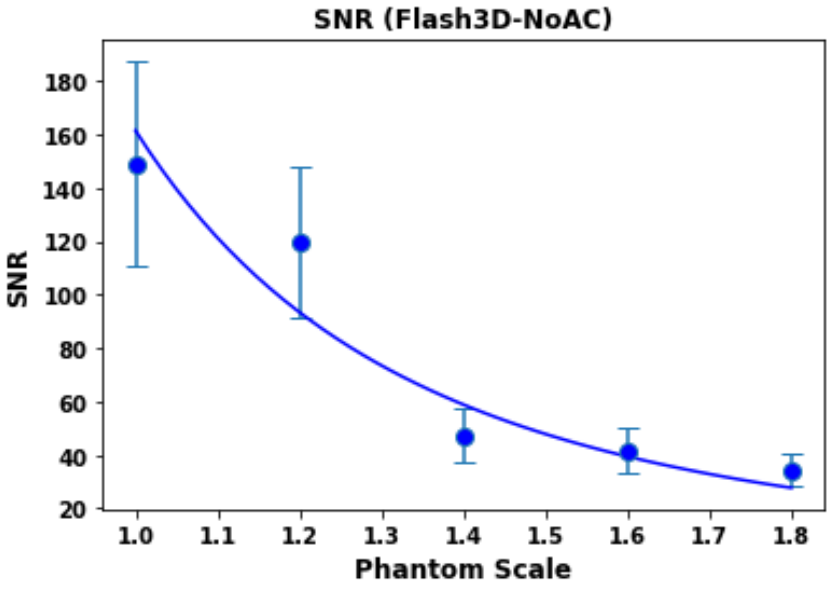

Figure 63: SNR for Flash3D-NoAC reconstructions. Trend line follows $1/r^{3.}$ Uncertainty bars display ±SD, depicting variability in counts per voxel.

The uncertainty bars in both plots is interesting due to the range of sizes. Phantom scale 1.0 for all three reconstruction methods has large uncertainty bars, which then drop away – suddenly for FBP and Flash3D-AC, and more gradually for Flash3D-NoAC. This could be an effect of the very low background values used for this calculation. The 1.0 phantom reconstruction has very few scattered photons making up the background, resulting in a very low background ROI standard deviation. In the calculation of SNR uncertainty, both the uncertainty of the myocardium mean counts per pixel and

the uncertainty of the background mean counts per pixel are taken into account. The very low background ROI uncertainty results in a large uncertainty bar. For the next phantom sizes, however, the number of counts in the background ROI increases, as does the variation of these counts. This increase in background ROI uncertainty, paired with the decrease in counts and variation within the myocardium, results in significantly smaller uncertainty bars for the larger phantom sizes.

CNR

CNR compares the contrast of two areas within an image. The CNR between both myocardium and left ventricle, and myocardium and background for all reconstruction types could be described as flat, especially when taking their standard deviations into consideration (Figure 64).

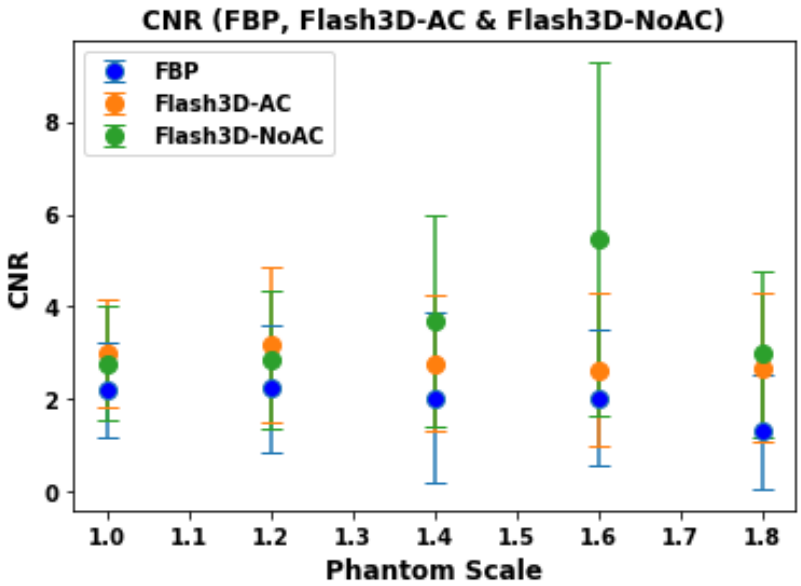

Figure 64: Comparison of CNR between the myocardium and left ventricle using FBP (blue), FLASH3D-NoAC (green) and FLASH3D-AC (orange). All reconstructions appear flat. Uncertainty bars display ±SD, depicting variability in counts per voxel.

In a ratio, such as the CNR equation, for the final value to stay constant the relationship between the numerator and denominator must stay the same. Either, the contrast and difference in standard deviation of the signals must not change in each image, or the denominator term is decreasing at the same relative rate as the contrast. By comparing the contrast between myocardium and ventricle, it is clear that the contrast between the two regions is decreasing as patient diameter increases (Figure 65 and Figure 66). Similar to the change in signal, the trend for FBP and FLASH3D-NoAC appears to follow a $1/r^3$ pattern (Figure 65). The shape of the FLASH3D-AC graph (Figure 66) is not the $1/r^3$ shape of the other two recontruction types, but still decreases as patient habitus increases.

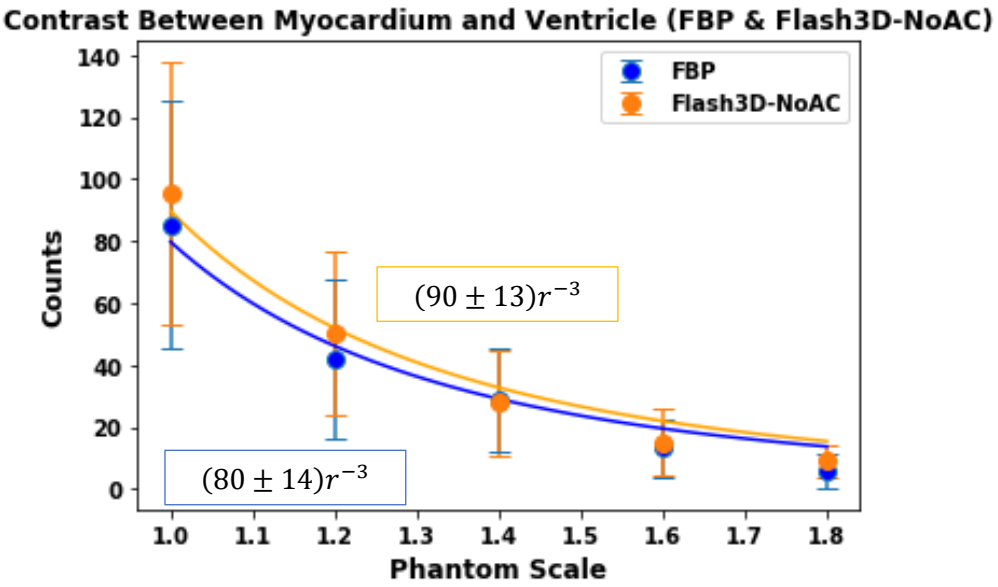

Figure 65: Comparison of contrast between myocardial and left ventricle ROIs using FBP (blue) and FLASH3D-NoAC (orange) reconstructions, showing matching trends. The trend follows a $1/r^3$ curve. Uncertainty bars display ±SD, depicting variability in counts per voxel.

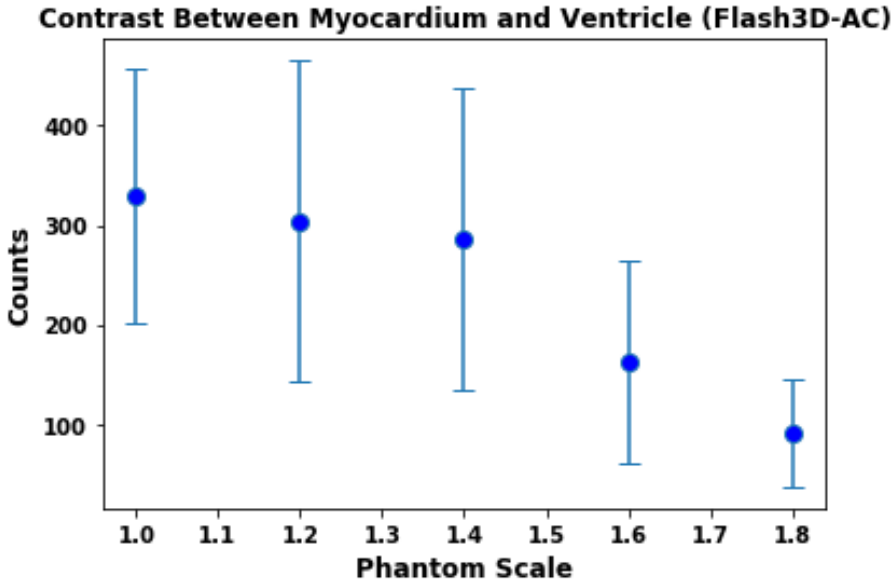

Figure 66: Contrast between myocardial and left ventricle ROIs using FLASH3D-AC reconstruction. Uncertainty bars display ±SD, depicting variability in counts per voxel.

A look at the denominator of the CNR equation shows it is also decreasing. Figure 67 shows both the numerator and denominator for the Syngo FBP reconstruction on the same graph, each normalised to the Phantom Scale 1.0 values. While not identical, each series of points follow the same trend, explaining the flatness of the CNR graphs.

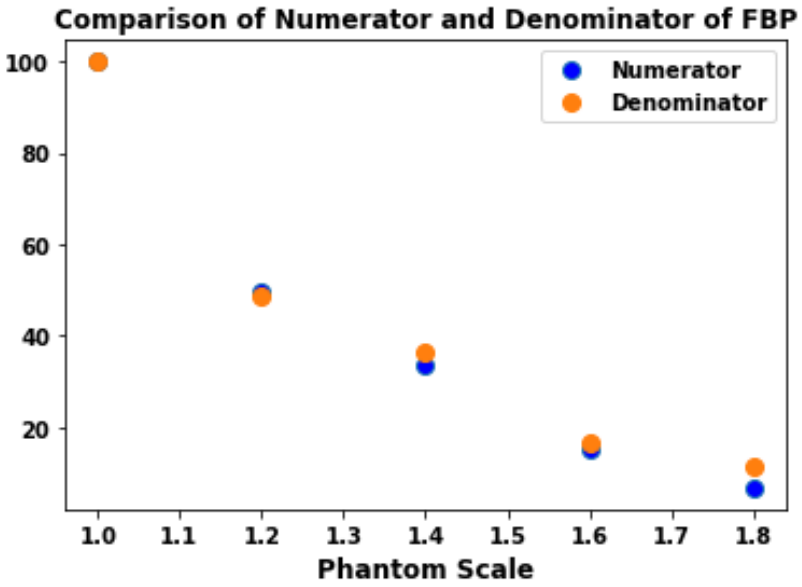

Figure 67: Comparison between the numerator (blue) and denominator (orange) of the CNR equation, each normalised to the 1.0 Scale phantom. Both parts of the ratio following the same trend explains the CNR graph being flat as patient diameter increases.

A comparison was also done between the reconstruction algorithms looking at the vertical long axis. These plots shows similar trends to those observed on the short axis, as expected.

4.3.4 Lesion Appearance

The next relationship the simulation was used to explore was that between lesion visibility and patient size. The same method was used in reconstructing and analysing these images as was used for the lesion-free images (Figure 68 - Figure 70).

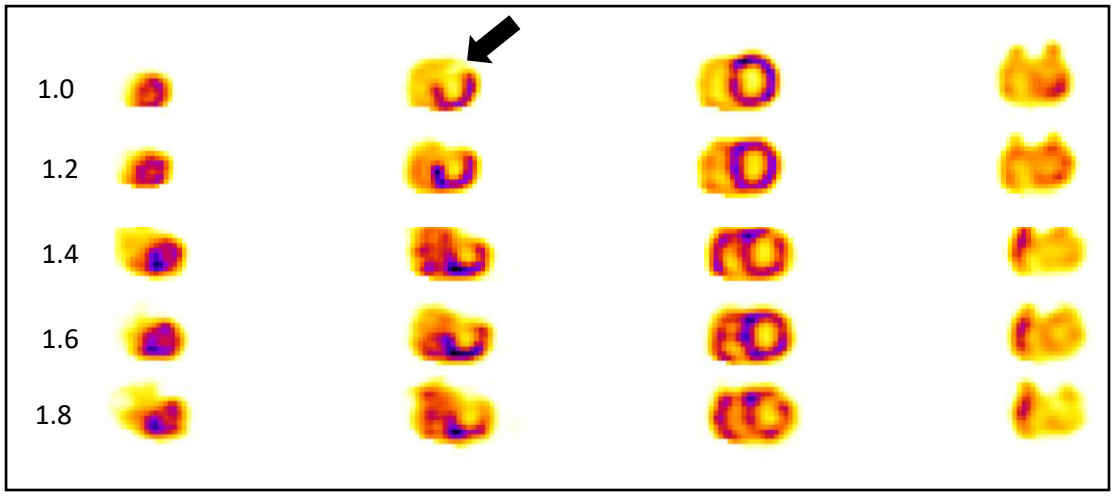

Figure 68: Montage of FLASH3D-AC reconstruction for each phantom size. The black arrow indicates the lesion location for the 1.0 phantom. The lesion is in the same position for each subsequent phantom size. .

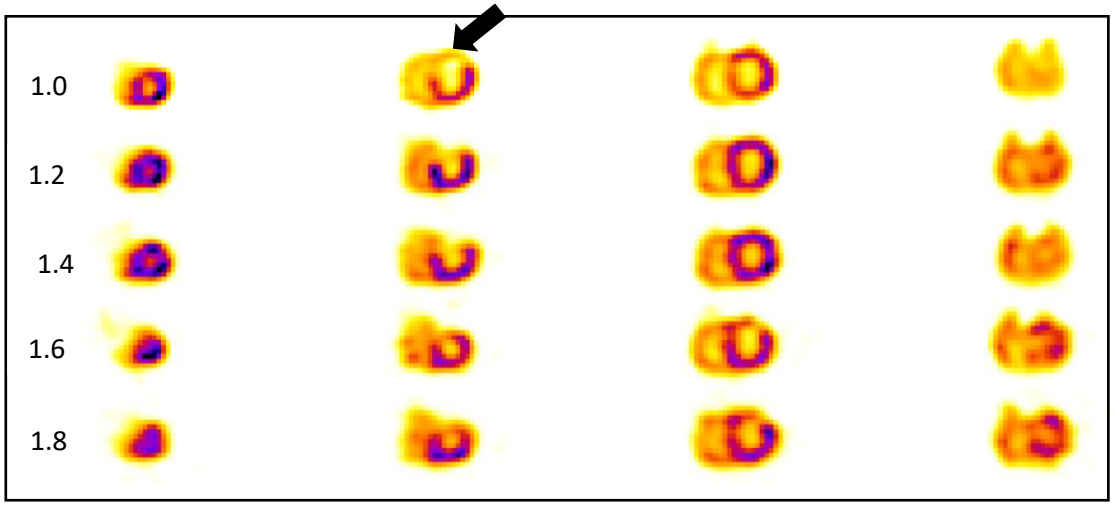

Figure 69: Montage of FLASH3D-NoAC reconstruction for each phantom size. The black arrow indicates the lesion location for the 1.0 phantom. The lesion is in the same position for each subsequent phantom size.

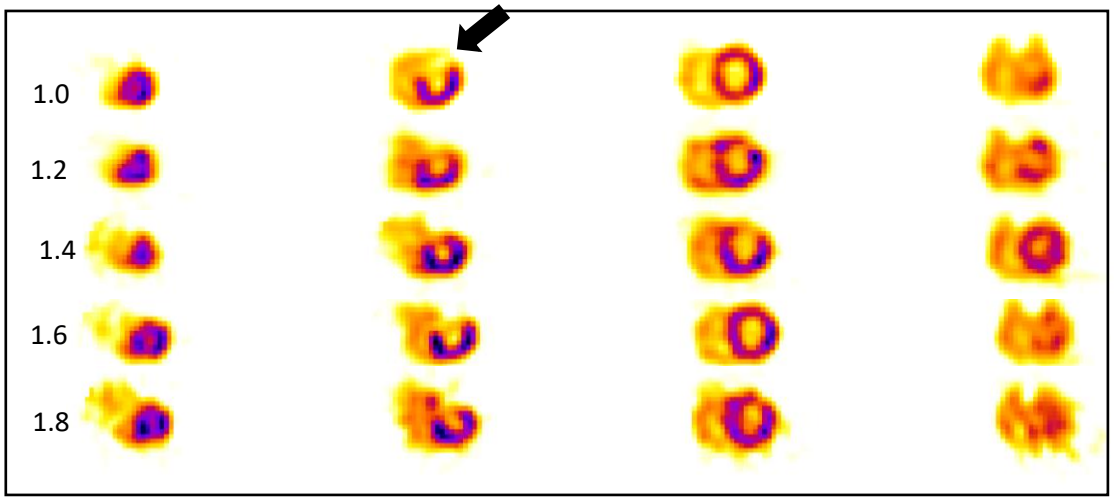

Figure 70: Montage of Syngo FBP reconstruction for each phantom size. The black arrow indicates the lesion location for the 1.0 phantom. The lesion is in the same position for each subsequent phantom size.

The mean and standard deviation of each phantom, for each reconstruction type, was recorded for the myocardium, ventricle, lesion volume and background (Appendix D). These values were used to calculate the SNR of the image overall and the CNR between the myocardium and the lesion.

As confirmation of the consistency of the simulation, the signal and SNR of the two sets of images (lesion-free and lesion present) were compared. As an example of the consistency that was found between the measurements, the comparisons for FLASH3D-NoAC are presented (Figure 71 and Figure 72). The full set of comparison graphs are presented in Appendix E.

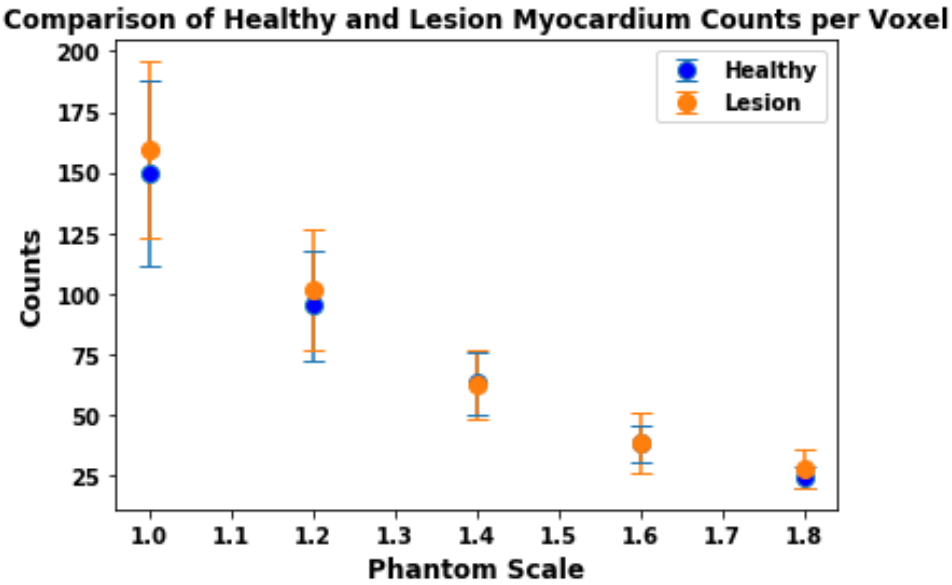

Figure 71: Comparison of mean signal counts from the myocardium between the lesion-free healthy simulation (blue) and the lesion-present simulation (orange). Uncertainty bars display ±SD, depicting variability in counts per voxel.

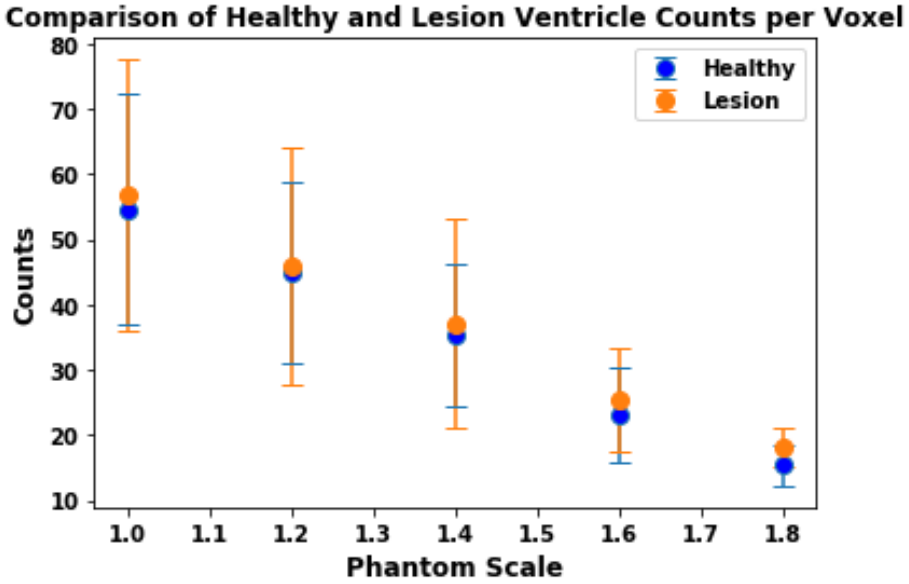

Figure 72: Comparison of mean signal counts from the left ventricle between the lesion-free healthy simulation (blue) and the lesion-present simulation (orange). Uncertainty bars display ±SD, depicting variability in counts per voxel.

The shape of the mean signals of both the myocardium (Figure 71) and left ventricles (Figure 72) align closely. Each point is within the SD of the other. The largest deviation is in the comparison of SNR (Figure 73) where the points for 1.2 and 1.4 vary more than at other phantom sizes. The overall shapes of the curves follow the same trends, however, indicating that the differences in positioning are due to fluctuations around the mean value that is to be expected in Monte Carlo simulations.

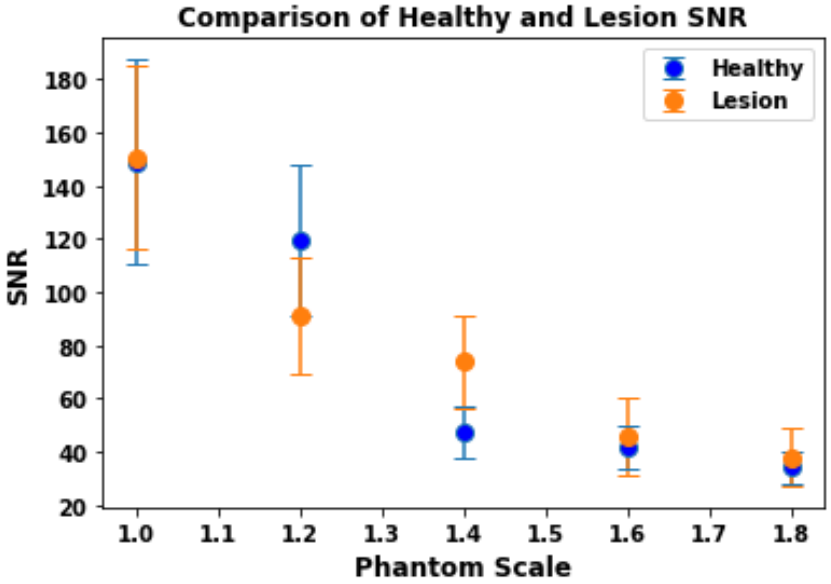

Figure 73: Comparison of SNR between the lesion-free healthy simulation (blue) and the lesion-present simulation (orange). Uncertainty bars display ±SD, depicting variability in counts per voxel.

The next relationship of interest is how the mean counts from within the lesion ROI change as the patient habitus increases. It was expected that an increase in scattering events in a larger patient would increase the number of counts detected within the lesion volume. However, as the number of

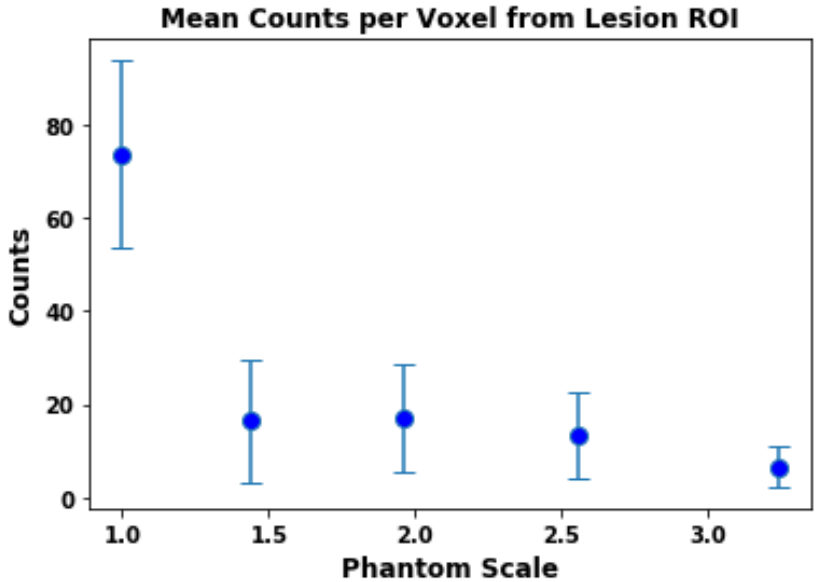

Figure 74: Mean counts from the lesion ROI using FLASH3D-NoAC reconstruction. The trend does not appear to follow the $1/r^3$ curve seen in the change in myocardial counts. Uncertainty bars display ±SD, depicting variability in counts per voxel.

counts detected overall was not constant, the number of counts in the lesion ROI does not follow the expected trend (Figure 74).

To plot the counts within the Lesion ROI as a percentage of the myocardial counts gives a better idea of the relative number of counts. However, this did not give the simple increase that was expected (Figure 75). Rather, it appears there is some other influence on the number of counts.

A similar pattern is observed in both the FBP (Figure 75) and FLASH3D-NoAC (Figure 76) reconstructions, with the FLASH3D-AC reconstruction producing a much flatter plot (Figure 77).

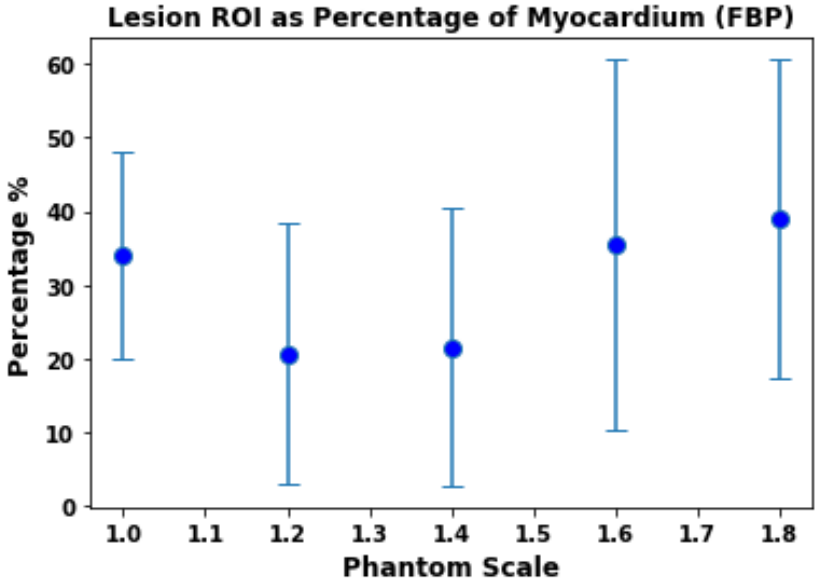

Figure 75: Plot showing the mean number of counts in the lesion ROI as a percentage of the mean number of counts in the rest of the myocardium, using FBP reconstruction. The plot does not appear to follow any particular curve. Uncertainty bars display ±SD, depicting variability in counts per voxel.

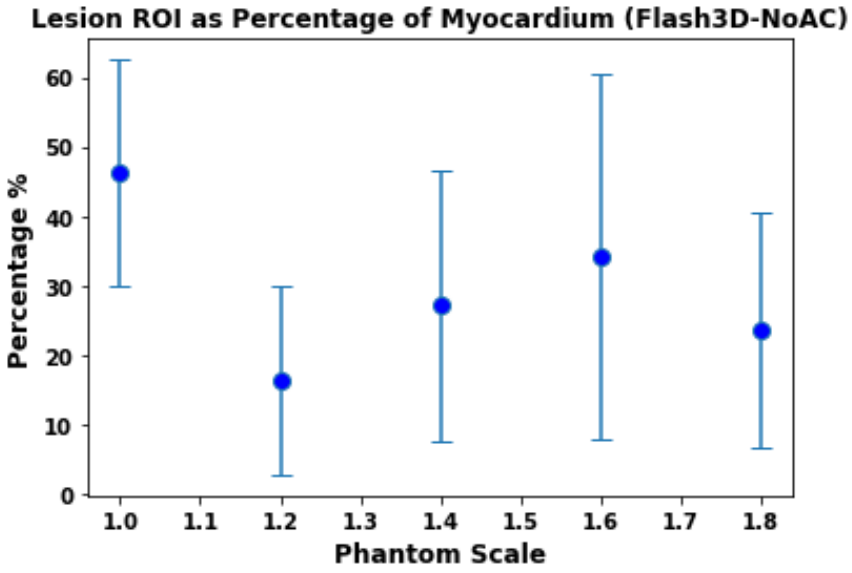

Figure 76: Plot showing the mean number of counts in the lesion ROI as a percentage of the mean number of counts in the rest of the myocardium, using FLASH3D-NoAC reconstruction. The plot does not appear to follow any particular curve. Uncertainty bars display ±SD, depicting variability in counts per voxel.

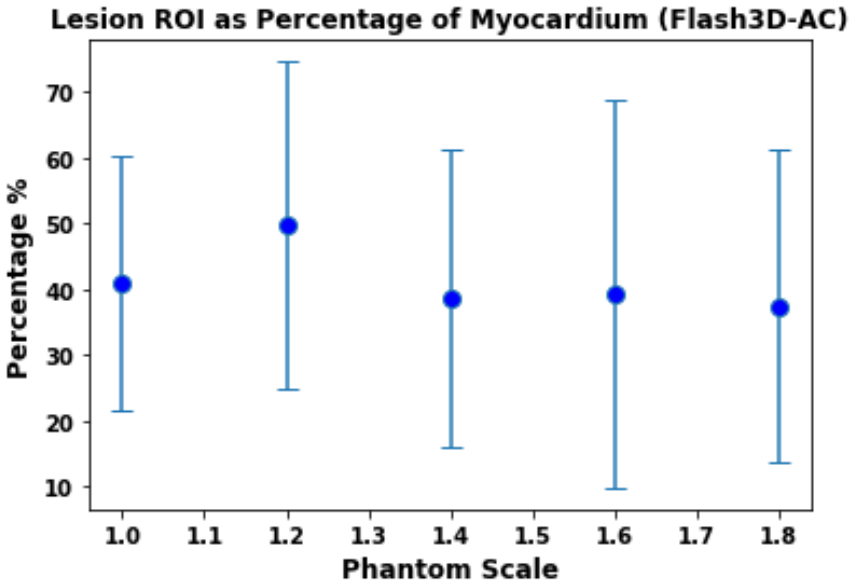

Figure 77: Plot showing the mean number of counts in the lesion ROI as a percentage of the mean number of counts in the rest of the myocardium, using FLASH3D-AC reconstruction. The plot does appears flat as patient habitus increases. Uncertainty bars display ±SD, depicting variability in counts per voxel.

The CNR of the lesion within the image follows a similar trend as the CNR between the myocardium and the background, staying generally quite flat, according to SD overlap (Figure 78).

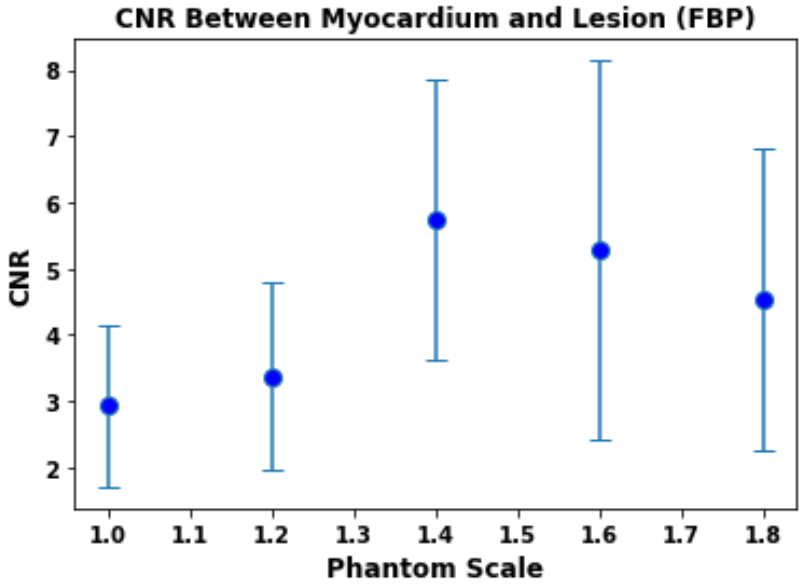

Figure 78: The CNR between the myocardium and the lesion ROI, using FBP reconstruction, showing a similar trend to that seen for CNR between the myocardium and the background. Uncertainty bars display ±SD, depicting variability in counts per voxel.

4.3.5 Qualitative Observations Study

The raw results collected as part of the Observation Study (Section 3.3.4), provided in Appendix F, were split into a range of observations. Due to time constraints only two observers were used for this study; one experienced nuclear medicine cardiologist and one radiologist with extensive nuclear medicine experience. As such, the results are not presented as statistically significant facts but rough trends to compare with the results gathered from the ROI measurements completed above. The overall sensitivity and specificity were calculated as 0.9 and 0.6, respectively. The trends seen in the observation study data complement those found through ROI measurements in ImageJ.

When split into lesion present and lesion absent, the trends observed were similar to those observed using the ROI measurements. The lesion absent images have a trend very similar to that observed in Section 4.3.3 for the mean signal in the FLASH3D-AC reconstruction (Figure 79). This shape also matches the decrease in contrast measured between the myocardium and background ROI.

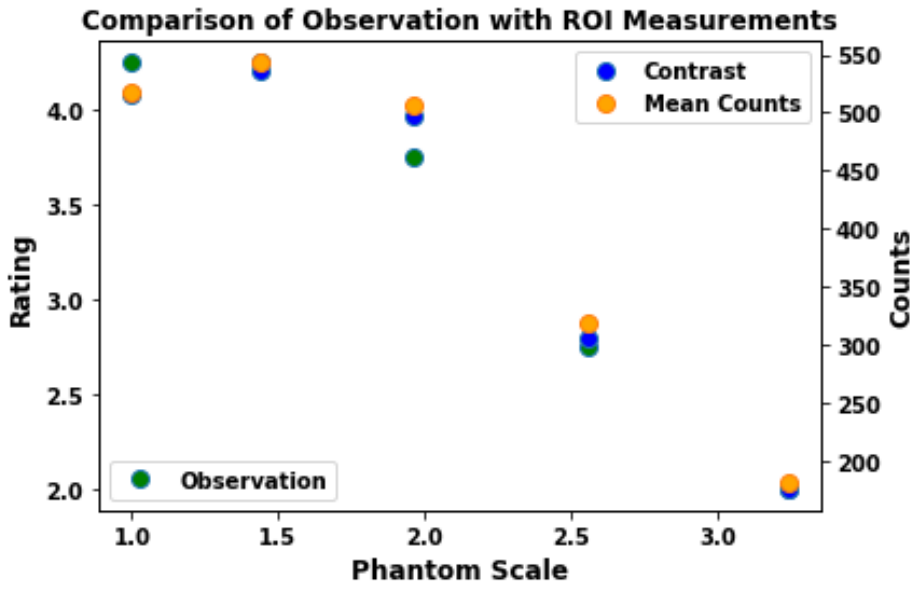

Figure 79: Comparing the mean image quality rating (green) (using both short axis and vertical long axis images) with the myocardial signal (orange), and contrast between myocardium and background (blue), for the images created using Flash3D-AC reconstruction.

The confidence the observer had in their lesion detectability decreased as patient diameter increased (Figure 80). The accuracy of the lesion detectability also decreased as patient diameter increased (Figure 81). Both decreases show a significant difference between the 1.2 and 1.4 scale phantom.

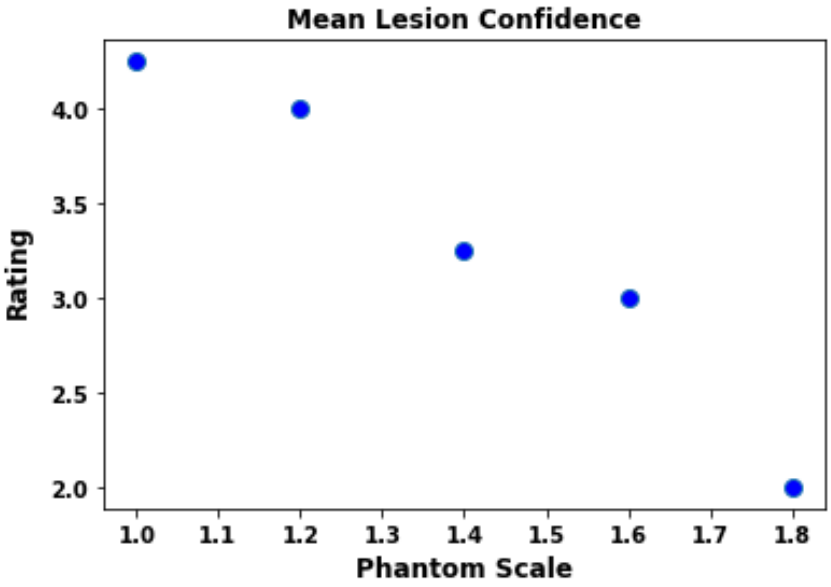

Figure 80: Mean lesion confidence rating (using both short axis and vertical long axis images) across phantom scales.

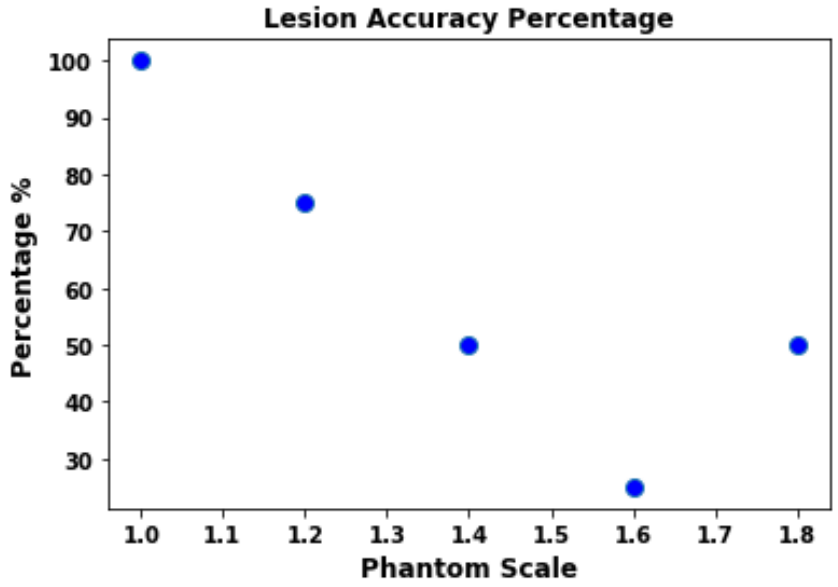

Figure 81: Mean accuracy across both the short axis and vertical long axis views

All but one of the images with a lesion present were correctly identified, by both observers. The misidentified image was the same for each (Phantom Scale 1.6, short axis view). The trend of observed image quality followed a similar trend to the lesion absent images, with a greater difference between the 1.0 and 1.2 Scale phantoms in the lesion present images (Figure 82). The trend in the decreasing confidence in lesion detectability is not a strong as for the lesion, but it is still present.

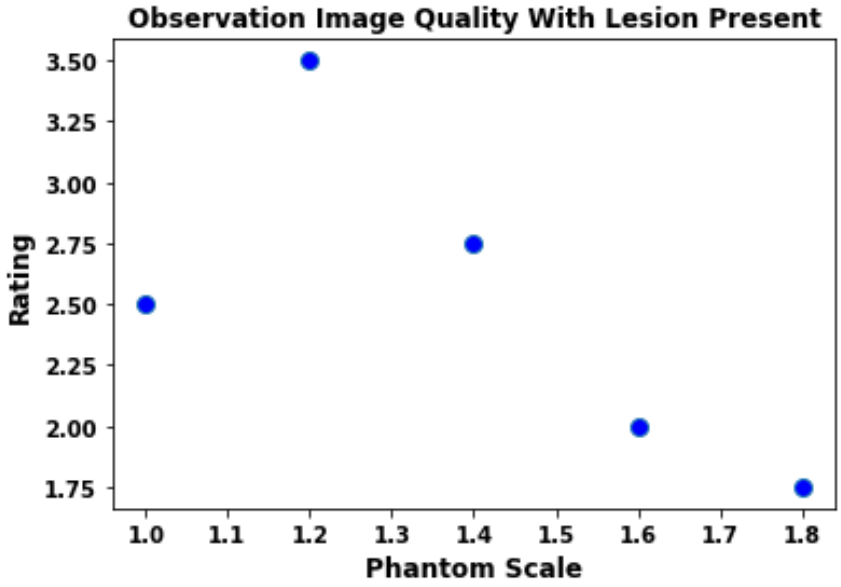

Figure 82: Mean image quality ratings given to each phantom size (including both short axis and vertical long axis views) of images with lesions present.

For the results in this part of the study to hold more weight, a larger number of independent observers would be required. Observer studies include a natural bias, due to their reliance on the opinion of the viewer, based on their individual experience. For this study, the inclusion of the observer study compliments the ROI measurements but it would not be sufficient to base a conclusion on such a small frame of reference.

5 Discussion

Each section of this project had its own aims, working towards the final goal of producing a simulation that could be used as a tool to answer clinically relevant questions involving SPECT scans, specifically MPI. How successful each component was in achieving its aims is discussed in this chapter, followed by suggestions for where this project could be continued in future.

5.1 Development of a Monte Carlo simulation

The goal of the first stage of this project was to model a Symbia T2 SPECT system, as used at Christchurch Hospital, within a Monte Carlo simulation. This model was then validated against the hospital system, to ensure it produces data comparable with the original system.

The simulation needs to imitate the physical system as closely as reasonably possible to be able to apply any results to a real-world scenario. While developing and verifying a SPECT setup in a Monte Carlo simulation is not a new task in a general sense, this set up is specific to the Symbia T2 gamma camera in use at Christchurch Hospital and is calibrated for ^{99m}Tc studies. While the focus for the rest of the thesis is on MPI, the same camera set up could be used for another study, outside of MPI, if the activity was simulated elsewhere. Ensuring accuracy of the simulation is essential if this work is to continue beyond this study and produce reliable data, which can be used to help improve patient care at Christchurch Hospital.

To say a simulation is a good representation of a physical system, it must be shown that results produced by the simulation agree within statistical uncertainty to those produced by the physical system. In the case of an imaging detector, two key factors that need to be shown to be comparable are the spatial and energy resolutions. As calculated in Section 4.1, the spatial resolution of the simulation is $11.96\ mm\ \pm 0.20\ mm$ (95% CI), while the spatial resolution of the Symbia system is $11.87\ mm\ \pm 0.15\ mm$ (95% CI). Within uncertainty these values agree, indicating the spatial resolution of the simulated system is a sufficiently accurate representation of the Symbia system at Christchurch Hospital. The energy resolution for the Symbia system at Christchurch Hospital was reported to be 9.5%, which falls within the range of $9.43\% \pm 0.17\%$ for the simulated system. Therefore, based on these results, the simulated system is an accurate representation of the Symbia T2.

The simulated flood field image of a uniform distribution of signal on the detector is important as it indicates there is no part of the detector that has greater (or lower) sensitivity than the rest. While it is unlikely for this to be a problem in a simulated setup, if it were non-uniform, the images produced would not give a clear indication of the real state of the patient being imaged. Part of the image would appear brighter or dimmer than the rest, potentially resulting in a misdiagnosis. In a simulated setup, this extrinsic test is another confirmation that the collimator is modelled correctly.

To make the most of this simulation setup in the time available for this project, a large number of CPUs were employed across several servers. While unlikely, there was the possibility of different processors responding differently to the GATE install, and therefore producing a different outcome from the same set of starting variables. This was clearly not the case, however, as the three servers produced identical outcomes for the same simulation, starting with the same seed. Any further output from these servers can be directly added and/or compared, as if they were completed by the same machine.

At the time of writing, it was announced within the GATE community that a feature within the software was being fixed that would allow for timing of simulations to be reduced. This fix involves allowing two sets of detector heads to collect data simultaneously. The second pair of detectors would be the same as the first pair, placed at a later point in time. This would allow four detector heads, in correctly spaced pairs, to collect data up to twice as fast as this current setup. Currently, the activity within the patient at the start of each projection angle is calculated to account for the decay that had occurred at previous projection angles – by introducing detector heads from two points in time in one simulation, this current correction may need to be altered. Considering the time simulated for a full scan is about 15 minutes, and the half-life of ^{99m}Tc is about six hours, removing the time correction for each simulation would not have a great effect on the final outcome. As time is still a major limitation to this project it is a strong recommendation that this, and any future updates, be taken full advantage of.

While there will always be room for improvement in both speed and performance, this simulation setup has been shown to accurately imitate the response of the Symbia T2 gamma camera in its use at Christchurch Hospital. The spatial and energy resolutions measured fell within the acceptable uncertainty of the hospital system, the image produced was shown to be uniform across the detector, and the different computer servers in use produce the same output from the same input parameters.

5.2 Characterisation of a Digital Phantom

The goal of the second stage of this project was to properly characterise a digital human phantom that could be used within the developed simulation. To make sure the phantom was introduced correctly into the simulation, a series of tests were completed, looking for any results that were not as expected. Each unexpected result helped refine the process for introducing the phantom files into the simulation, while each result that showed what was expected confirmed the method in place.

One expected result was found when testing the use of the phase space file. The relative intensities within the projection image at 0° confirmed the presence of a bright ring, with a dimmer centre. If the phase space file had not worked the way it was intended, and instead released the photons as if it were the origin, the projection image would have had more even intensity, as the photons would have been evenly distributed across the pericardium. Instead, the brighter edging showed that the original source's placement, predominantly within the myocardium, was still affecting the final projection image.

An unexpected result was the appearance of the artefact within the reconstructed image. After eliminating several potential causes, it was found that the nipple mesh on the body STL file was where the artefact was introduced. The cause for the defect was identified as being due to the orientation of the mesh representing the nipple on the phantom. Each mesh is assigned an "inside" face and an "outside" face, indicating to the photons at the mesh boundary what material they are leaving and what material they are entering. The nipple mesh was originally orientated so the outer surface was assigned the "outside" setting but this seems to have resulted in a change in the apparent attenuation of photons by the phantom, making the projection images brighter than expected. With the nipple meshes removed, this extra brightness is not observed. To explore the problem further, another test was done where the nipple meshes were included with the "inside" face on the outside. This test behaved the same way as the test with the nipple meshes removed completely, with no enhanced brightness present in the projection images. Other organs were then included, to check if similar behaviour could be observed from their current orientation. No other bright anomalies were observed, so no further investigation was done. It was decided to continue to run simulations without the nipple meshes included, as the reason for the surprising interaction between the meshes and the photons was still unknown. The added thickness of the nipple meshes would not cause a significant change in the attenuation of the photons if they were removed, so it was assessed to be reasonable to remove them.

5.3 Application of the Monte Carlo Simulation with the XCAT Phantom

The goal of the third stage of this project was to use the developed simulation, in conjunction with a phantom representing patient geometry, to investigate the change in image quality with patient size. In this proof-of-concept study, simulations were completed to show the decrease in image quality with an increase in patient size and the associated change in visibility of a heart defect within the reconstructed image.

The key finding of interest in the GATE output is that a change did occur that appeared to have some reliance on the phantom scaling factor. Visually, the contrast between the signal from the heart and the scatter surrounding the heart decreases as patient size increases. There is also some detail that is visible in the projection images at phantom scales of 1.0 and 1.2 that cannot be identified in the larger phantoms projection images. For example, in the montages provided in Section 4.3.1, the darker ring representing the myocardium of the left ventricle can be identified in projection 31 and 41 of the Phantom Scale 1.0 montage, but that contrast is all but obscured in the Phantom Scale 1.8 montage. That there is such clear change through the projection images is important in knowing that the simulation is sensitive to the change in patient habitus.

The mean counts per voxel within the heart ROI, after reconstruction within MATLAB shows a $1/r^3$ trend. This trend is later repeated throughout many of the Syngo reconstructions, as well. A relationship of $1/r^3$, rather than being directly inversely proportional as the thickness changes, is believed to relate to the fact the photons are emitted in all directions, and can be visualised as an expanding sphere of photons. Photons in all directions are undergoing greater attenuation at larger patient sizes, resulting in an overall $1/r^3$ relationship that is seen in these reconstructions.

5.3.1 Syngo Reconstructions

The signal for both Syngo FBP and Flash3D-NoAC follow the same $1/r^3$ trend as the MATLAB reconstruction. The Flash3D-AC reconstruction, however, does not. The trend for this reconstruction type is not clear, based on the number of phantom sizes used in this study. It could be said that the curve peaks at Phantom Scale 1.2, then follows an exponential decrease across to the level of Phantom Scale 1.8. Another interpretation could be that the whole range follows an exponential decrease with the first few data points fluctuating around the trend lines. This interpretation would rely heavily on the uncertainty bars around each data point. After looking further into how the attenuation correction method works in Syngo, however, a further possibility is that the results from the first three patient

sizes are fluctuating around a mean value. The program is designed to use the given attenuation maps to correct the signal received by the detector to account for the attenuation of photons as they pass through different media. As the phantom thickness increases, the software is working to correct for the change in signal seen by the reconstruction techniques not using attenuation correction. That results in the first three patient sizes sitting around the fluctuations of a flat line. The larger two phantoms are pushing the reconstruction technique to the point that it struggles to keep the signal boosted in the same way it could for the first three phantoms. The shape of the graph in the region of the largest phantoms is uncertain. It could be that between phantom 1.4 and 1.6 the signal begins to drop away linearly, or even following the $1/r^3$ curve seen in the other reconstruction methods. It could also be a stepping function, working to keep the signal constant at a second, lower threshold than what the smaller phantoms are corrected to. Which trend is correct cannot be observed from this graph. A more extensive range of phantom sizes, or a smaller step size between phantoms in the current range, would be required for this to be known with certainty.

While the signal from the myocardium for FBP and Flash3D-NoAC follows a $1/r^3$ trend, the signal from the left ventricle appears to decrease more linearly. The signal from within the ventricle itself is likely to follow the same $1/r^3$ trend across patient sizes, however the ventricle ROI is likely to include a greater number of scattered photons from the myocardium as patient thickness increases. It is proposed that the competing mechanisms result in an approximately linear decrease in signal overall.

The plot of SNR for images reconstructed using either FBP or Flash3D-AC methods would appear to indicate a significant decrease in image quality between the 1.0 and 1.2 scale phantoms. Such a significant decrease at such a relatively small increase in phantom size does not match the observations made visually of the reconstructed slices. The measurements would indicate that the standard level of activity was only adequate for patients of average body habitus. Another possibility would be that the phantom representing the average male was simulated with more activity than was necessary to produce a diagnostic scan. SNR alone is not enough to determine the diagnostic quality of a scan, however, and so further observations must be made before conclusions are drawn.

Some of the problems associated with choosing an appropriate background ROI for SNR and CNR calculation could be reduced by including a uniform background, through a body blood pool. Currently the standard deviation of the background signal drops away towards zero the further the ROI is from the myocardium. By including the body blood pool, the background standard deviation would no longer be dependent on the ROI's distance from the myocardium. This could result in a lower SNR for the images. For CNR, including a uniform background would have less effect unless the measurement was the CNR between the myocardium and the background.

The comparisons between the mean counts per voxel from the myocardium of the lesion-free phantom and the lesion-present phantom acts as an extra confirmation that the simulation is working as expected. The activity with the myocardium ROI of the lesion-present images was scaled to allow for the lesion volume, which would not have any activity taken up within it. These calculations resulted in counts that agreed closely with the original, lesion-free, images.

The lesion visibility results are not what were expected. It was expected that the activity within the lesion, relative to the activity within the myocardium, would increase as the phantom scale increased, due to an increase in scattering by the phantom. This is not what was measured – rather, the lesion ROI as a percentage of the myocardium ROI held relatively steady across the phantom sizes. It is possible that the lesion size chosen was too large to be able to observe the expected effect. A large lesion would have a large number of voxels that would not greatly increase in number of counts, even at higher phantom scales. A smaller lesion, half the size, for example, would be influenced far more strongly by the scattered photons from the surrounding healthy tissue than the large lesion used in this study.

5.3.2 Qualitative Observations Study

While in general image quality is best described by metrics such as SNR and CNR, the lack of realistic background present in the simulation images means the observer image quality ratings align well with the change in signal as patient diameter increases, rather than the change in SNR or CNR.

The confidence the observer had in their lesion detectability decreased as patient diameter increased, as did the accuracy of the lesion detectability. Both decreases show a significant difference between the 1.2 and 1.4 scale phantom, potentially indicating that it is between these two scales that an increase in administered activity could be needed to boost the image quality for larger patient habitus. This indication needs further evednce to support it, however.

The trend of observed image quality followed a similar trend in both the lesion-free and lesion-present images, with a greater difference between the 1.0 and 1.2 Scale phantoms in the lesion present images. The trend in the decreasing confidence in lesion detectability is not a strong as for the lesion, but it is still present.

It was expected that the number of lesions present but not observed would go up as patient diameter increased. While this was true the greatest effect on misdiagnosis came from the observation of lesions that were not truly there. These false positives are due to the decreasing image quality making the reconstructed images appear less smooth at larger patient sizes. The indication is then that a

smaller lesion would also become less visible at a smaller phantom size than the lesion used in this study.

It is also interesting to note that the one lesion present that was not identified was in an image with an image quality rating, and lesion detectability confidence, of one. This indicates that while it was decided that the image had no lesion present, the observer had very low confidence in that decision being accurate, and the image was not judged to be of diagnostic quality. Of all the images rated as being of diagnostic quality (an overall image quality rating of 3 or above), no lesion was unobserved. However, several images giving a high image quality rating were observed to have lesions that were not present.

For the results in this part of the study to hold more weight, a larger number of independent observers would be required. Observer studies include a natural bias, due to their reliance on the opinion of the viewer, based on their individual experience. For this study, the inclusion of the observer study compliments the ROI measurements but it would not be sufficient to base a conclusion on such a small frame of reference.

5.3.3 General Discussion

The results gathered from the above reconstruction methods show a definite decrease in image quality, but not with the clear cut-off in diagnostic quality that was expected. The absence of activity from other tissues within the image may have had some effect on this, but so did the extra corrections provided within the reconstruction methods. A reason the CNR for the difference sized phantoms comes out approximately equal, may be due to the ability of Syngo to boost the signal of the low count images without also increasing the effect of noise in the image. It would be interesting to see if this is still true if a further study includes a background blood pool or other source of background noise.

At the time of planning this project, the ability to observe only the change in counts relating to the myocardium was of great interest, as it is something that cannot be observed in a human patient study. However, while this is an interesting observation to be able to make, the inclusion of a background blood pool, if not a selection of other organ activity uptakes, may provide results with closer ties to clinical application.

A limitation of this study is in the way patient habitus is only modelled through an increased volume of adipose tissue around the patient. While it is an advantage of Monte Carlo methods to be able to observe the effect of changing only one parameter (here, the volume of adipose tissue surround an average stature person), there are many different builds, even of patients of similar heights.

Another limitation is that this proof of concept only observes the relationship between image quality and patient habitus for male phantoms. Due to the proof of concept nature of this study, this limitation does not pose an immediate problem to the nature of the results gathered – steps to include a digital phantom in the GATE simulation have been outlined, and the sensitivity of the simulation to the change in patient habitus has been confirmed.

5.4 Future Work

The work presented in this thesis sits as the foundations of an optimisation study in MPI SPECT scans. The simulation developed could also be applied to other studies implementing the Symbia T2 gamma camera, but particular work was put into preparing phantoms and sources for the MPI studies. While significant progress was made throughout this work, new developments within the GATE program, and results noted during the testing phase of this project, leave room for improvement for the next phase.

One such improvement is the introduction of independent RORs for each detector head. Using the Generic Repeater option within GATE v9.1 would allow the use of body contouring, which is a better representation of the clinical method. Implementing this method would include calculating the location and angle of the detector at each location around the body. This process could be made easier by implementing python to calculate the locations and angles, and a program such as GNU Parallel to input the correct set of values for each simulation. The same update that allowed independent RORs to be defined for the two heads currently in use, would also allow a second set of detectors to be placed within the simulation. The four heads, if placed in a way that they do not overlap, would halve the number of simulations to be run per phantom.

Along with including independent RORs, a further extension of the simulation would be to use the 4-dimentional aspect of the XCAT phantom to include heart beat motion. This would open the way for a gated simulation, modelling the gated MPI scans that are now routine in many centres.

Additions to the simulation that could be considered for future applications also include the addition of a background blood pool and the patient bed. The added activity in the blood pool would increase the simulation time but, to minimise that increase, a limited pool could be included rather than the whole body – only within the field of view, for example. The patient bed would be designed to match the specifications of the bed used at Christchurch Hospital. The blood pool would result in a more uniform background for the reconstructed images, while the patient bed would improve the representation of scatter and attenuation in the simulation.

Including a greater number of simulations within future tests would also give a clearer understanding of the shape of the trends. Both increasing the maximum scaling factor, and decreasing the step size between each factor would help give a better understanding of the relationships observed, especially for those using FLASH3D-AC reconstruction. Decreasing the size of the lesion, or creating a variety of lesion sizes and locations, would also help provide a clearer understanding of the requirements for a diagnostic quality image.

In terms of the optimisation study that was the clinical question in mind, driving the development of this simulation, the relationship between image quality and patient habitus explored in this thesis is only a start. Another relationship to explore would be that between administered activity and image quality. The relationship found there could be used to develop a metric, relating activity with image quality for a given patient size. The metric could then be expanded to other patient sizes through the relationship observed between image quality and patient habitus.

Future research would benefit from building on the limitations present within this study, as discussed above. Including alternative phantoms would allow for scaling of body organs, representing patients of different stature. This would give a better understanding of a wider range of patient sizes, better representing the range that can be present within a clinical setting, not just focusing on average stature patients with extra adipose tissue.

6 Conclusion

This project developed a Monte Carlo simulation modelling a SPECT camera system used at Christchurch Hospital. This simulation was then used in a proof of concept study to explore the different relationships between image quality and patient habitus. The results of this project can be used as the first stages of an optimisation study in myocardial perfusion imaging for the Nuclear Medicine Department at Christchurch Hospital.

As outlined in Chapter 3, a Monte Carlo simulation fitting the specifications required by this project was developed using GATE. The simulation was created to model the Symbia T2 SPECT system at Christchurch Hospital. The simulation was validated against the Christchurch Hospital system. Measurements of the spatial and energy resolutions fell within the acceptable uncertainty of the hospital system, showing the results gathered by the simulation could be viewed as a reasonable representation of the real-world system.

After validation, the simulation was used in conjunction with the XCAT mesh phantom to produce myocardial perfusion SPECT images for a range of patient sizes. The reference phantom, representing the average adult male, was scaled to produce patients of increasing body habitus while keeping consistent height and organ size. The 3-D software Rhino 6 was used to ensure each phantom was imported into GATE with the heart in the same relative location, for ease of set up and reproducibility. An issue was discovered in the interactions between the photons and the phantom, resulting in a defect in the reconstructed images. Through a series of tests, it was found the issue lay with the nipple mesh of the body file. This mesh was removed and the problem was resolved.

Using the developed Monte Carlo simulation made it possible to study the change in quality of reconstructed images for different body habitus by only simulating the myocardial and heart blood pool uptake of the radiopharmaceutical. This is not possible with human studies. Furthermore, reducing the activity simulated allowed for significant reductions simulation times. However, it is reliant upon the data provided in the ICRP publications and it does make the assumption that the myocardial uptake of the radiopharmaceutical is independent of body habitus.

The output from the simulations were attached to a DICOM template, allowing them to be read by Syngo and reconstructed following clinical protocols. Three reconstruction methods were used in Syngo: filtered back projection (FBP); Flash3D iterative reconstruction with attenuation correction

(Flash3D-AC); and Flash3D iterative reconstruction without attenuation correction (Flash3D-NoAC). A basic FBP reconstruction was also performed in MATLAB.

The MATLAB reconstruction showed the relationship between the number of counts in the reconstructed image and patient habitus, without any extra settings that are within the Syngo reconstruction algorithms. The trend observed was a $1/r^3$ relationship between number of counts and phantom scaling factor.

The image quality of each Syngo reconstructed image was examined through the calculation of mean signal, SNR and CNR. The plots of each image quality metric were used to observe the change as patient habitus increased. It was found that the mean signal from the myocardium in both FBP and Flash3D-NoAC followed an approximate $1/r^3$ trend, while Flash3D-AC managed to keep the relative counts between phantom scales relatively consistent before falling away at the largest phantom sizes.

The images produced by the Flash3D-AC reconstruction were viewed by physicians and rated on image quality and confidence in lesion detectability. The observations supported the trends in signal and contrast that were found through measurements in ImageJ. While further study is needed to back-up the observations of such a small pool of observers, the ratings given indicate the potential need to increase the administered activity above the patient habitus relating to Phantom Scale 1.2.

The simulation developed in this project is suitable for use in any Monte Carlo simulation study relating to ^{99m}Tc SPECT. In particular, this project applied the developed simulation, in conjunction with the XCAT phantom, in a SPECT MPI study. The simulation was found to be sensitive to changes in phantom scaling, and the output was successfully introduced to Siemen's clinical reconstruction software, Syngo. The simulation developed throughout this thesis, and the future developments suggested, can be used as a useful tool in answering clinical questions relating to SPECT MPI.

References

[1] M. M. Khalil, Ed., *Basic Sciences of Nuclear Medicine*. Springer-Verlag, 2011. [Online]. Available: https://books.google.co.nz/books?hl=en&lr=&id=GrYH6zb7xzkC&oi=fnd&pg=PR3&dq=nuclear+medicine&ots=oRe_sxkcKL&sig=cf8ZoR1dghRJhLMQ-odOlwBX0cQ&redir_esc=y#v=onepage&q&f=false

[2] R. Zimmermann, *Nuclear Medicine: Radioactivity for Diagnosis and Therapy*, 2nd ed. EDP Sciences, 2017.

[3] A. Webb, *Introduction to Biomedical Imaging*. John Wiley & Sons, Inc., 2003.

[4] W. B. Saunders, 'Chapter 16 - Cardiac System', in *Nuclear Medicine*, 4th ed., H. A. Ziessman, J. P. O'Malley, and J. H. Thrall, Eds. 2014, pp. 378–423. [Online]. Available: https://doi.org/10.1016/B978-0-323-08299-0.00016-X.

[5] 'Major causes of death', *Ministry of Health*, Aug. 2018. https://www.health.govt.nz/our-work/populations/maori-health/tatau-kahukura-maori-health-statistics/nga-mana-hauora-tutohu-health-status-indicators/major-causes-death (accessed Jan. 14, 2021).

[6] Ministry of Health, 'ORS C2: Code of Practice for Nuclear Medicine', Ministry of Health, Wellington, 2018. Accessed: Jul. 14, 2020. [Online]. Available: https://www.health.govt.nz/system/files/documents/publications/code-practice-nuclear-medicine-apr19.pdf

[7] A. J. Ramon *et al.*, 'Investigation of dose reduction in cardiac perfusion SPECT via optimization and choice of the image reconstruction strategy', *J. Nucl. Cardiol.*, vol. 25, no. 6, pp. 2117–28, 2018, doi: 10.1007/s12350-017-0920-1.

[8] E. Papanastasiou, E. Theodoridou, A. Doumas, G. Gerasimou, and A. Siountas, 'A study on the optimization of the administered activity in myocardial perfusion SPECT imaging with Tc-99m according to body measurements', *Phys. Med.*, vol. 68, pp. 69–74, 2019, doi: https://doi.org/10.1016/j.ejmp.2019.11.011.

[9] M. K. O'Connor, E. Bothun, and R. J. Gibbons, 'Influence of patient height and weight and type of stress on myocardial count density during SPECT imaging with Thallium201 and Technetium99m-sesstamibi', *J. Nucl. Cardiol.*, vol. 5, no. 3, pp. 304–12, 1998.

[10] A. Notghi, F. X. Sundram, J. W. O'Brien, and N. B. Smith, 'Assessing the effect of increasing injection activity for myocardial perfusion imaging in overweight patients', *Br. J. Radiol.*, vol. 81, pp. 730–734, 2008, doi: 10.1259/bjr/60645843.

[11] A. Notghi, N. Williams, N. Smith, S. Goyle, and L. K. Harding, 'Relationship between myocardial counts and patient weight: adjusting the injected activity in myocardial perfusion scans', *Nucl. Med. Commun.*, vol. 24, pp. 55–59, 2003, doi: 10.1097/01.mnm.0000051632.18733.c1.

[12] J. C. Taylor, S.-A. Froberg, P. G. Hillel, A. M. Harris, and W. B. T. Tindale, 'Correlation of left ventricular count rate with patient weight in Tc-99m myocardial perfusion imaging', *Nucl. Med. Commun.*, vol. 32, no. 4, pp. 279–283, 2011, doi: 10.1097/MNM.0b013e328342e9d9.

[13] C. N. Robinson *et al.*, 'The relationship between administered radiopharmaceutical activity in myocardial perfusion scintigraphy and imaging outcome', *Eur. J. Nucl. Med. Mol. Imaging*, vol. 35, pp. 329–335, 2008, doi: 10.1007/s00259-007-0597-9.

[14] E. J. Hall, *Radiobiology for the Radiologist*, 3rd ed. J. B. Lippincott Company, 1988.

[15] S. Staelens and I. Buvat, 'Monte Carlo Simulations in Nuclear Medicine Imaging', in *Advances in Biomedical Engineering*, Elsevier B.V., 2009, pp. 175–207.

[16] B. Faddegon *et al.*, 'The TOPAS tool for particle simulation, a Monte Carlo simulation tool for physics, biology and clinical research', *Phys. Med.*, vol. 72, pp. 114–121, Apr. 2020, doi: 10.1016/j.ejmp.2020.03.019.

[17] M. T. Bahreyni Toossi, J. Pirayesg Islamian, M. Momennezhad, M. Ljungberg, and S. H. Naseri, 'SIMIND Monte Carlo simulation of a single photon emission CT', *J. Med. Phys.*, vol. 35, no. 1, pp. 42–47, 2010, doi: 10.4103/0971-6203.55967.

[18] M. E. Crestoni, 'Radiopharmaceuticals for Diagnosis and Therapy', in *Reference Module in Chemistry, Molecular Sciences and Chemical Engineering*, Elsevier, 2018. [Online]. Available: http://www.sciencedirect.com/science/article/pii/B9780124095472142052

[19] A. Celler, 'Single Photon Imaging, Applications', in *Encyclopedia of Spectroscopy and Spectrometry*, 3rd ed., Elsevier, 2017, pp. 76–83. [Online]. Available: http://www.sciencedirect.com/science/article/pii/B9780128032244000078

[20] N. Lanconelli, 'The importance of Monte Carlo simulations in modelling detectors for Nuclear Medicine', *Math. Comput. Simul.*, vol. 80, no. 10, pp. 2109–2114, 2010, doi: 10.1016/j.matcom.2010.04.004.

[21] 'Collimators for Nuclear Medicine', *Nuclear Fields*, 2017. http://www.nuclearfields.com/collimators-nuclear-medicine.htm (accessed Jan. 27, 2021).

[22] S. R. Cherry, J. A. Sorenson, and M. E. Phelps, *Physics in Nuclear Medicine*, 3rd ed. Saunders, 2003.

[23] G. L. Zeng, J. R. Galt, M. N. Wernick, R. A. Mintzer, and J. N. Aarsvold, 'Single-Photon Emission Computed Tomography', in *Emission Tomography: The Fundamentals of PET and SPECT*, 1st ed., Elsevier Science & Technology, 2004, p. 597.

[24] M. Lyra and A. Ploussi, 'Filtering in SPECT Image Reconstruction', *Int. J. Biomed. Imaging*, vol. 2011, no. 693795, 2011, doi: 10.1155/2011/693795.

[25] P. P. Bruyant, 'Analytic and iterative reconstruction algorithms in SPECT', *J. Nucl. Med.*, vol. 43, no. 10, pp. 1343–58, Oct. 2002.

[26] H. Azhari, J. A. Kennedy, N. Weiss, and L. Volokh, 'Nuclear Medicine: Planar and SPECT Imaging', in *From Signals to Image*, Springer, Cham, 2020, pp. 159–215.

[27] M. Lyra, A. Ploussi, M. Rouchota, and S. Synefia, 'Filters in 2D and 3D Cardiac SPECT Image Processing', *Cardiol. Res. Pract.*, vol. 2014, p. 963264, 2014, doi: 10.1155/2014/963264.

[28] K. Van Laere, M. Koole, I. Lemahieu, and R. Dierckx, 'Image filtering in single-photon emission computer tomography: principles and applications', *Comput. Med. Imaging Graph.*, vol. 25, no. 2, pp. 127–133, 2001, doi: 10.1016/S0895-6111(00)00063-X.

[29] H. M. Hudson and R. S. Larkin, 'Accelerated Image Reconstruction Using Ordereed Subsets of Projection Data', *IEEE Trans. Med. Imaging*, vol. 13, no. 4, pp. 601–609, 1994, doi: 10.1109/42.363108.

[30] K. M. Jones *et al.*, 'Use of quantitative SPECT/CT reconstruction in 99mTc-sestamibi imaging of patients with renal masses', *Ann. Nucl. Med.*, vol. 32, pp. 87–93, 2018, doi: 10.1007/s12149-017-1222-z.

[31] E. B. Podgorsak, *Radiation Physics for Medical Physicists*, 3rd ed. Springer, 2016.

[32] V. Venugopal and P. S. Bhagdikar, 'de Broglie Wavelength and Frequency of the Scattered Electrons in Compton Effect', *Phys. Educ.*, vol. 29, no. 1, 2012, [Online]. Available:

http://canterbury.summon.serialssolutions.com/2.0.0/link/0/eLvHCXMwdV1NSwMxEB3UkyBi8du2zh9o3c1Hs3uU0sVbBQW9LUk2W3tZZbsW_fdOkhaK0HNCGBIy8wbeewPA2TgZ_csJ2tmUZ1pMDOd5JhPLLFdGOEPJ0rhA-t0RvcL9Vhqj25_lOtoFm9VDSp36WEhFKfeQsTCoYf5OqDLs2ikLxRmcbvAcPsYH6MGBa87huXJI_e2C8B2-aT_aoVl0H0hNOxZt5C7_4meNBL7wxQaHS1fhbDORZoXLBv0_JViG0V34AobF7HX6NAoxlF_RIqL0kZY-Un4JJ9pz1ZsuaNqqa0DHpNVCVUpOrJDG5pl1tU7SrBYqZ1bdwNWe0273rtzBMZVyFsTWaR-OuvbbDbbMSf88w3BZfzHudgs

[33] L. Laakkonen, 'Monte Carlo simulations of spectral properties of clinical photon beams with Geant4', Master's, University of Jyvaskyla, Finland, 2019. [Online]. Available: https://jyx.jyu.fi/bitstream/handle/123456789/66408/1/URN%3ANBN%3Afi%3Ajyu-201911184912.pdf

[34] G. Choppin, J.-O. Liljenzin, J. A. N. Rydberg, and C. Ekberg, *Radiochemistry and Nuclear Chemisty*, 4th ed. Elsevier Science & Technology, 2013.

[35] I. Singh, B. Singh, B. S. Sandhu, and A. D. Sabharwal, 'Comparative study for intermediate crystal size of NaI(Tl) scintillation detector', *Rev. Sci. Instrum.*, vol. 91, no. 7, 2020, doi: 10.1063/5.0005243.

[36] M. Kurudirek, 'Effective atomic numbers and electron densities of some human tissues and dosimetric materials for mean energies of various radiation sources relevant to radiotherapy and medical applications', *Radiat. Phys. Chem.*, vol. 102, pp. 139–146, Sep. 2014, doi: https://doi.org/10.1016/j.radphyschem.2014.04.033.

[37] *Quality assurance for SPECT systems*. Vienna: INTERNATIONAL ATOMIC ENERGY AGENCY, 2009. [Online]. Available: https://www.iaea.org/publications/8119/quality-assurance-for-spect-systems

[38] S. Dorbala *et al.*, 'Single Photon Emission Computed Tomography (SPECT) Myocardial Perfusion Imaging Guidelines: Instrumentation, Acquisition, Processing, and Interpretation', *J. Nucl. Cardiol.*, vol. 25, no. 5, pp. 1784–1846, Oct. 2018, doi: 10.1007/s12350-018-1283-y.

[39] J. T. Bushberg, J. A. Seibert, and E. M. Leidholdt, *The essential Physics of Medical Imaging*, 3rd ed. Wolters Kluwer Health, 2011.

[40] 'Myocardial Perfusion Scan, Stress', *John Hopkins Medicine*, 2020. https://www.hopkinsmedicine.org/health/treatment-tests-and-therapies/myocardial-perfusion-scan-stress (accessed Sep. 07, 2020).

[41] 'Myocardial Perfusion Scan', Nuclear Medicine Department, Christchurch Hospital, Christchurch, New Zealand, 3, Mar. 2018.

[42] M. Havel, M. Kolacek, M. Kamlnek, V. Dedek, O. Kraft, and P. Slrucek, 'Myocardial perfusion imaging parameters: IQ-SPECT and conventional SPECT system comparison', *Hell. J. Nucl. Med.*, vol. 17, no. 3, pp. 200–203, 2014.

[43] Lucid Equipment, *Siemens Symbia S functionality*, (2020). Accessed: Dec. 14, 2020. [Online Video]. Available: https://www.youtube.com/watch?v=3Xr0E3_swKY

[44] A. Notghi, F. X. Sundram, J. W. O'Brien, and N. B. Smith, 'Assessing the effect of increasing injection activity for myocardial perfusion imaging in overweight patients', *Br. J. Radiol.*, vol. 81, pp. 730–734, 2008, doi: 10.1259/bjr/60645843.

[45] A. J. Ramon *et al.*, 'Investigation of dose reduction in cardiac perfusion SPECT via optimization and choice of the image reconstruction strategy', *J. Nucl. Cardiol.*, vol. 25, no. 6, pp. 2117–28, 2018, doi: 10.1007/s12350-017-0920-1.

[46] M. K. O'Connor, E. Bothun, and R. J. Gibbons, 'Influence of patient height and weight and type of stress on myocardial count density during SPECT imaging with Thallium201 and Technetium99m-sesstamibi', *J. Nucl. Cardiol.*, vol. 5, no. 3, pp. 304–12, 1998.

[47] A. Notghi, N. Williams, N. Smith, S. Goyle, and L. K. Harding, 'Relationship between myocardial counts and patient weight: adjusting the injected activity in myocardial perfusion scans', *Nucl. Med. Commun.*, vol. 24, pp. 55–59, 2003, doi: 10.1097/01.mnm.0000051632.18733.c1.

[48] J. C. Taylor, S.-A. Froberg, P. G. Hillel, A. M. Harris, and W. B. T. Tindale, 'Correlation of left ventricular count rate with patient weight in Tc-99m myocardial perfusion imaging', *Nucl. Med. Commun.*, vol. 32, no. 4, pp. 279–283, 2011, doi: 10.1097/MNM.0b013e328342e9d9.

[49] E. Papanastasiou, E. Theodoridou, A. Doumas, G. Gerasimou, and A. Siountas, 'A study on the optimization of the administered activity in myocardial perfusion SPECT imaging with Tc-99m according to body measurements', *Phys. Med.*, vol. 68, pp. 69–74, 2019, doi: https://doi.org/10.1016/j.ejmp.2019.11.011.

[50] IAEA, *Nuclear Medicine Physics: A Handbook for Teachers and Students*. IAEA, 2015.

[51] Y.-Q. Zhang *et al.*, 'The image quality, lesion detectability, and acquisition time of 18F-FDG total-body PET/CT in oncological patients', *Eur. J. Nucl. Med. Mol. Imaging*, vol. 47, pp. 2507–2515, 2020, doi: 10.1007/s00259-020-04823-w.

[52] M. Ljungberg, S.-E. Strand, and M. A. King, Eds., *Monte Carlo Calculations in Nuclear Medicine: Applications in Diagnostic Imaging*, Second. CRC Press.

[53] P. Andreo, 'Monte Carlo techniques in medical radiation physics', *Phys. Med. Biol.*, vol. 36, no. 7, pp. 861–920, 1991, doi: 10.1088/0031-9155/36/7/001.

[54] D. E. Raeside, 'Monte Carlo principles and applications', *Phys. Med. Biol.*, vol. 21, no. 2, pp. 181–197, 1976, doi: 10.1088/0031-9155/21/2/001.

[55] R. Y. Rubinstein, *Simulation and the Monte Carlo Method*. John Wiley & Sons, Inc., 1981.

[56] J. Perl, J. Shin, B. Faddegon, and H. Paganetti, 'TOPAS: An innovative proton Monte Carlo platform for research and clinical applications', *Med. Phys.*, vol. 39, no. 11, pp. 6818–6837, Nov. 2012, doi: 10.1118/1.4758060.

[57] I. Buvat and I. Castiglioni, 'Monte Carlo simulations in SPET and PET', *Q. J. Nucl. Med.*, vol. 46, no. 1, pp. 48–61, Mar. 2002.

[58] S. Agostinelli *et al.*, 'GEANT4 - a simulation toolkit', *Nucl. Instrum. Methods Phys. Res. Sect. Accel. Spectrometers Detect. Assoc. Equip.*, vol. 506, no. 3, pp. 250–303, Jul. 2003, doi: 10.1016/S0168-9002(03)01368-8.

[59] J. Allison *et al.*, 'Geant4 developments and applications', *IEEE Trans. Nucl. Sci.*, vol. 53, no. 1, pp. 270–278, 2006, doi: 10.1109/TNS.2006.869826.

[60] S. Jan *et al.*, 'GATE: a simulation toolkit for PET and SPECT', *Phys. Med. Biol.*, vol. 49, pp. 4543–4561, 2004, doi: 10.1088/0031-9155/49/19/007.

[61] 'TOPAS MC'. http://www.topasmc.org/ (accessed May 18, 2021).

[62] W. P. Segars, 'Development and application of the new dynamic NURBS-based cardiac-torso (NCAT) phantom', PhD, University of North Carolina at Chapel Hill, United States of America, 2001.

[63] D. Krstic and D. Nikezic, 'Input files with ORNL-mathematical phantoms of the human body for MCNP-4B', *Comput. Phys. Commun.*, vol. 176, no. 1, pp. 33–37, 2007, doi: 10.1016/j.cpc.2006.06.016.

[64] P. H. Pretorius, M. A. King, B. M. W. Tsui, K. J. LaCroix, and W. Xia, 'A mathematical model of motion of the heart for use in generating source and attenuation maps for simulating emision imaging', *Med. Phys.*, vol. 26, no. 11, pp. 2323–2332, 1999, doi: 10.1118/1.598746.

[65] W. P. Segars and B. M. W. Tsui, 'MCAT to XCAT: The Evolution of 4-D Computerized Phantoms for Imaging Research', *Proc. IEEE*, vol. 97, no. 12, pp. 1954–1968, Dec. 2009, doi: 10.1109/JPROC.2009.2022417.

[66] X. G. Xu and K. F. Eckerman, Eds., *Handbook of Anatomical Models for Radiation Dosimetry*. Taylor & Francis Group, 2010.

[67] V. J. de Melo Lima, V. F. Cassola, R. Kramer, C. A. B. de Oliveira Lira, H. J. Khoury, and J. W. Vieira, 'Development of 5- and 10-year-old pediatric phantoms based on polygon mesh surfaces', *Med. Phys.*, vol. 38, no. 8, pp. 4723–4736, 2011, doi: 10.1118/1.3615623.

[68] K. Higley *et al.*, 'Creation and application of voxelised dosimetric models, and a comparison with the current methodology as used for the International Commission on Radiological Protection's Reference Animals and Plants', *Ann. ICRP*, vol. 44, no. 1_suppl, pp. 313–330, 2015, doi: 10.1177/0146645315576097.

[69] R. McGurk, J. Seco, J. Riboldi, J. Wolfgang, W. P. Segars, and H. Paganetti, 'Extension of the NCAT phantom for the investigation of intra-fraction respiratory motion in IMRT using 4D Monte Carlo', *Phys. Med. Biol.*, vol. 55, no. 5, pp. 1475–1490, 2010, doi: 10.1088/0031-9155/55/5/014.

[70] W. P. Segars, G. Sturgeon, S. Mendonca, J. Grimes, and B. M. W. Tsui, '4D XCAT phantom for multimodality imaging research', *Med. Phys.*, vol. 37, no. 9, pp. 4902–4915, 2010, doi: 10.1118/1.3480985.

[71] W. P. Segars, B. M. W. Tsui, J. Cai, F.-F. Yin, G. S. K. Fung, and E. Samei, 'Application of the 4-D XCAT Phantoms in Biomedical Imaging and Beyond', *IEEE Trans. Med. Imaging*, vol. 37, no. 3, pp. 680–692, 2018, doi: 10.1109/TMI.2017.2738448.

[72] W. P. Segars, M. Mahesh, T. J. Beck, E. C. Frey, and B. M. W. Tsui, 'Realistic CT simulation using the 4D XCAT phantom', *Med. Phys.*, vol. 35, no. 8, pp. 3800–3808, 2008, doi: 10.1118/1.2955743.

[73] A. G. Webb, 'General Image Characteristics', in *Introduction to Biomedical Imaging*, 1st ed., Wiley-IEEE Press, 2003, pp. 220–232. [Online]. Available: https://ieeexplore-ieee-org.ezproxy.canterbury.ac.nz/servlet/opac?bknumber=5273528

[74] J. A. Thorley, J. Pike, and J. Z. Rappoprt, 'Super-resolution Microscopy: A comparison of commercially available options', in *Fluorescence Microscopy: Super-resolution and other novel techniques*, Elsevier B.V., 2014, p. 260.

[75] A. B. Wolbarst, P. Capasso, and A. R. Wyant, 'Image Quality and Dose: What Constitutes a "Good" Medical Image?', in *Medical Imaging: Essentials for Physicians*, 1st ed., John Wiley & Sons, Inc., 2013, p. 435.

[76] A. Rose, *Vision: human and electronic*. Plenum Press, 1973.

[77] E. Samei *et al.*, 'Assessment of display performance for medical imaging systems: Executive summary of AAPM TG18 report', *Med. Phys.*, vol. 32, no. 4, pp. 1205–1225, 2005, doi: 10.1118/1.1861159.

[78] OpenGATE Collaboration, 'GATE'. https://gate.uca.fr/#/admin (accessed Feb. 17, 2021).

[79] D. Sarrut, 'update spect', *GiLab*, 2019. https://gitlab.in2p3.fr/davidsarrut/gate-exercices/-/tree/master/spect/mac (accessed Apr. 29, 2020).

[80] 'Symbia TruePoint SPECT.CT System Specifications'. Siemens Medical Solutions, 2005.

[81] J. P. Islamian, M. T. Bahreyni Toossi, M. Momennezhad, S. R. Zakavi, R. Sadeghi, and M. Ljungberg, 'Monte Carlo Study of the Effect of Collimator Thickness on Tc-99m Source Response in Single Photon Emission Computer Tomography', *World J. Nucl. Med.*, vol. 11, no. 2, pp. 70–74, 2012, doi: 10.4103/1450-1147.103419.

[82] 'Physics Reference Manual: Release 10.4'. Geant4 Collaboration. Accessed: Jun. 14, 2021. [Online]. Available: https://indico.cern.ch/event/679723/contributions/2792554/attachments/1559217/2454299/PhysicsReferenceManual.pdf

[83] *Rhinoceros*. Robert McNeel & Associates, 2020. [Online]. Available: https://www.rhino3d.com/

[84] ICRP, 'Radiation Dose to Patients from Radiopharmaceuticals: a Compendium of Current Information Related to Frequently Used Substances', ICRP Publication 128, 2014.

[85] R. Nall, 'How Much Blood Is in Your Body and How Much You Can Lose', *healthline*, Jul. 18, 2017. https://www.healthline.com/health/how-much-blood-in-human-body (accessed Jun. 04, 2021).

[86] T. Ole, *GNU Parallel 20200622 ('Floyd')*. 2020. [Online]. Available: https://doi.org/10.5281/zenodo.3903853

[87] F. P. Trub, J. C. Wells, F. J. Ruhli, K. Staub, and J. Floris, 'Filling the weight gap: Estimating body weight & BMI using height, chest & upper arm circumference of Swiss conscripts in the first half of the 20th century', *Econ. Hum. Biol.*, vol. 38, 2020, doi: 10.1016/j.ehb.2020.100891.

[88] 'DICOM Conformance Statement: syngo MI Applications VB21'. Siemens Medical Solutions, Jan. 2018. Accessed: Jun. 14, 2021. [Online]. Available: https://cdn0.scrvt.com/39b415fb07de4d9656c7b516d8e2d907/1800000004690339/a6ed53c811dd/dcs_syngo_mi_apps_vb21-04690339_1800000004690339.pdf

[89] 'PS3.5: DICOM PS3.5 2021b - Data Structures and Encoding'. NEMA, 2021. Accessed: Jun. 14, 2021. [Online]. Available: http://dicom.nema.org/medical/dicom/current/output/pdf/part05.pdf

[90] X. He, E. C. Frey, J. M. Links, K. L. Gilland, W. P. Segars, and B. M. W. Tsui, 'A Mathematical Observer study for the evaluation and optimization of compensation methods for myocardial SPECT using a phantom population that realistically models patient variability', *IEEE Trans. Nucl. Sci.*, vol. 51, no. 1, pp. 218–224, 2004, doi: 10.1109/TNS.2004.823331.

[91] A. Cheung, Y. Zhou, T. L. Faber, E. V. Garcia, L. Zhu, and J. Chen, 'The performance of phase analysis of gated SPECT myocardial perfusion imaging in the presence of perfusion defects: A simulation study', *J. Nucl. Cardiol.*, vol. 19, no. 3, pp. 500–506, 2011, doi: 10.1007/s12350-011-9494-5.

[92] T. Hosny, M. M. Khalil, A. A. Elfiky, and W. M. Elshemey, 'Image quality characteristics of myocardial perfusion SPECT imaging using state-of-the-art cmmercial software algorithms: evaluation of 10 reconstruction methods', *Am. J. Nucl. Med. Mol. Imaging*, vol. 10, no. 6, pp. 375–386, 2020.

[93] W. Rasband, *ImageJ*. United States of America: National Institutes of Health. [Online]. Available: http://imagej.nih.gov/ij

[94] *Vernier Graphical Analysis*. 2011. [Online]. Available: http://www.vernier.com

[95] D. R. Dance, S. Christofides, A. D. A. Maidment, I. D. McLean, and K. H. Ng, Eds., *Diagnostic Radiology Physics: A Handbook for Teachers and Students*. IAEA, 2014.

Appendix A

Gate macros for each section of the simulation.

runParallel.sh

```
#!/bin/bash
cmd="parallel ~/spectCATv2.0/runSim.sh --projAngles {1} --index {2} -j37 '>' {2}.log';' rm {2}.log ::: 52.00 49.19 46.38 43.57 40.76 37.95 35.14 32.32 29.51 26.70 23.86 21.08 18.27 15.46 12.65 9.84 7.03 4.22 1.41 -1.41 -4.22 -7.03 -9.84 -12.65 -15.46 -18.27 -21.08 -23.89 -26.70 -29.51 -32.32 -35.14 -37.95 -40.76 -43.57 -46.38 -49.19 :::+ 0 1 2 3 4 5 6 7 8 9 10 11 12 13 14 15 16 17 18 19 20 21 22 23 24 25 26 27 28 29 30 31 32 33 34 35 36"
eval $cmd
```

runSim.sh

```
#!/bin/bash
# Gate will decay the source during projection acquisition but this script need to calulate activity at
# start of each projection.

A0=5.669 #MBq - activity at start of projAngle[0]
headSeparation=104.0  #deg - Total angular separation for all heads
radius=29 #cm Distance from COR to front of camera

timePerProjection=25 #seconds
Thalf=21600 #seconds - 6 hrs
lambda=$(bc -l <<< "l(2)/$Thalf")

projAngles=${2:?Missing argument}
index=${4:?Missing argument} #time index (number of projections that have completed)

time=$(bc -l <<< "$index*$timePerProjection")
decay=$(bc -l <<< "e(-$lambda*$time)")
A=$(bc -l <<< "$A0*$decay")
cmd="Gate mac/main.mac -a [HEAD_SEPARATION,$headSeparation][RADIUS,$radius][ANGLE,$projAngles][PROJTIME,$timePerProjection][ACTIVITY,$A][TIME,$time]"
echo $cmd
eval $cmd

echo "Finished"
```

main.mac

```
# Verbose
/control/execute mac/verbose.mac

# Visu
#/control/execute mac/visu.mac

# ------------------------------------------------
# GEOMETRY
# ------------------------------------------------
# Geometry world
# Material Database
/gate/geometry/setMaterialDatabase data/GateMaterials.db

/control/alias COLL_X 266
/control/alias COLL_Y 354

# World
/gate/world/geometry/setXLength 1.5 m
/gate/world/geometry/setYLength 2.5 m
/gate/world/geometry/setZLength 1.5 m
/gate/world/vis/setColor white
/gate/world/vis/forceWireframe
/gate/world/setMaterial Air

# Geometry SPECT
/control/execute mac/spect_head_update.mac
/control/execute mac/spect_collimator_lehr_update.mac
/control/execute mac/spect_digitizer_Tc99m.mac

# Translation is according to collimator type and radius
# The following lines compute the correct position of the head volume for this
# collimator (PSD_position is defined in spect_head)
/control/add TRANSLATION {RADIUS} {PSD_position}
/control/multiply TRANSLATION {TRANSLATION} -1
/gate/SPECThead/placement/setTranslation 0. 0. {TRANSLATION}  cm

/control/execute mac/additionalHeads.mac

# Import patient
/control/execute mac/patientAnatomy.mac

/control/listAlias

# ------------------------------------------------
# PHYSICS
# ------------------------------------------------

/gate/physics/addPhysicsList emstandard_opt3
```

```
/gate/physics/addProcess RadioactiveDecay

/gate/physics/Gamma/SetCutInRegion      world 1 km
/gate/physics/Electron/SetCutInRegion   world 1 km
/gate/physics/Positron/SetCutInRegion   world 1 km

/gate/physics/Gamma/SetCutInRegion      body 1 mm
/gate/physics/Electron/SetCutInRegion   body 1 mm
/gate/physics/Positron/SetCutInRegion   body 1 mm

/gate/physics/Gamma/SetCutInRegion      SPECThead 0.1 mm
/gate/physics/Electron/SetCutInRegion   SPECThead 1 mm
/gate/physics/Positron/SetCutInRegion   SPECThead 1 mm

# ------------------------------------------
# OUTPUT
# ------------------------------------------
# Save particles stats
/gate/actor/addActor              SimulationStatisticActor stat
/gate/actor/stat/save            output/stats{ANGLE}.txt
/gate/actor/stat/saveEveryNSeconds 20

# Image output
# output projection will contains 3 slices:
# slice 1: all counts
# slice 2: scatter window
# slice 3: peak 140keV window
/gate/output/projection/enable
/gate/output/projection/setFileName output/projection{ANGLE}
/gate/output/projection/addInputDataName scatter
/gate/output/projection/addInputDataName peak140

/gate/output/projection/pixelSizeX 6.5913400650024 mm
/gate/output/projection/pixelSizeY 6.5913400650024 mm
/gate/output/projection/pixelNumberX 64
/gate/output/projection/pixelNumberY 64
/gate/output/projection/projectionPlane XY

# ------------------------------------------
# INIT
# ------------------------------------------
# Initialize
/gate/run/initialize

# ------------------------------------------
# SOURCE
# ------------------------------------------
/control/execute mac/PhS_heartSource.mac    #<--------Requires heart geometry exists

# ------------------------------------------
# START
```

```
# ------------------------------------------

# Random
/gate/random/setEngineName MersenneTwister
/gate/random/setEngineSeed auto

# Go
/gate/application/setTimeStart 0 s
/gate/application/setTimeSlice {PROJTIME} s
/gate/application/setTimeStop  {PROJTIME} s

/gate/application/startDAQ
```

spect_head_update.mac

```
# SPECT Head: main volume, everything is included in SPECThead
# the name MUST be SPECThead
/gate/world/daughters/name SPECThead
/gate/world/daughters/insert box
/gate/SPECThead/geometry/setXLength 68.5 cm
/gate/SPECThead/geometry/setYLength 53.9 cm
/gate/SPECThead/geometry/setZLength 13.9675 cm
/gate/SPECThead/vis/setColor white
/gate/SPECThead/setMaterial Air
/gate/SPECThead/vis/forceWireframe

# Shielding: main volume
/gate/SPECThead/daughters/name shielding
/gate/SPECThead/daughters/insert box
/gate/shielding/geometry/setXLength 68.5 cm
/gate/shielding/geometry/setYLength 53.9 cm
/gate/shielding/geometry/setZLength 10.5 cm
/gate/shielding/placement/setTranslation 0. 0. -1.73375 cm
/gate/shielding/setMaterial Steel
/gate/shielding/vis/setColor red
/gate/shielding/vis/forceWireframe

# Shielding: first layer of the lead cover
/gate/shielding/daughters/name shielding_lead_cover
/gate/shielding/daughters/insert box
/gate/shielding_lead_cover/geometry/setXLength 61.64 cm
/gate/shielding_lead_cover/geometry/setYLength 47.0 cm
/gate/shielding_lead_cover/geometry/setZLength  9.5 cm
/gate/shielding_lead_cover/placement/setTranslation 0. 0. 0.5 cm
/gate/shielding_lead_cover/setMaterial Lead
/gate/shielding_lead_cover/vis/forceWireframe

# Shielding: Aluminium Cover
/gate/shielding_lead_cover/daughters/name shielding_aluminium_cover
/gate/shielding_lead_cover/daughters/insert box
```

```
/gate/shielding_aluminium_cover/geometry/setXLength 61.64 cm
/gate/shielding_aluminium_cover/geometry/setYLength 47.04 cm
/gate/shielding_aluminium_cover/geometry/setZLength 0.13 cm
/gate/shielding_aluminium_cover/placement/setTranslation 0. 0. 4.685 cm
/gate/shielding_aluminium_cover/setMaterial Aluminium
/gate/shielding_aluminium_cover/vis/setColor blue
/gate/shielding_aluminium_cover/vis/forceWireframe

# Shielding: reflector TiO2
/gate/shielding_lead_cover/daughters/name shielding_reflector
/gate/shielding_lead_cover/daughters/insert box
/gate/shielding_reflector/geometry/setXLength 61.64 cm
/gate/shielding_reflector/geometry/setYLength 47.04 cm
/gate/shielding_reflector/geometry/setZLength  0.12 cm
/gate/shielding_reflector/placement/setTranslation 0. 0. 3.61 cm
/gate/shielding_reflector/setMaterial TiO2
/gate/shielding_reflector/vis/setColor blue
/gate/shielding_reflector/vis/forceWireframe

# Shielding: crystal
/gate/shielding_lead_cover/daughters/name crystal_volume
/gate/shielding_lead_cover/daughters/insert box
/gate/crystal_volume/geometry/setXLength 59.1 cm
/gate/crystal_volume/geometry/setYLength 44.5 cm
/gate/crystal_volume/geometry/setZLength  0.95 cm
/gate/crystal_volume/placement/setTranslation  0 0 4.145 cm
/gate/crystal_volume/setMaterial NaITl
/gate/crystal_volume/vis/setColor yellow
# special command to say that this volume is the crystal
/gate/systems/SPECThead/crystal/attach crystal_volume
# This is needed !
/gate/crystal_volume/attachCrystalSD

# Shielding: Backside
# The back-side is fairly complex, and may have a strong influence on the
# spectrum: the model shown here is simplified
/gate/shielding_lead_cover/daughters/name shielding_backside
/gate/shielding_lead_cover/daughters/insert box
/gate/shielding_backside/geometry/setXLength 61.64 cm
/gate/shielding_backside/geometry/setYLength 47.04 cm
/gate/shielding_backside/geometry/setZLength  8. cm
/gate/shielding_backside/placement/setTranslation 0. 0. -0.45 cm
/gate/shielding_backside/setMaterial Pyrex66
```

spect_collimator_lehr_update.mac

```
# Holes are regular hexagons
# Holes length     : 24.05   mm
# Holes diam       : 1.11    mm
# Septal thickness : 0.16  mm

# The PSD_position is determined as the lowest coordinate of the PSD volume in
# the head box. It is used later to compute the head position
/control/alias PSD_position 6.6025

# Collimator: main volume
/gate/SPECThead/daughters/name collimator
/gate/SPECThead/daughters/insert box
/gate/collimator/geometry/setXLength 68.5 cm
/gate/collimator/geometry/setYLength 53.9 cm
/gate/collimator/geometry/setZLength 3.085 cm
/gate/collimator/setMaterial Air
/gate/collimator/attachPhantomSD
/gate/collimator/placement/setTranslation 0. 0. 5.06 cm
/gate/collimator/vis/setColor red
/gate/collimator/vis/forceWireframe

# Collimator: aluminum PSD (Position Sensitive Detection)
/gate/collimator/daughters/name aluminiumPSD
/gate/collimator/daughters/insert box
/gate/aluminiumPSD/geometry/setXLength 59.7 cm
/gate/aluminiumPSD/geometry/setYLength 45.1 cm
/gate/aluminiumPSD/geometry/setZLength 0.1 cm
/gate/aluminiumPSD/placement/setTranslation 0. 0. 1.4925 cm
/gate/aluminiumPSD/setMaterial Aluminium
/gate/aluminiumPSD/vis/setColor green
/gate/aluminiumPSD/vis/forceWireframe

# Collimator: PVC layer
/gate/collimator/daughters/name collimator_pvc_layer
/gate/collimator/daughters/insert box
/gate/collimator_pvc_layer/geometry/setXLength 59.7 cm
/gate/collimator_pvc_layer/geometry/setYLength 45.1 cm
/gate/collimator_pvc_layer/geometry/setZLength 0.15 cm
/gate/collimator_pvc_layer/placement/setTranslation 0. 0. 1.3675 cm
/gate/collimator_pvc_layer/setMaterial PVC
/gate/collimator_pvc_layer/vis/setColor red
/gate/collimator_pvc_layer/vis/forceWireframe

# Collimator: air gap
/gate/collimator/daughters/name collimator_air_gap
/gate/collimator/daughters/insert box
/gate/collimator_air_gap/geometry/setXLength 59.7 cm
/gate/collimator_air_gap/geometry/setYLength 45.1 cm
```

```
/gate/collimator_air_gap/geometry/setZLength 0.38 cm
/gate/collimator_air_gap/placement/setTranslation 0. 0. 1.1025 cm
/gate/collimator_air_gap/setMaterial Air
/gate/collimator_air_gap/vis/setColor blue
/gate/collimator_air_gap/vis/forceWireframe

# Collimator: core
/gate/collimator/daughters/name collimator_core
/gate/collimator/daughters/insert box
/gate/collimator_core/geometry/setXLength 59.7 cm
/gate/collimator_core/geometry/setYLength 45.1 cm
/gate/collimator_core/geometry/setZLength 2.405 cm
/gate/collimator_core/placement/setTranslation 0. 0. -0.29 cm
/gate/collimator_core/setMaterial Lead
/gate/collimator_core/vis/setColor blue
/gate/collimator_core/vis/forceWireframe

# Collimator: holes
# Insert a first hole
/gate/collimator_core/daughters/name collimator_hole
/gate/collimator_core/daughters/insert hexagone
/gate/collimator_hole/geometry/setHeight 2.405 cm
/gate/collimator_hole/geometry/setRadius 0.0555 cm
/gate/collimator_hole/setMaterial Air

# Repeat the first hole in an array
/gate/collimator_hole/repeaters/insert cubicArray
/gate/collimator_hole/cubicArray/setRepeatNumberX {COLL_X}
/gate/collimator_hole/cubicArray/setRepeatNumberY {COLL_Y}
/gate/collimator_hole/cubicArray/setRepeatNumberZ 1
/gate/collimator_hole/cubicArray/setRepeatVector 2.24 1.27 0. mm

# Repeat these holes in a linear array
/gate/collimator_hole/repeaters/insert linear
/gate/collimator_hole/linear/setRepeatNumber 2
/gate/collimator_hole/linear/setRepeatVector  1.12 0.635 0. mm

# Collimator: aluminum cover 2
/gate/collimator/daughters/name collimator_aluminium_cover2
/gate/collimator/daughters/insert box
/gate/collimator_aluminium_cover2/geometry/setXLength 59.7 cm
/gate/collimator_aluminium_cover2/geometry/setYLength 45.1 cm
/gate/collimator_aluminium_cover2/geometry/setZLength 0.05 cm
/gate/collimator_aluminium_cover2/placement/setTranslation 0. 0. -1.5175 cm
/gate/collimator_aluminium_cover2/setMaterial Aluminium
/gate/collimator_aluminium_cover2/vis/setColor blue
/gate/collimator_aluminium_cover2/vis/forceWireframe
```

spect_digitizer_Tc99m.mac

```
# Digitizer for Technitium 99m
# Adder
/gate/digitizer/Singles/insert adder

# Readout
/gate/digitizer/Singles/insert readout
/gate/digitizer/Singles/readout/setDepth 1

# Intrinsic Spatial Blurring
/gate/digitizer/Singles/insert spblurring
/gate/digitizer/Singles/spblurring/setSpresolution 5.106 mm   #3.97 mm
/gate/digitizer/Singles/spblurring/verbose 0

# Energy Blurring
/gate/digitizer/Singles/insert blurring
/gate/digitizer/Singles/blurring/setLaw inverseSquare
/gate/digitizer/Singles/blurring/inverseSquare/setResolution 0.095
/gate/digitizer/Singles/blurring/inverseSquare/setEnergyOfReference 140.0 keV

# Thresholds Tc99m
/gate/digitizer/Singles/insert thresholder
/gate/digitizer/Singles/thresholder/setThreshold 108.5 keV
/gate/digitizer/Singles/insert upholder
/gate/digitizer/Singles/upholder/setUphold 150.5 keV

# Scatter Windows
/gate/digitizer/name scatter
/gate/digitizer/insert singleChain
/gate/digitizer/scatter/setInputName Singles
/gate/digitizer/scatter/insert thresholder
/gate/digitizer/scatter/thresholder/setThreshold 108.5 keV
/gate/digitizer/scatter/insert upholder
/gate/digitizer/scatter/upholder/setUphold 129.5 keV

# Tc-99m : 140 keV windows, width of 20%
/gate/digitizer/name peak140
/gate/digitizer/insert singleChain
/gate/digitizer/peak140/setInputName Singles
/gate/digitizer/peak140/insert thresholder
/gate/digitizer/peak140/thresholder/setThreshold 129.5 keV
/gate/digitizer/peak140/insert upholder
/gate/digitizer/peak140/upholder/setUphold 150.5 keV

# Dead time -> no dead time simulated here
/gate/digitizer/Singles/insert deadtime
/gate/digitizer/Singles/deadtime/setDeadTime 1650 ns
/gate/digitizer/Singles/deadtime/setMode paralysable
/gate/digitizer/Singles/deadtime/chooseDTVolume crystal_volume
```

patientAnatomy.mac

```
## ---IMPORT BODY STL FILE FOR PHANTOM (Phantom Scale 1.0 as Example)
/gate/world/daughters/name body
/gate/world/daughters/insert tessellated
/gate/body/geometry/setPathToSTLFile data/patientData/STLFiles/MaleScale1.0_BodyShort.stl
/gate/body/setMaterial       Body

# ---IMPORT STL FOR HEART AND OTHER ORGRANS AND POSITION IN BODY
/gate/body/daughters/name peri
/gate/body/daughters/insert tessellated
/gate/peri/geometry/setPathToSTLFile data/patientData/STLFiles/MaleScale1.0_HeartOuter.stl
/gate/peri/setMaterial      Heart

/gate/body/daughters/name lung
/gate/body/daughters/insert tessellated
/gate/lung/geometry/setPathToSTLFile data/patientData/STLFiles/MaleScale1.0_Lung.stl
/gate/lung/setMaterial Lung

/gate/body/daughters/name liver
/gate/body/daughters/insert tessellated
/gate/liver/geometry/setPathToSTLFile data/patientData/STLFiles/MaleScale1.0_Liver.stl
/gate/liver/setMaterial Liver

/gate/body/daughters/name bone
/gate/body/daughters/insert tessellated
/gate/bone/geometry/setPathToSTLFile data/patientData/STLFiles/MaleScale1.0_Bones.stl
/gate/bone/setMaterial RibBone

/gate/body/daughters/name kidney
/gate/body/daughters/insert tessellated
/gate/kidney/geometry/setPathToSTLFile data/patientData/STLFiles/MaleScale1.0_Kidney.stl
/gate/kidney/setMaterial Kidney

/gate/body/daughters/name stomach
/gate/body/daughters/insert tessellated
/gate/stomach/geometry/setPathToSTLFile data/patientData/STLFiles/MaleScale1.0_Stomach.stl
/gate/stomach/setMaterial Intestine

/gate/body/daughters/name intestine
/gate/body/daughters/insert tessellated
/gate/intestine/geometry/setPathToSTLFile data/patientData/STLFiles/MaleScale1.0_Intestines.stl
/gate/intestine/setMaterial Intestine

/gate/body/daughters/name muscles
/gate/body/daughters/insert tessellated
/gate/muscles/geometry/setPathToSTLFile data/patientData/STLFiles/MaleScale1.0_Muscle.stl
/gate/muscles/setMaterial Muscle

/gate/body/daughters/name brain
```

```
/gate/body/daughters/insert tessellated
/gate/brain/geometry/setPathToSTLFile data/patientData/STLFiles/MaleScale1.0_Brain.stl
/gate/brain/setMaterial Brain

# ---Rotate body to align with couch
/gate/body/placement/setRotationAxis  1 0 0
/gate/body/placement/setRotationAngle -90 deg
```

PhS_heartSource.mac

```
# Make the heart source of activity
# Requires heart anatomy is already present
/gate/source/addSource src_Heart phaseSpace
/gate/source/src_Heart/addPhaseSpaceFile data/PhSData/PhS-Gamma-MaleAverage_Peri-20MBq.root
/gate/source/src_Heart/attachTo peri
/gate/source/src_Heart/setForcedHalfLife  21624.12 s  #6.0 hrs
/gate/source/src_Heart/setForcedUnstableFlag true
/gate/source/src_Heart/setActivity {ACTIVITY} MBq
```

Appendix B

Python Code: Convert GATE Output to Sinograms

```
import numpy as np
from PIL import Image

i = ['projection0.sin', 'projection25.sin', 'projection50.sin', 'projection75.sin', 'projection100.sin',
'projection125.sin', 'projection150.sin', 'projection175.sin', 'projection200.sin', 'projection225.sin',
'projection250.sin', 'projection275.sin', 'projection300.sin', 'projection325.sin', 'projection350.sin',
'projection375.sin', 'projection400.sin', 'projection425.sin', 'projection450.sin', 'projection475.sin',
'projection500.sin', 'projection525.sin', 'projection550.sin', 'projection575.sin', 'projection600.sin',
'projection625.sin', 'projection650.sin', 'projection675.sin', 'projection700.sin', 'projection725.sin',
'projection750.sin', 'projection775.sin', 'projection800.sin', 'projection825.sin', 'projection850.sin',
'projection875.sin', 'projection900.sin']   #GATE simulation output

C = np.empty((74,64,64), np.uint16)   #empty matrix matching final dimensions of image data

print("Let's go!")
print("... Camera One...")  #data relating to Detector 1
for j in i:
   k = i.index(j)  #select which .sin image to open
   A = np.fromfile(j, dtype=np.uint16)    #open .sin image as unsigned 16 bit
   A = A.reshape(6,64,64)  #reshape into matrix
   x = 4   # select which slice of the matrix to take, relating to first detector peak window
   B = A[x,:,:]
   B = np.rot90(B,k=2,axes=(0,1))  #rotate image 180 deg to match hospital orientation
   d = k   #index of final matrix to place image slice
   C[d] = B    #place image slice in correct location in the matrix
   print("%s Done!" % k)

print("... Camera Two...")  #data relating to Detector 2
for j in i:
   k = i.index(j)  #select which .sin image to open
   A = np.fromfile(j, dtype=np.uint16)    #open .sin image as unsigned 16 bit
   A = A.reshape(6,64,64)  #reshape into matrix
   x = 5   # select which slice of the matrix to take, relating to second detector peak window
   B = A[x,:,:]
   B = np.rot90(B,k=2,axes=(0,1))  #rotate image 180 deg to match hospital orientation
   d = k + 37  #index of final matrix to place image slice
   C[d] = B    #place image slice in correct location in the matrix
   print("%s Done!" % k)

print("... Making Sinograms....")
image_row = list(range(0,64))   # number of rows in image
stack = list(range(0,74))   #number of images in stack C
```

```
for row in image_row:   #for every row of pixels in the image
   S = C[:,row]
   S_Im = Image.fromarray(S)
   rot_im = S_Im.rotate(90, expand=True)
   filename = "%s_rotated.png" % row  #name sinogram of each row
   rot_im.save(filename)  #save
   print("%s Done!" % row)

print("Finished!")
```

Matlab Code: Reconstruct Sinograms using FBP

```
slice = [1:63];

theta = [52.00, 49.19, 46.38, 43.57, 40.76, 37.95, 35.14, 32.32, 29.51, 26.70, 23.86, 21.08, 18.27, 15.46,
12.65, 9.84, 7.03, 4.22, 1.41, -1.41, -4.22, -7.03, -9.84, -12.65, -15.46, -18.27, -21.08, -23.89, -26.70, -
29.51, -32.32, -35.14, -40.76, -43.57, -46.38, -49.19, -52.00, -54.81, -57.62, -57.62, -60.43, -63.24, -
66.05, -68.86, -71.68, -74.49, -77.30, -80.11, -82.92, -85.73, -88.54, -91.35, -94.16, -96.97, -99.78, -
102.59, -105.41, -108.22, -111.03, -113.84, -116.65, -119.46, -122.27, -125.08, -127.89, -130.70, -
133.51, -136.32, -139.14, -141.95, -144.76, -147.57, -150.38, -153.19];
M = [];
for i = 1:length(slice)
   j = slice(i);
   title = [num2str(j),'_rotated.png'];
   img = imread(title);
   title2 = [num2str(j), '_reconstructed_MATLAB.png'];
   Test = iradon(img, theta, 'Hann');

   %figure, imshow(Test, [])
   M = cat(3,M,Test);
end

%sliceViewer(M, 'SliceDirection',[1 0 0])   %view along X axis
%sliceViewer(M, 'SliceDirection',[0 0 1])   %view along Z axis (default)
```

Appendix C

Python Script Converting GATE Output to DICOM

```
import numpy as np
from pydicom import dcmread

i = ['projection0.sin', 'projection25.sin', 'projection50.sin', 'projection75.sin', 'projection100.sin',
'projection125.sin', 'projection150.sin', 'projection175.sin', 'projection200.sin', 'projection225.sin',
'projection250.sin', 'projection275.sin', 'projection300.sin', 'projection325.sin', 'projection350.sin',
'projection375.sin', 'projection400.sin', 'projection425.sin', 'projection450.sin', 'projection475.sin',
'projection500.sin', 'projection525.sin', 'projection550.sin', 'projection575.sin', 'projection600.sin',
'projection625.sin', 'projection650.sin', 'projection675.sin', 'projection700.sin', 'projection725.sin',
'projection750.sin', 'projection775.sin', 'projection800.sin', 'projection825.sin', 'projection850.sin',
'projection875.sin', 'projection900.sin']   #GATE simulation output
C = np.empty((148,64,64), np.uint16)   #empty matrix matching final dimensions of image data
print("Let's go!")
print("... Camera One...")  #data relating to Detector 1
for j in i:
   k = i.index(j)  #select which .sin image to open
   A = np.fromfile(j, dtype=np.uint16)    #open .sin image as unsigned 16 bit
   A = A.reshape(6,64,64)  #reshape into matrix
   x = 4   # select which slice of the matrix to take, relating to first detector peak window
   B = A[x,:,:]
   B = np.rot90(B,k=2,axes=(0,1))  #rotate image 180 deg to match hospital orientation
   d = k   #index of final matrix to place image slice
   C[d] = B    #place image slice in correct location in the matrix
   print("%s Done!" % k)

print("... Camera Two...")  #data relating to Detector 2
for j in i:
   k = i.index(j)  #select which .sin image to open
   A = np.fromfile(j, dtype=np.uint16)    #open .sin image as unsigned 16 bit
   A = A.reshape(6,64,64)  #reshape into matrix
   x = 5   # select which slice of the matrix to take, relating to second detector peak window
   B = A[x,:,:]
   B = np.rot90(B,k=2,axes=(0,1))  #rotate image 180 deg to match hospital orientation
   d = k + 37  #index of final matrix to place image slice
   C[d] = B    #place image slice in correct location in the matrix
   print("%s Done!" % k)

print("... Camera One Scatter...")
for j in i:
   k = i.index(j)  #select which .sin image to open
   A = np.fromfile(j, dtype=np.uint16)    #open .sin image as unsigned 16 bit
   A = A.reshape(6,64,64)  #reshape into matrix
```

```
    x = 2   # select which slice of the matrix to take, relating to first detector scatter window
    B = A[x,:,:]
    B = np.rot90(B,k=2,axes=(0,1))  #rotate image 180 deg to match hospital orientation
    d = k + 74 #index of final matrix to place image slice
    C[d] = B     #place image slice in correct location in the matrix
    print("%s Done!" % k)

print("... Camera Two Scatter...")
for j in i:
    k = i.index(j)  #select which .sin image to open
    A = np.fromfile(j, dtype=np.uint16)     #open .sin image as unsigned 16 bit
    A = A.reshape(6,64,64) #reshape into matrix
    x = 3   # select which slice of the matrix to take, relating to second detector scatter window
    B = A[x,:,:]
    B = np.rot90(B,k=2,axes=(0,1))  #rotate image 180 deg to match hospital orientation
    d = k + 111     #index of final matrix to place image slice
    C[d] = B     #place image slice in correct location in the matrix
    print("%s Done!" % k)

print("... Making DICOM....")
filename                                                                                                =
"CARDIAC_PHANTOM.NM.MYOCARDIAL_PERFUSION.1000.0001.2020.10.12.16.21.54.145474.12415
6143.IMA"     #sample file with correct header information
ds = dcmread(filename)

ds.PixelData = C    #matrix with image data

m = ds.DetectorInformationSequence[0]   #correcting ROR for detector One (mm)
m[0x0018,0x1142].value = [250, 250, 250, 250, 250, 250, 250, 250, 250, 250, 250, 250, 250, 250, 250,
250, 250, 250, 250, 250, 250, 250, 250, 250, 250, 250, 250, 250, 250, 250, 250, 250, 250, 250, 250,
250]

n = ds.DetectorInformationSequence[1]   #correcting ROR for detector Two (mm)
n[0x0018,0x1142].value = [250, 250, 250, 250, 250, 250, 250, 250, 250, 250, 250, 250, 250, 250, 250,
250, 250, 250, 250, 250, 250, 250, 250, 250, 250, 250, 250, 250, 250, 250, 250, 250, 250, 250, 250,
250]

p = ds.RotationInformationSequence[0]   #correcting ROR (mm)
p[0x0018,0x1142].value = [250, 250, 250, 250, 250, 250, 250, 250, 250, 250, 250, 250, 250, 250, 250,
250, 250, 250, 250, 250, 250, 250, 250, 250, 250, 250, 250, 250, 250, 250, 250, 250, 250, 250, 250,
250]

ds.save_as("MaleScale1.0.IMA")  #combine image data with header file as new file
print("Finished!")
```

Appendix D

Counts within each ROI, as recorded in ImageJ.

Lesion Free Images

Reconstruction Method	Threshold	ROI Size (Pixels)		
		Myo	Vent	Bkgd
FBP	7006	101	13	15
Flash3D-AC	2980	88	18	15
Flash3D-NoAC	8924	87	18	15

Table 9: Mean counts per pixel for a central slice of the Syngo FBP reconstruction of each scale of phantom.

Scale	Myocardium	SD	Ventricle	SD	Background	SD
1.0	13819.0	3929.7	5311.3	776.8	8.0	26.0
1.2	8729.4	2258.7	4522.9	1253.4	28.1	75.2
1.4	5831.0	1542.3	2972.5	629.2	52.8	87.0
1.6	35985	8130	22848	4942	925.0	801
1.8	23378	4998	17598	2314	129.0	209

Table 10: Mean counts per pixel for a central slice of the Flash3D-AC reconstruction of each scale of phantom.

Scale	Myocardium	SD	Ventricle	SD	Background	SD
1.0	5169.5	1188.6	1883.6	468.7	17.0	13.0
1.2	5431.5	1326.3	2391.1	919.6	64.0	64.5
1.4	5064.1	1294.1	2208.6	783.3	90.7	48.9
1.6	31829	8374	15641	5699	1321	967
1.8	18133	4487	9092	2962	581	739

Table 11: Mean counts per pixel for a central slice of the Flash3D-NoAC reconstruction of each scale of phantom.

Scale	Myocardium	SD	Ventricle	SD	Background	SD
1.0	14974.8	3855.5	5458.5	1760.7	216.5	100.5
1.2	9510.6	2255.1	4482.3	1391.4	270.1	79.7
1.4	6289.8	1326.1	3523.0	1091.7	294.4	132.9
1.6	38165	7672	23091	7160	3115	914
1.8	24334	4370	15347	3163	1058	709

Lesion Present Images

Reconstruction Method	Threshold	ROI Size (Pixels)			
		Myo	Vent	Lesion	Bkgd
FBP	8928	58	14	18	15
Flash3D-AC	2879	55	14	18	15
Flash3D-NoAC	10382	50	14	18	15

Table 12: Mean counts per pixel for a central slice of the Syngo FBP reconstruction of each scale of phantom with a lesion included.

Scale	Myocardium	SD	Ventricle	SD	Lesion	SD	Background	SD
1.0	15188.7	3812.6	5407.3	1094.8	5172.7	1675.8	247.8	299.3
1.2	9449.5	2723.8	3539.9	812.7	1954.6	1579.3	137.9	218.8
1.4	6055.1	1375.5	4160.1	1261.6	1306.5	1097.7	80.2	111.4
1.6	36556	9635	25676	6692	12934	8530	468	612
1.8	26659	6332	15270	2318	10376	5216	828	319

Table 13: Mean counts per pixel for a central slice of the Flash3D-AC reconstruction of each scale of phantom with a lesion included.

Scale	Myocardium	SD	Ventricle	SD	Lesion	SD	Background	SD
1.0	4945.1	1373.1	1886.5	490.8	2027.0	769.3	19.8	16.1
1.2	5466.6	1456.1	2477.9	686.7	2713.3	1155.5	62.9	39.0
1.4	4827.6	1269.0	2047.4	440.7	1858.5	973.2	136.9	96.2
1.6	33051	9302	18400	5703	12978	9036	925	728
1.8	20803	7004	9937	2948	7783	4163	630	547

Table 14: Mean counts per pixel for a central slice of the Flash3D-NoAC reconstruction of each scale of phantom with a lesion included.

Scale	Myocardium	SD	Ventricle	SD	Lesion	SD	Background	SD
1.0	15954.2	3616.8	5680.1	2073.3	7367.9	2003.7	287.7	168.1
1.2	10153.0	2457.5	4585.9	1816.3	1653.3	1320.8	408.9	239.8
1.4	6236.3	1443.4	3710.4	1611.2	1690.2	1153.4	283.8	94.3
1.6	3852.0	1235.4	2545.5	791.9	1314.8	920.2	133.6	59.5
1.8	27652	7842	18022	3037	6539	4295	686	322

Appendix E

Myocardial Counts Comparison

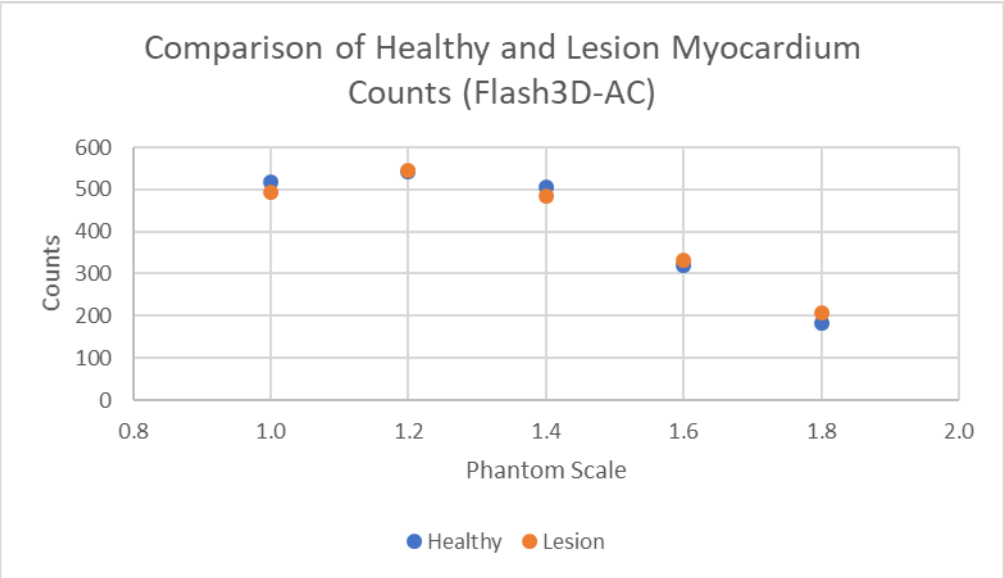

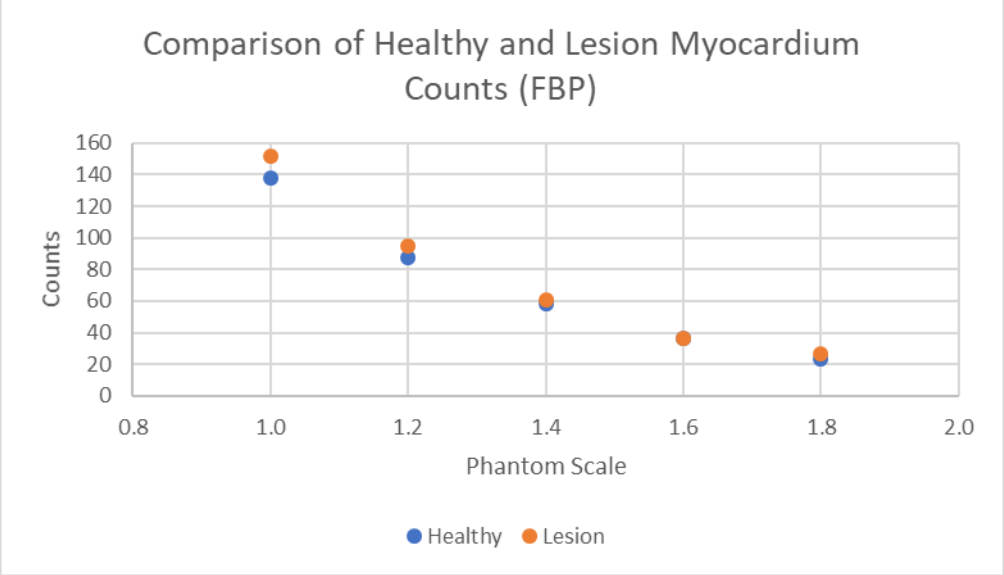

Ventricle Counts Comparison

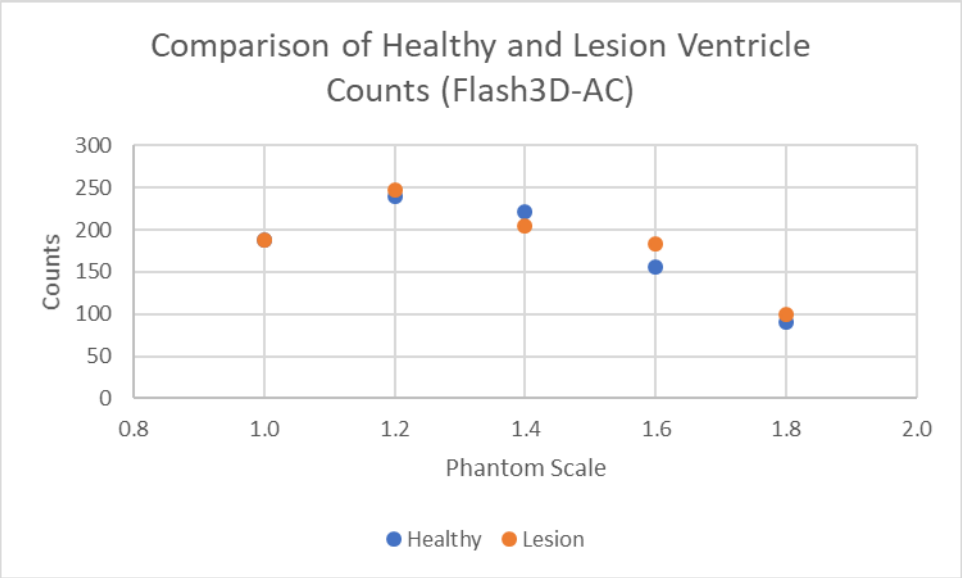

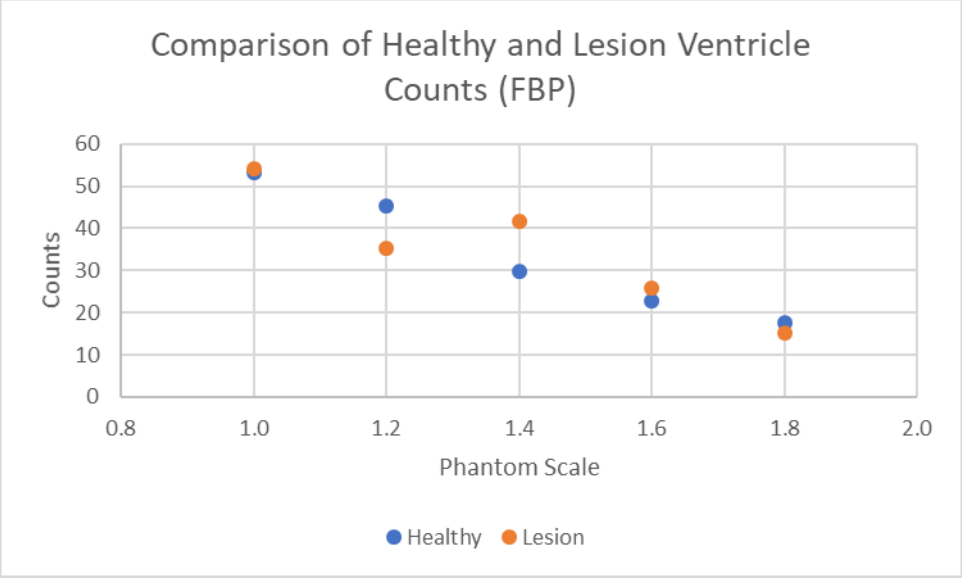

SNR Comparison

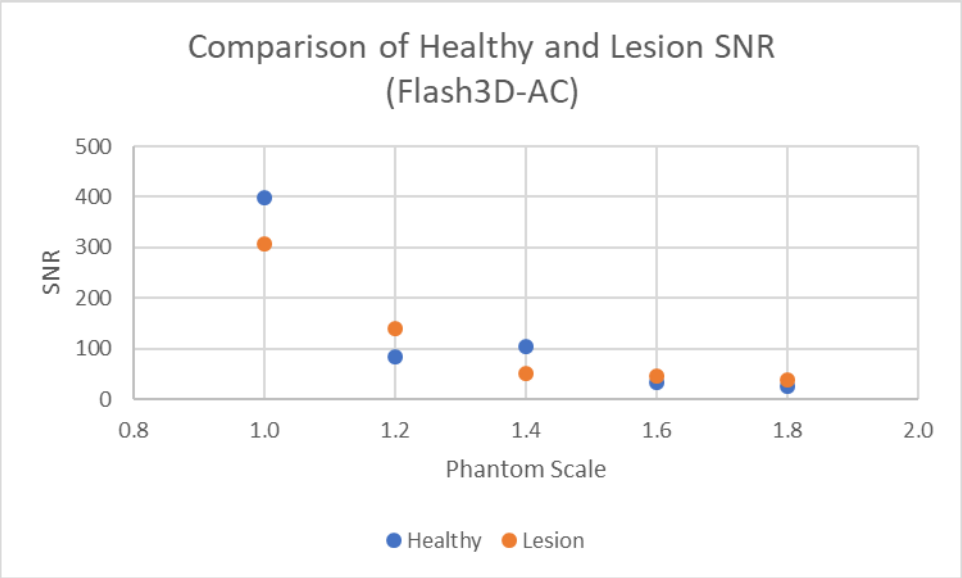

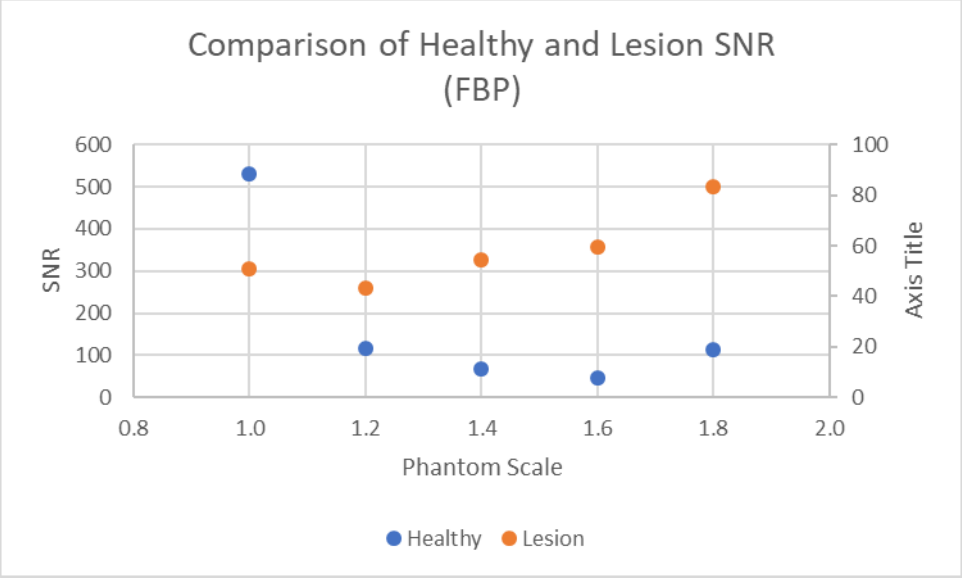

Appendix F

Observation Study Raw Data

Image #	Phantom Scale	Lesion Presence	Image View	Image Quality Rating		Observed Lesion Presence		Lesion Observation Confidence	
				Ob1	Ob2	Ob1	Ob2	Ob1	Ob2
1	1	n	SHORT AXIS	5	4	n	n	5	4
2	1	y	SHORT AXIS	3	3	y	y	3	5
3	1.6	n	SHORT AXIS	4	2	y	n	4	2
4	1	y	VERTICLE LONG AXIS	1	3	y	y	2	5
5	1.8	y	VERTICLE LONG AXIS	2	2	y	y	1	5
6	1.2	y	SHORT AXIS	5	3	y	y	5	3
7	1.6	y	SHORT AXIS	1	2	y	n	1	2
8	1.4	y	VERTICLE LONG AXIS	3	4	y	y	2	4
9	1.2	n	VERTICLE LONG AXIS	5	4	n	n	5	4
10	1.8	n	SHORT AXIS	2	3	y	n	3	2
11	1.4	n	SHORT AXIS	5	3	y	n	5	3
12	1	n	VERTICLE LONG AXIS	4	4	n	n	4	4
13	1.4	y	SHORT AXIS	1	3	y	y	1	3
14	1.4	n	VERTICLE LONG AXIS	4	3	y	n	3	2
15	1.8	y	SHORT AXIS	1	2	n	y	1	3
16	1.2	n	SHORT AXIS	5	3	y	n	4	3
17	1.2	y	VERTICLE LONG AXIS	3	3	y	y	3	4
18	1.6	n	VERTICLE LONG AXIS	3	2	y	y	3	3
19	1.8	n	VERTICLE LONG AXIS	1	2	y	n	1	1
20	1.6	y	VERTICLE LONG AXIS	2	3	y	y	3	4